Doklady Physics, Vol. 45, No. 4, 2000, pp. 129–131. Translated from Doklady Akademii Nauk, Vol. 371, No. 4, 2000, pp. 466–468.

PHYSICS

Maximum-Entropy Production Principle as a Criterion for the Morphological-Phase Selection in the Crystallization Process

L. M. Martiouchev and V. D. Seleznev

Presented by Academician V.P. Skripov May 25, 1999

Received May 28, 1999

1. Deductive construction of thermodynamics of nonequilibrium processes is based on axiomatically introducing a certain general principle used furthermore to derive all principal thermodynamic equations and laws [1]. A well-known principle of such a type is, e.g., Onsager principle for the minimum-energy dissipation. Another less known principle proposed by Ziegler [2], is that of the maximum for the dissipation-work rate, or the entropy-production rate. According to this principle, a nonequilibrium system tends to its final state by the shortest possible way. In [3], the modern critical analysis of all basic principles for irreversible processes of phenomenological thermodynamics is presented, and a rather general variational principle is put forward. In this paper, it is indicated that one of the interesting consequences of the approach proposed is the statement that an arbitrary nonequilibrium dynamic system tends to a local equilibrium state with the extreme velocity. Thus, in [2] and [3], similar statements (below, for brevity referred to as the maximum principle) on the behavior of a nonequilibrium-system are formulated independently.

Here, we would like to emphasize that these papers, apparently, due to their formalized and specific character, have not attracted proper attention. As a result, in consequent years, many researchers, studying particular nonequilibrium systems, independently came up to similar conclusions. Thus, in [4], the maximum principle is based on analysis of experimental data on the chemical-reaction kinetics. In [5], the necessity of this principle follows from analysis of a choice of the diffusion path in the triple system. In [6], the fastest-reaction principle was introduced for hydrodynamics and geophysics. In [7], the increase in the entropy production in the course of kinetic phase transition was discussed. Finally, in [8], it was emphasized (as applied to studying the biological-evolution rate) that in the case of the existence of several trajectories leading to the given value of the biological perfection, evolution chooses the most rapid trajectory among those leading to the final state.

Taking into account all the mentioned examples, we can conclude that the maximum principle is met sufficiently widely in describing processes occurring in nonequilibrium systems. At the same time, studying consequences, in which this principle is revealed in specific systems, has received little attention in literature. It seems, however, that this principle could turn out to be rather fruitful for analysis of nonequilibrium, self-organizing systems in which transitions from one of the evolution regimes to another are possible. One of the pronounced examples is the morphological transition in the course of the nonequilibrium crystallization.

2. We consider the most typical situation, of the isothermal isobaric crystallization from the supersaturated solution. The system is assumed to be two-component (a crystallizing medium and a solvent), the solvent being completely displaced by the growing crystal. It is well known that the local entropy production for systems of this type is given by the expression

$$\sigma = -\mathbf{j}\nabla\mu, \tag{1}$$

where $\mathbf{j}$ is the flow-rate density for the crystallizing component, $\nabla\mu$ is the chemical-potential gradient. Expression (1) is applicable to all parts of the volume under consideration and, in particular, to a domain in the vicinity of the surface of a crystal growing with the local linear velocity $\mathbf{V}$. In this case, the flow-rate density can be written out in the form:

$$\mathbf{j} = -(C_{\text{sol}} - C_{\text{s}})\mathbf{V}, \tag{2}$$

where C_{sol} is the crystal density and C_{s} is the concentration near the crystal surface.

Based on the maximum principle, we can conclude that the crystal growth (i.e., the evolution of the nonequilibrium crystallizing system towards its equilibrium state) proceeds with the maximum possible local entropy production. It follows from (1) and (2) that σ is

Ural State Technical University,
ul. Mira 19, Yekaterinburg, 620002 Russia
E-mail: martiouchev@mailcity.com

1028-3358/00/4504-0129$20.00

directly proportional to the velocity of increasing the growing-crystal mass. In [9], on the basis of analysis of the anisotropic Hele–Shaw experiment, and numerical calculations of the dendritic growth, a hypothesis has been put forward that in the case of more than one possible morphologies, only the most rapidly growing of them is nonlinearly stable and, therefore, observable. Thus, this example is one more independent illustration in favor of the maximum principle. For the systems under consideration, this principle can be formulated more rigorously in such a manner: in the presence of a sufficient level of fluctuations, that local state is realized among possible ones, which is characterized by the maximum value of the entropy production.

3. Employing (1), we now consider the possible consequences of the application of the maximum principle to the growth of a spherical crystal from the supersaturated solution, according to the calculation in the Mullins–Sekerka classical approximation [10]. We assume that the growing spherical particle with the radius R is subjected to deformation described by a single spherical harmonic $Y_{lm}(\theta, \varphi)$:

$$r(\theta, \varphi, t) = R + \delta(t) Y_{lm}(\theta, \varphi).$$

Here, $\delta(t) \ll R$ and t is time. The calculations are performed in the first order of the perturbance amplitude $\delta(t)$. It is possible to show, that the difference in the near-surface entropy production for the perturbed (p) and non-perturbed (n) cases (per unit solid angle) is determined by the expression of the form:

$$\sigma_p - \sigma_n \sim R\frac{d\delta}{dt} + \delta\frac{dR}{dt}. \quad (3)$$

Expression (3) is obtained for the direction (θ, φ) corresponding to the maximum value of $Y_{lm}(\theta, \varphi)$, for which the most dangerous (from the standpoint of violating the spherical-growth) state is realized. In doing so, we have assumed that $\nabla\mu \sim \nabla C_s/C_s$, while the relative supersaturation Δ is small ($\Delta \ll 1$). Transforming (3) with allowance for the results of [10], we obtain:

$$\sigma_p - \sigma_n \sim l - \left[\frac{(l+1)(l+2)+2}{2}(l-1) + 1\right]\frac{R_S^*}{R},$$

where $R_S^* = 2\Gamma/\Delta$ is the radius of a critical germ for the production of the crystalline phase, Γ is the capillary constant [10], and l is the number of a perturbing harmonic.

Within the range of possible changing in the sphere radius $[R_S^*, R_S^S]$ $R_S^S = [1 + (l+1)(l+2)/2]R_S^*$ is the radius of the sphere-stability loss with respect to infinitely small perturbance of its shape [10]), the function $(\sigma_p - \sigma_n)$ increases monotonically intersecting zero at the point $R_S^b = R_S^*(l^3 + 2l^2 + l - 2)/(2l)$.

Thus, the difference between the entropy production in the cases of the perturbed and unperturbed sphere, changes its sign at the point R_S^b, which differs from the value R_S^S predicted by the Mullins–Sekerka theory. This difference [arising due to the presence of an additional term in (3), which is proportional to the perturbance amplitude δ] is caused by the fact that the entropy production per unit solid angle [in accordance with (1) and (2)] depends not only on the linear velocity of the crystal growth but on the change in the crystal surface as well. When $R = R_S^S$ then, according to the results of the Mullins–Sekerka theory, the crystal loses its stability under an infinitely small perturbance. In the terminology of the equilibrium thermodynamics, this point can be called the spinodal of the given morphological transition. Within the range (R_S^b, R_S^S), the growing sphere is stable with respect to infinitely small perturbances [10]. However, as far as in the presence of a perturbance, the entropy production within this range is higher, the maximum principle results in the fact that the growth of the perturbed sphere is more preferable. This contradiction can be eliminated by the assumption that the growth is metastable within this range, i.e., unstable with respect to small but finite perturbances. The point R_S^b, we call binodal of a morphological transition. It should be noted that in the given case, the nature of arising instability can be explained by a possibility of the appearance of the azimuth flows nearby the sphere surface. These flows arise due to the irregularity of the substance distribution within the solid angles when the perturbance is imposed and are directed to the maximum value of $Y_{lm}(\theta, \varphi)$.

4. Figure 1 presents, as an illustration, the morphological phase diagram of the stable and unstable crystal growth. The diagram shows the crystal size as a function of the supersaturation and demonstrates the regions of existence and coexistence of morphologies. As is seen from this figure, the metastable regions related to different harmonics can intersect each other. Therefore, for a given R, there exists a possibility for simultaneous developing several different morphologies in the solution (in the case presented, there are three morphologies, namely, metastable spherical phase and two morphological ones corresponding to the second and the third harmonics). It should be emphasized that this fact well-known experimentally [11, 12] cannot be described within the classical perturbation theory [9, 10].

Thus, it is shown that the application of the maximum principle enables simple theoretical description

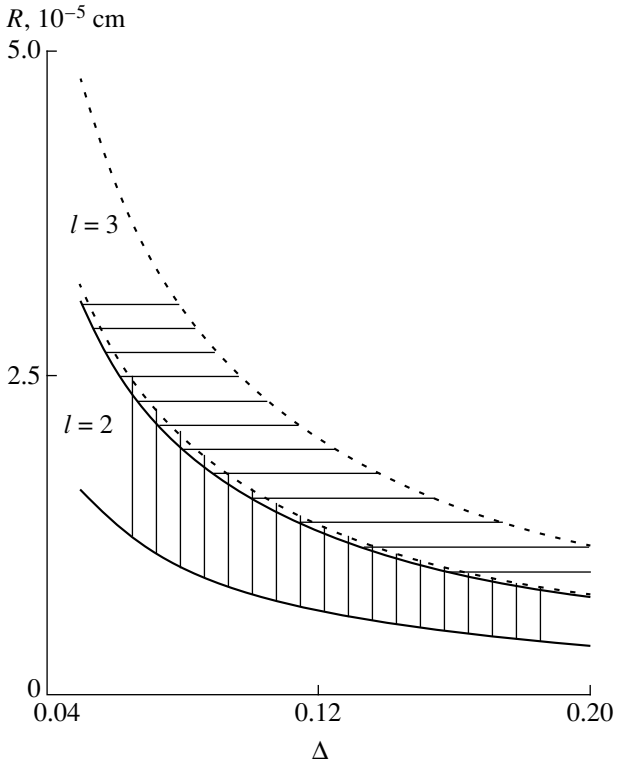

Morphological phase diagram for the stable and unstable growth. The diagram is plotted for the relative supersaturation Δ as a function of the radius R for $l = 2, 3$. Dashed and solid lines correspond to the spinodal and binodal, respectively. The metastable region is shaded. The stable and unstable growths occur below the binodal and above the spinodal, respectively. The diagram is plotted for $\Gamma = 10^{-7}$ cm.

of the coexistence of different morphological phases on the basis of the metastability concept.

REFERENCES

1. I. Gyarmati, *Nonequilibrium Thermodynamics. Field Theory and Variational Principles* (Springer-Verlag, Heidelberg, 1970; Mir, Moscow, 1974).
2. H. Ziegler, in *Progress in Solid Mechanics*, Ed. by I. N. Sneddon and R. Hill (North-Holland, Amsterdam, 1963; Mir, Moscow, 1966), Vol. 4, Chap. 2.
3. I. P. Vyrodov, Zh. Fiz. Khim., No. 6, 1329 (1982).
4. M. I. Shakhparonov, Zh. Fiz. Khim., No. 12, 3043 (1979).
5. S. V. Kornienko and A. M. Gusak, Metallofiz. Mod. Technol. **20**, 28 (1998).
6. G. S. Golitsyn, Dokl. Akad. Nauk **356**, 321 (1997) [Phys.–Dokl. **42**, 479 (1997)].
7. A. V. Melkikh and V. D. Seleznev, *Metastable States and Phase Transitions* (Ural. Otd. Ross. Akad. Nauk, Yekaterinburg, 1997).
8. S. É. Shnol', *Physicochemical Aspects of Biological Evolution* (Nauka, Moscow, 1979).
9. E. Ben-Jacob and P. Garik, Nature **343**, 523 (1990).
10. W. W. Mullins and R. F. Sekerka, J. Appl. Phys. **34**, 323 (1963).
11. Y. Sawada, Physica A **140**, 134 (1986).
12. Y. Sawada, B. Perrin, P. Tabeling, *et al.*, Phys. Rev. A **43**, 5537 (1991).

Translated by O. Chernavskaya

Doklady Physics, Vol. 45, No. 4, 2000, pp. 132–135. Translated from Doklady Akademii Nauk, Vol. 371, No. 5, 2000, pp. 607–610.

PHYSICS

An Effect of Conditions for Synthesis of Polyacenequinones on Parameters of Their Dielectric Spectra and Domain Structure

N. V. Afanas'ev, L. V. Mukhaeva, Academician M. G. Voronkov, T. G. Ermakova, A. A. Maksimov, and L. Ya. Tsarik

Received September 13, 1999

With a goal of studying formation of the molecular-domain structure for polymeric semiconductors [1], we used the model of double-layer spheroids for the evaluation of parameters of conducting polyacenequinone macromolecules on the basis of their dielectric spectra in accordance with the generalized Lorenz–Lorentz formula [2].

Polyacenequinones were obtained by the method [3] of polycyclocondensation of pyrene with dianhydride of pyromellitic acid in the presence of anhydrous zinc chloride at 580 K. When adjusting reaction conditions in order to obtain low-resistance polymers, the process duration varied within the range from 0.17 to 20 h (this duration is indicated in the polymer definitions [3]). Polycyclocondensation proceeds via intermediate complexes containing zinc chloride and results in ladder polymers. Their macromolecules contain aromatic condensed conjugate systems including cycles of benzoid and chinoid structures according to the following schematic diagram:

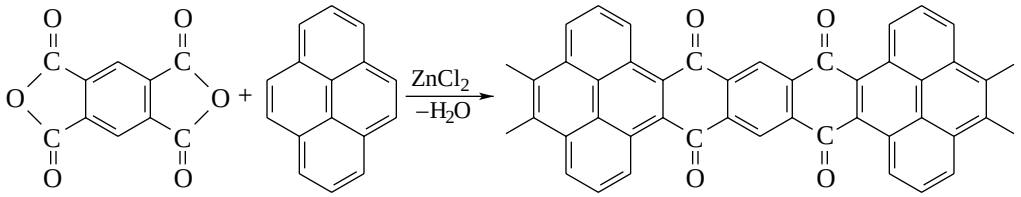

Chain fragment

With increasing the duration of the process, the polycyclocondensation is accompanied by sewing macroscopic chains (macrochains) [4] with forming insoluble nonmelting three-dimensional polymers exhibiting the domain structure [1].

Previously, this fact was not taken into account, and dielectric spectra of polyacenequinones were interpreted on the basis of the concept of electronic relaxation polarization of conducting molecular chains [5].

The values of parameters in the dispersion region caused by the interlayer polarization of such polymers (see table) were determined by the method of dispersion diagrams [6] (Fig. 1). These parameters are: the low-frequency ε'_S and the high-frequency ε'_∞ limits of the dielectric permittivity ε'; the relaxation time $\tau = (2\pi\nu_M)^{-1}$, where ν_M is the value of the frequency ν of the electric field applied, for which the coefficient of dielectric loss ε'' has the maximum ε''_M and the parameter of the relaxation time distribution is $0 \le \alpha \le 1$. The plots are the normalized Debye functions: i.e., the reduced dielectric permittivity $\varepsilon_1 = \dfrac{(\varepsilon' - \varepsilon'_\infty)}{\Delta\varepsilon'}$, where $\Delta\varepsilon' = \varepsilon'_S - \varepsilon'_\infty$ and the reduced loss factor $\varepsilon_2 = \dfrac{\varepsilon''}{\varepsilon''_M}$.

Previously, it was assumed that the increment $\Delta\varepsilon'$ of the dielectric permittivity in the dispersion region does not change with increasing the reaction duration *t* of the polyacenequinone formation from 3 to 8 h [7]. However, the use of the pseudoisolation effect for conducting macromolecules [8] in order to determine their

Irkutsk State Technical University, ul. K. Marksa 1, Irkutsk, 664003 Russia
Institute of Chemistry, Siberian Division, Russian Academy of Sciences, ul. Favorskogo 1, Irkutsk, 664033 Russia

1028-3358/00/4504-0132$20.00

shape made it possible to measure parameters of the dispersion region under conditions of the maximum electrical conduction $\sigma_0 \approx 10^{-2}$ S/m attained for $t = 20$ h (Fig. 1). In this case, a significant increase of $\Delta\varepsilon'$ was found (Fig. 2), which provides evidence for a large volume concentration of the conducting phase $v \longrightarrow 1$ in accordance with the generalized Lorenz–Lorentz formula.

The structure model of close-packed two-layer spheroids was employed to estimate the domain parameters of these polymers. Below, we mark the values related to the low-resistance part of the spheroid and relatively high-resistance near-surface layer by the subscripts 1 and 2, respectively. For simplicity, all the spheroids are considered to be equal and oriented by their variable semiaxis a in parallel to the electric field applied. We call the ratio $f = \dfrac{b}{a}$ (b and $c = b$ are the other semiaxes) the domain-shape coefficient determining its depolarization coefficient $0 \le N \le 1$ [2].

In order to describe the frequency dependence of the complex dielectric permittivity ε, we used the generalized Lorenz–Lorentz formula

$$\varepsilon = \varepsilon_2\left[1 + \frac{v(\varepsilon_1 - \varepsilon_2)}{\varepsilon_2 + (1 - v)N(\varepsilon_1 - \varepsilon_2)}\right]. \qquad (1)$$

The volume concentration of the conducting phase was determined as

$$v = \frac{V_1}{V_1 + V_2}, \qquad (2)$$

where V is the volume. Thus, for close-packed spheroids $v \longrightarrow 1$ as $V_2 \longrightarrow 0$. In an alternating electric field with the circular frequency ω, the quantities ε_i (i = 1, 2) in formula (1) are complex:

$$\varepsilon_i = \varepsilon_i' - j\varepsilon_i'' = \varepsilon_\infty' - j\frac{\sigma_i}{\varepsilon_0\omega}. \qquad (3)$$

Here, we consider for simplicity ε_i' to be the same and equal to $\varepsilon_\infty' = 4$, i.e., to the value of the dielectric permittivity of polyacenequinones at sufficiently high frequencies and low temperatures, σ is the conductivity and ε_0 is the electric constant in IS.

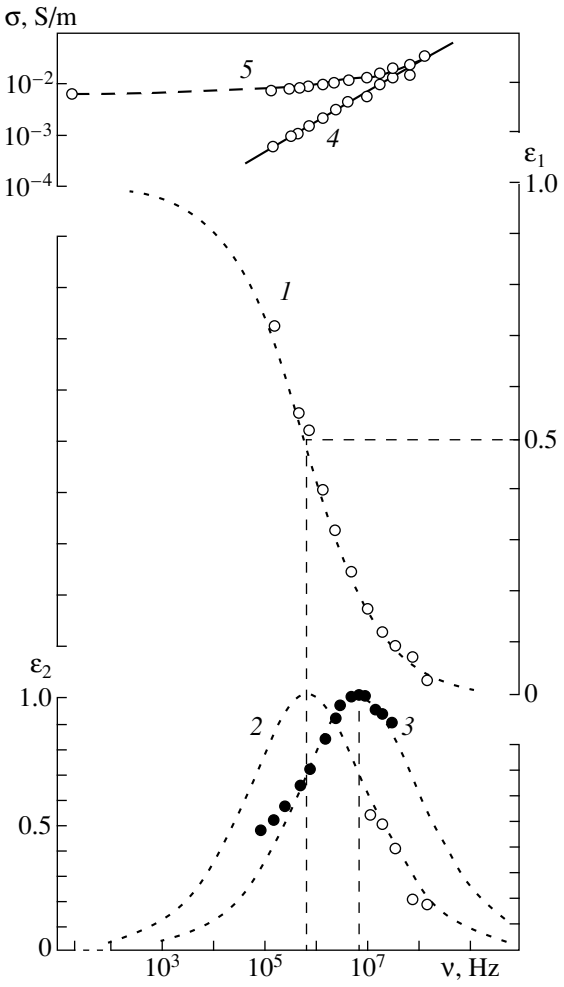

Fig. 1. Dispersion plots for 76EHE (20) polyacenequinone: (*1*, *2*) compressed sample; (*3*) mixture with a paraffin; (*4*) active conduction σ; (*5*) $\sigma + \sigma_0$. Temperature is 293 K. The thickness of the compressed sample is 0.28 mm, its diameter is 2.5 mm; the rigid electrodes are made of steel.

Parameters of dielectric spectra and molecular domains of polyacenequinones

Polymer	σ_0, 10^{-5} S/m	σ_p, 10^{-5} S/m	ν_M, 10^4 Hz	ε_M''	α	ν_M', 10^4 Hz	α'	N	f
Synthesis [13]									
76EHE(24*)	2	2.3	1.6	5.3	0.47	6	0.47	0.31	0.87
76EHE(5)	5	10	5.7	7.4	0.55	22.4	0.5	0.24	0.69
76EHE(10)	27	–	3.2	11.8	0.55	–	–	–	–
Synthesis [7]									
76EHE(3)	70	200	158	3.3	0.6	400	0.6	0.34	1.04
76EHE(8)	500	720	300	7.6	0.6	1580	0.6	0.39	1.23
76EHE(20)	710	340	70	16.6	0.5	710	0.5	0.33	1.00

Note: Polymer 76EHE(24*) was obtained with the interruption in the synthesis process.

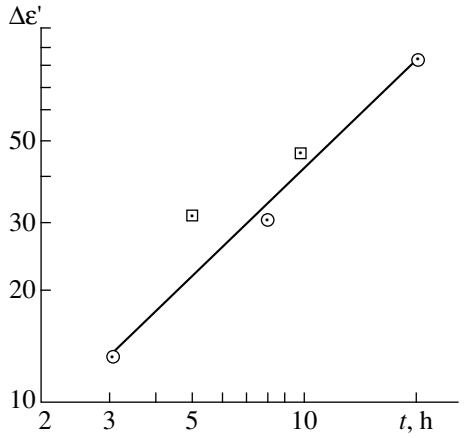

Fig. 2. The dielectric-permittivity increment for polyacenequinone as a function of the synthesis duration *t*: ⊙—data of [7], ⊡—data of [1].

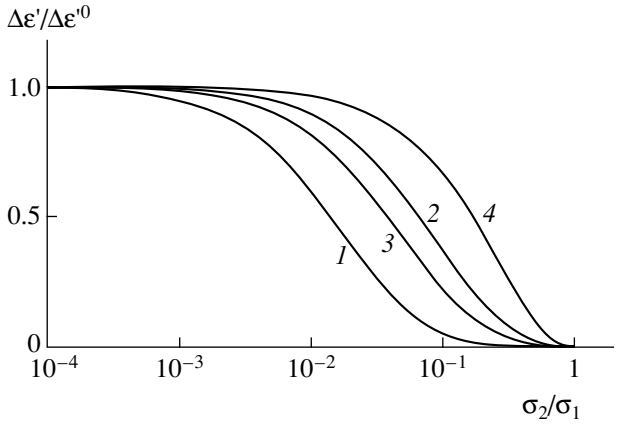

Fig. 3. Reduced dielectric permittivity increment as a function of the reduced conduction of the domain insulating layer for: (*1*, *2*) a spherical domain; (*3*, *4*) a planar domain ($N = 1$). The volume concentration of the domain conducting phase is (*1*, *3*) 0.9 and (*2*, *4*) 0.5.

Substituting ε_i from (3) into formula (1), we obtain expressions for parameters of the Debye equation [9]:

$$\tau = \frac{\tau^0}{1 + \left[\frac{1}{(1-\nu)N} - 1\right]\frac{\sigma_2}{\sigma_1}}, \quad (4)$$

$$\Delta\varepsilon' = \frac{\Delta\varepsilon'^0}{\left[1 + \frac{1}{(1-\nu)N(\sigma_1/\sigma_2 - 1)}\right]^2}. \quad (5)$$

Here,

$$\tau^0 = \frac{\varepsilon_0\varepsilon'_\infty}{(1-\nu)N\sigma_1}, \quad (6)$$

$$\Delta\varepsilon'^0 = \frac{\nu\varepsilon'_\infty}{(1-\nu)N}. \quad (7)$$

It was assumed previously that $\beta = \frac{\sigma_2}{\sigma_1}$, and in this case, τ and $\Delta\varepsilon'$ are equal to τ^0 and $\Delta\varepsilon'^0$, respectively. However, for low-resistivity polymeric semiconductors, this assumption requires substantiation, since the cause for the formation in the process of synthesis of domain near-surface layers has still not been established. In the case of their small thickness (and, consequently, a large value of $\Delta\varepsilon'$), the increase of σ_2 is possible due to charge-carrier tunneling. It follows from Fig. 3 and formula (4) that a noticeable reduction in τ and $\Delta\varepsilon'$ is expected already for $\beta = 0.01$.

The values of parameters for the structure model proposed are presented in the table; these parameters are determined with allowance for the depolarization coefficient of domains, calculated according to the formula taken from [8]:

$$\frac{1}{N} = \frac{1-\nu'}{\varepsilon'_p}\left(\frac{\Delta\varepsilon'}{\nu'_M/\nu_M - 1} + \varepsilon'_p - \varepsilon'_\infty\right). \quad (8)$$

Here, ν'_M is the frequency in the maximum of the loss factor for a mixture of polyacenequinones with a paraffin for reasonably small volume concentration $\nu'(0, 1)$ of the polymer, $\varepsilon'_p \approx 2$ is the dielectric permittivity of paraffin. The values of *N* obtained are close to 1/3 (see table), which is consistent with a spherical shape of domains. Based on this fact, we have proposed a method for determination of dielectric-spectrum parameters. This method is characterized by a high sensitivity in choosing optimum variants of dispersion plots (Fig. 4) and can be employed for low-resistance polymers, when the use of the logarithmic-asymptote method [1] is hampered. With allowance for the value of *N* obtained, the frequency ν'_M in the spectrum of the mixture of polyacenequinones with paraffin makes it possible to determine the value of σ_p, i.e., the most probable value of domain conduction in the static distribution [8]. The other parameter of this distribution is α, which takes values virtually similar to the analogous parameter α' for the mixture [10] (see table).

A possibility of employing formula (8) for determination of the domain depolarization coefficient is explained by the fact that the domains, but not the grains, are structure elements responsible for the interlayer polarization in the dispersion region under study in the mixture of polyacenequinones with paraffin. This statement is also true in that case when a grain contains many domains significantly different in their conduction. The grains are responsible for the surface capacity [11]. In the spectra of compressed polyacenequinone samples, the corresponding dispersion region

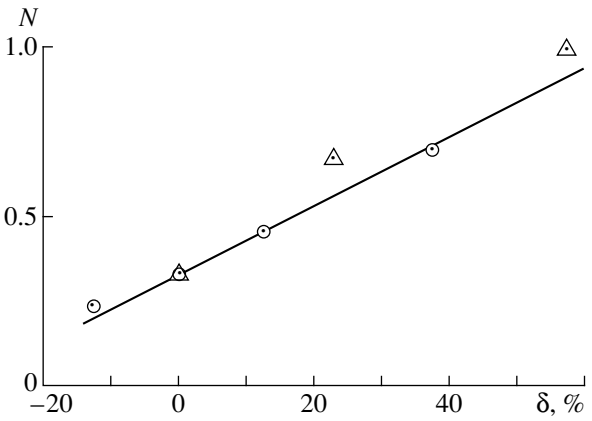

Fig. 4. Dependence of the depolarization coefficient of a domain on the relative variation in the dielectric-permittivity increment δ for a constant value of the relaxation-time distribution parameter: (△) 76EHE(3), (⊙) 76EHE(20).

lies within the range of lower frequencies. This region reduces in the case of isolating grains by paraffin and becomes virtually unobservable for $\nu' = 0.1$.

With account of the domain distribution as a function of the conduction, we should replace σ_1 by σ_n in formulas (4)–(6) (see table). In this case, the most probable value of the relaxation time in the statistical distribution must be taken for this quantity.

According to formula (7), in the case of $\Delta\varepsilon' = 80$ (Fig. 2), the volume concentration of the conducting phase in the spherical domain attains 0.87. This corresponds to the ratio $h/R = 0.047$, where h is the thickness of the near-surface insulated layer in the domain and R is its radius. Estimating R by a value not more than 1 μm [12], we obtain $h \le 50$ nm.

For explanation of the expected values of $\Delta\varepsilon' > 100$ (Fig. 2), we can assume the existence of deformation of spherical domains in the vicinity of their contact with neighbor ones. The limiting structure model is a close package of two-layer cubes, which is equivalent to a compressed two-layer spheroid ($f = \infty$) oriented perpendicular to the electric field ($N = 1$). In this case, formulas (1) and (2) are consistent with the Maxwell–Wagner two-layer model [9], provided that we ignore the insignificant contribution of thin insulated layers located in parallel with the electric field.

The study carried out testifies to the fact that the model of two-layer spheroids and the method of the pseudoisolation effect suggested can be used for studying the domain structure of low-resistance polymeric semiconductors with large values of the dielectric-permittivity increment.

ACKNOWLEDGMENTS

This work was supported by the Federal Program "Integratsiya," grant no. 2.1-187

REFERENCES

1. N. V. Afanas'ev, L. V. Mukhaeva, M. G. Voronkov, and T. G. Ermakova, Dokl. Akad. Nauk **323**, 452 (1992) [Sov. Phys. Dokl. **37**, 135 (1992)].
2. A. V. Netushil, B. Ya. Zhukhovitskiĭ, V. N. Kudin, and E. P. Parinin, *High-Frequency Heating of Dielectrics and Semiconductors* (Gosénergoizdat, Moscow, Leningrad, 1959).
3. R. Rosen and H. A. Pohl, J. Polymer. Sci., Ser. A1 **4**, 1135 (1966).
4. V. V. Korshak and S. V. Vinogradova, *Equilibrium Polycondensation* (Nauka, Moscow, 1968).
5. H. A. Pohl and M. Pollak, Chem. Phys. **66**, 4031 (1977).
6. N. V. Afanas'ev, L. V. Mukhaeva, M. G. Voronkov, *et al*., Dokl. Akad. Nauk SSSR **319**, 858 (1991) [Sov. Phys.–Dokl. **36**, 580 (1991)].
7. N. V. Afanas'ev, L. V. Mukhaeva, M. G. Voronkov, and T. G. Ermakova, Dokl. Akad. Nauk **326**, 999 (1992) [Sov. Phys.–Dokl. **37**, 508 (1992)].
8. N. V. Afanas'ev, L. V. Mukhaeva, M. G. Voronkov, and T. G. Ermakova, Dokl. Akad. Nauk **360**, 614 (1998) [Dokl. Phys. **43**, 33 (1998)].
9. A. R. Hippel, *Dielectrics and Waves* (Wiley, New York; Chapman and Hall, London, 1954; Inostrannaya Literatura, Moscow, 1960).
10. N. V. Afanas'ev, L. V. Mukhaeva, M. G. Voronkov, *et al*., Dokl. Akad. Nauk SSSR **306**, 328 (1989) [Sov. Phys.–Dokl. **34**, 439 (1989)].
11. N. V. Afanas'ev, L. V. Mukhaeva, M. G. Voronkov, and T. G. Ermakova, Dokl. Akad. Nauk **337**, 595 (1994) [Phys.–Dokl. **39**, 556 (1994)].
12. N. V. Afanas'ev, L. V. Mukhaeva, M. G. Voronkov, and T. G. Ermakova, Dokl. Akad. Nauk **330**, 177 (1993) [Phys.–Dokl. **38**, 205 (1993)].
13. N. V. Afanas'ev, R. V. Afanas'eva, T. G. Ermakova, and V. A. Lopyrev, Vysokomol. Soedin., Ser. A **21**, 413 (1979).

Translated by T. Galkina

Doklady Physics, Vol. 45, No. 4, 2000, pp. 136–141. Translated from Doklady Akademii Nauk, Vol. 371, No. 6, 2000, pp. 753–758.

PHYSICS

Three-Dimensional Spinning Waves in the Case of Gas-Free Combustion

T. P. Ivleva and Academician A. G. Merzhanov

Received November 26, 1999

Spinning waves represent a spiral-helix motion of a localized combustion center, which occurs along the lateral surface of a cylindrical sample [1, 2]. After their discovery, these waves stimulated a lot of investigations. Solving unsteady two-dimensional equations of heat conduction and kinetics in the case of combustion of a thin adiabatic shell, authors of [3] have performed for the first time computer modeling of a spinning wave. Then, the two-dimensional approach started to be used in other theoretical studies as well (see, e.g., [4, 5]). However, processes that occurred inside a solid sample in the presence on its lateral surface of a spinning wave remained yet unknown. Attempts to consider three-dimensional models [6, 7] have not yield desired results, because computational algorithms chosen led to rather difficult calculations.

In [8], we have succeeded in a three-dimensional numerical investigation of a spinning wave for a cylinder, having a small radius, and have compared the results obtained with those of the two-dimensional calculation. It was shown that, as in the two-dimensional case, the three-dimensional wave has only one spinning center moving with a constant velocity along a spiral helix. Both models yield close values for the temperature of the center and its dimensions on the surface. The wave period and the center velocity of motion exhibit somewhat stronger differences. In addition, in [8], a new characteristic of a combustion center, namely, its radial dimension was defined. This quantity has a noticeable value, but the radius is smaller than that of the cylinder. While the combustion center moves along a spiral path, its dimensions do not vary. Therefore, its thermal effect on the cylinder axial region is constant in its magnitude (but not in the direction). As a result, combustion of the cylinder central domain occurs in a steady mode that is impossible for the one-dimensional regime of the flame propagation when parameters related to the unstable region have the same values. Furthermore, such a steady-state spinning wave is called classical.

Here, we present results for the numerical analysis of three-dimensional equations that describe gas-free combustion of samples having large radii. New types of spinning waves, which were not described in literature and have undoubtedly three-dimensional nature, have been discovered.

Similarly to [8], we solved the simplest unsteady dimensionless system of equations describing gas-free combustion (according to Frank-Kamenetskiĭ [9]) with the corresponding boundary conditions. For brevity, we do not write out this system of equations here. However, we emphasize that the constitutive parameters of the problem are the following: the dimensionless temperature $\theta = \frac{T - T_*}{\mathrm{Ar} T_*}$, the dimensionless time $\tau = \frac{t}{t_*}$, the dimensionless cylinder radius $R_0 = \frac{r_0}{h_*}$, the Todes criterion $\mathrm{Td} = \mathrm{Ar}\frac{T_*}{T_* - T_0}$, and the Arrhenius criterion $\mathrm{Ar} = \frac{RT_*}{E}$. Here, T is temperature; T_* is the characteristic temperature usually taken to be coincident with the combustion adiabatic temperature; t is time; t_* is the characteristic reaction time; r_0 is the dimensional cylinder radius; h_* is the characteristic width of the reaction zone; R is the gas constant; E is the activation energy; and T_0 is the initial temperature of both the sample and the environment.

We emphasize that, for the chosen temperature scale, the equality $\theta = \theta_{ad} = 0$ corresponds to the adiabatic temperature; the initial temperature is negative ($\theta_0 = -\mathrm{Td}^{-1}$); and the combustion-center temperature is superadiabatic ($\theta > 0$). Details concerning the equations and relations connecting dimensional and dimensionless quantities are presented in [8].

In this paper, similarly to [8], we pay attention mainly to the role of two parameters. They are:

—The depth of the remoteness from the stability limit [10] $\alpha_{st} = 9.1\mathrm{Td} - 2.5\mathrm{Ar}$[1] and

Institute of Structural Macrokinetics, Russian Academy of Sciences, Chernogolovka, Moscow oblast, 142432 Russia

[1] The quantity α_{st} is inversely proportional to the enthalpy excess in the combustion wave. For the stability limit (critical stability), $\alpha_{st} = \alpha_{st}^{crit} = 1$. In the unstable region, $\alpha_{st} < 1$.

1028-3358/00/4504-0136$20.00

—The dimensionless radius of the cylinder[2] $R_0 = \frac{r_0}{\mathrm{Td}\Delta z_m}$ [8], where $\Delta z_m = a u_{\mathrm{ZFK}}^{-1}$.

Carrying out the calculations, we paid most attention to the quantity R_0, as the most important one in analysis of not one-dimensional regimes. The role of the heat loss is not considered here. Similarly to [8], the main results following from the analysis of unsteady temperature fields and the conversion depth were calculated with the help of a Pentium-266 personal computer.

Below, we describe characteristic features of newly discovered types of spinning waves.

1. Unsteady one-center spinning waves. The behavior of the spinning center resembles that described in [8] but has an unsteady nature. The dimensions of the center, the velocity of its motion along a spiral helix, and temperature fluctuate. When expanding, the center embraces by its peripheral region a part of the cylinder axis and then narrows again. In contrast to the steady case [8], this causes oscillations of both temperature and an instantaneous combustion rate at the cylinder axis. When the combustion center becomes localized in near-surface layers of the cylinder, the heat flux transferred from it to the cylinder axis is insufficient to cause the transformation of the substance on the axis, because the cylinder has a large radius. However, this flux forms an extensive zone of the warmed-up substance in the cross section orthogonal to the axis. The combustion center approaching this zone initiates its frontal burning. Depending on the constitutive parameters, the temperature maximum can occur at any point of the frontal line, including the cylinder axis as well. After the interior of the sample has burnt, the combustion center again becomes localized near the cylinder surface at which the substance is yet unreacted. That is why, the structure and velocity of the combustion center exhibit temporal periodic variations with periodicity not related to 2π.

2. Two-center spinning waves. There are two spinning centers situated symmetrically. Their motion can be accompanied by either steady-front propagation along the cylinder axis (at small diameters of the samples and insignificant remoteness from the stability threshold) or burning-cylinder central domains in the pulsating regime. In the second case, the behavior of the combustion centers is unsteady. Initially, they expand in the radial direction. As a result, their peripheral regions collide on the cylinder axis, and form a two-headed structure, the temperature increasing in the center of the cylinder. Then, the binary combustion center decomposes into two narrowing parts, and temperature on the cylinder axis drops. The complete separation of a combustion center from the surface does not occur. The periodicity of the unsteady two-headed regime is not connected strictly with 2π. Temperature oscillations in the combustion centers in the cylinder surface areas occur simultaneously (Fig. 1).

We call these regimes conjugate spinning waves.

3. Three-center spinning waves. In contrast to the above-discussed regime, a three-center spinning wave has three combustion centers, which, in turn, leave the surface and move toward the interior of the cylinder. The center, being inside the cylinder, merges with one of the two near-surface centers. As a result, two new combustion centers arise. One of them reaches the surface, while the other moves to the third center. Observing the cylinder surface, we would see disappearance and, then, appearance of the combustion centers. To be more exact, three combustion centers visible on the surface, in turn, flash and, then, lose their brightness. Such regimes can be called flickering spinning waves.

4. Many-center waves. In this regime, four spinning centers that can, in pairs, leave the surface and displace toward the interior of the sample are formed. Moving, they can interact with both each other and the centers staying in the near-surface layer. Possible division of the centers into two parts leads to formation of two-headed structures. The maximum number of the heads observed simultaneously is six. Among the steady-state regimes discovered, this regime is the most complicated, because the spatial inhomogeneity and unsteady temporal behavior are the most clearly expressed in it (Fig. 2).

The features noted above represent only a small part of the information obtained. Discussing it, we present below the data that are, in our opinion, the most important.

First of all, we emphasize that, as the cylinder radius increases, the space-time pattern of spinning-wave propagation becomes more complicated. From the classical steady-state spinning wave, which has one combustion center localized near the cylinder surface [8], we pass to many-center regimes. In these regimes, the velocity of the centers is unsteady, the centers separate from the surface (the phenomenon of flickering) and interact in the sample volume with the subsequent formation of many-headed structures.

We keep the term *spinning* for such regimes, because the velocity of a combustion center preserves the spiral (translational–rotational) component in the cases described. However, the role of this component decreases with increasing R_0, i.e., the spinning pattern of wave propagation becomes more complicated (degenerates). Simultaneously, the role of the radial component of the center velocity becomes more essential, which leads to forming complicated configurations of the unsteady temperature field.

This result is extremely important. It implies that, in the general case, it is impossible to ignore the radial heat transfer in the case of the gas-free combustion of

[2] The quantity u_{ZFK} represents a steady-state wave-propagation velocity given by the Zel'dovich–Frank-Kamenetskiĭ theory; α is the thermometric conductivity; Δz_m is the width of the Mikhel'son pre-ignition zone.

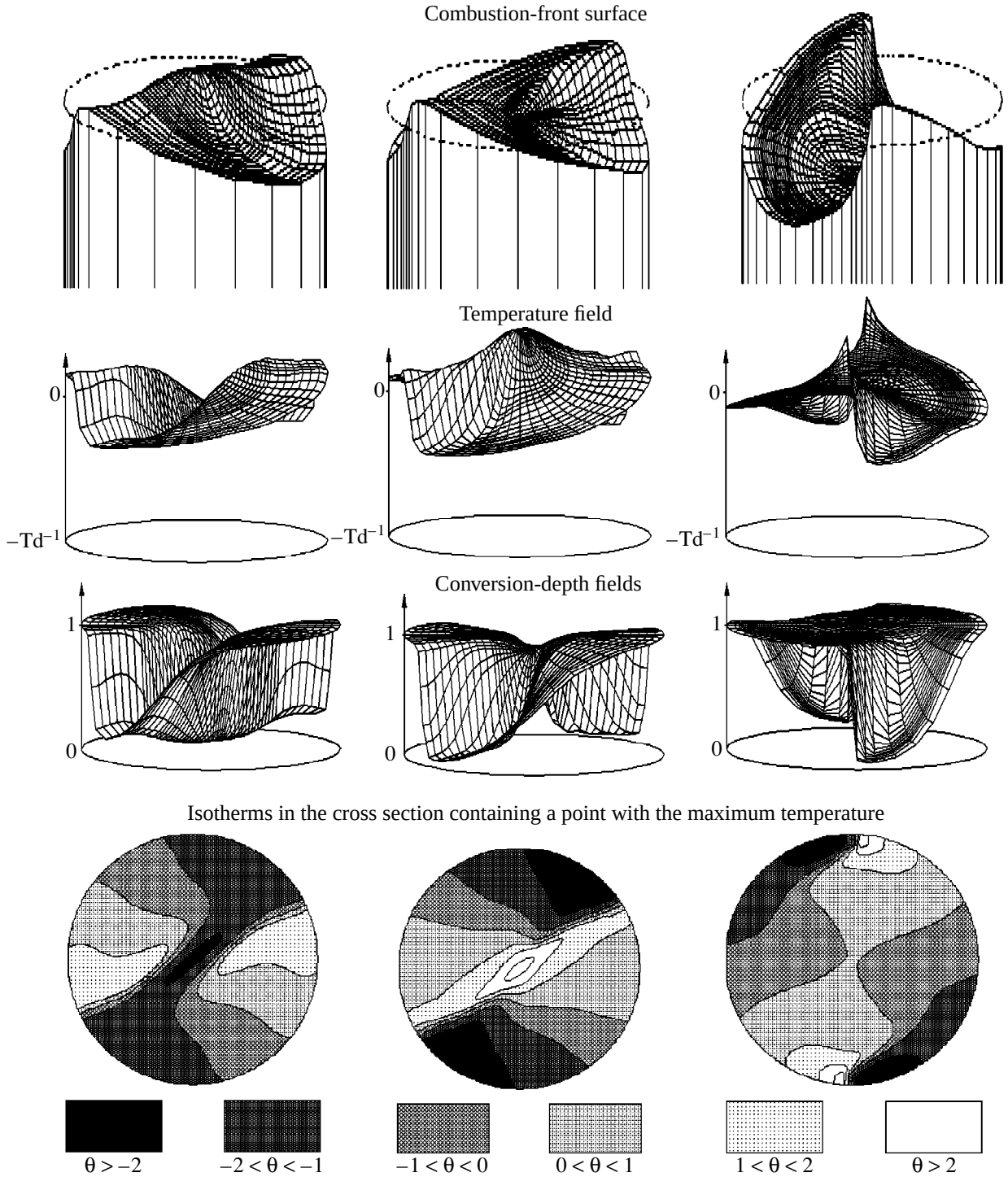

Fig. 1. Conjugate spinning wave at time moments corresponding to the expansion of combustion centers in the radial direction, merging the centers on the axis, and localization of the centers on the surface. Front structure (the dashed line corresponds to the cross section orthogonal to the axis and passing through a point with the maximum temperature), temperature fields and conversion depths, as well as isotherms for the same cross section are shown for each of these moments at $\alpha_{st} = 0.9$ and $R_0 = 67$.

solid samples. Thus, the two-dimensional analysis carried out in [3] and in other studies can be valid only for either samples of small diameters or an artificial model of the adiabatic cylindrical shell.

In all the cases under consideration, even in the case of many-center waves, we deal with the periodic wave propagation. Although, for each set of the values of α_{st} and R_0, the structure and velocity of the wave undergo

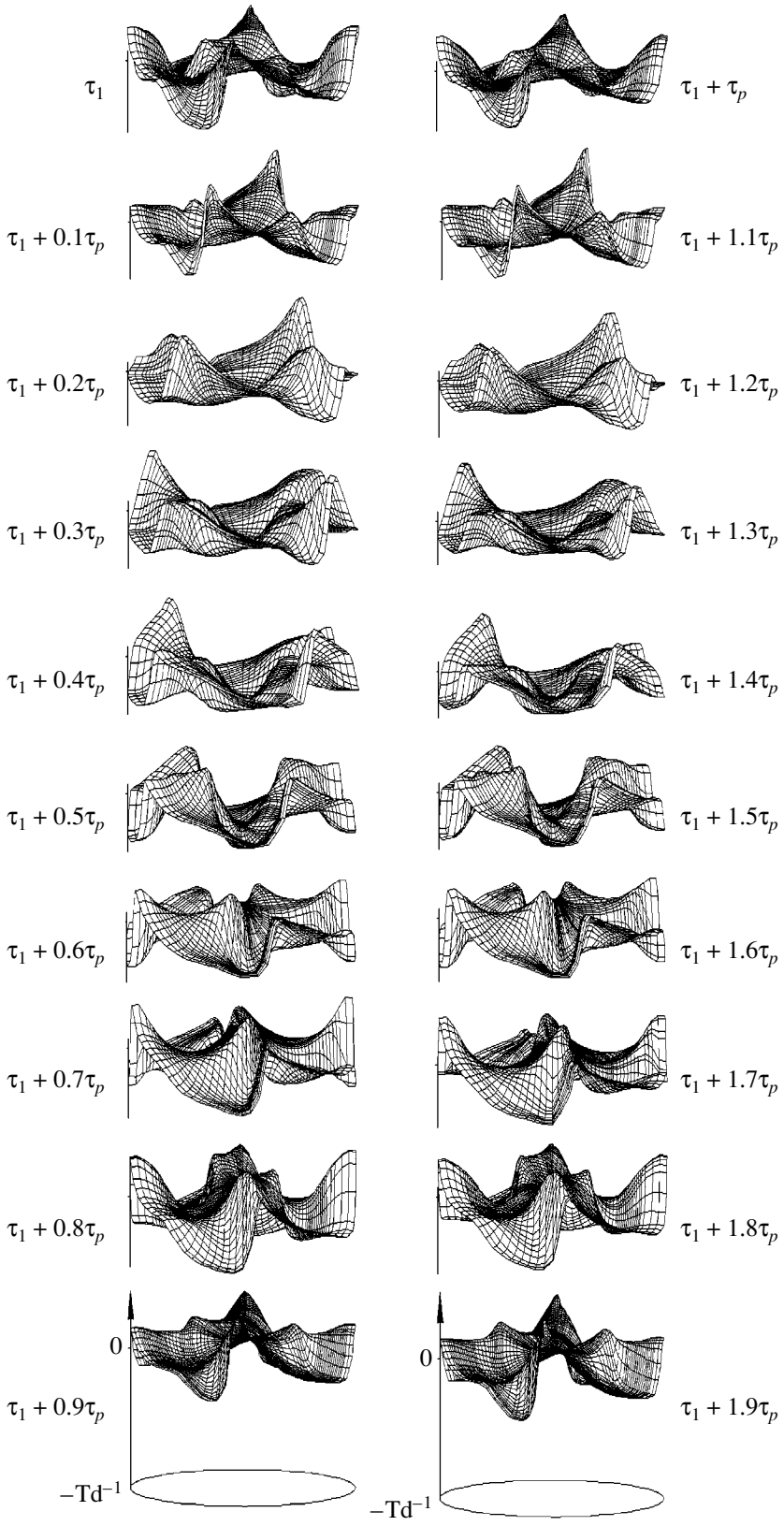

Fig. 2. Dynamics of the temporal variations in the structure of the temperature field for a many-center wave. The patterns corresponds to the cross section orthogonal to the axis and containing a point with the maximum temperature (the point moves downward as the sample combustion occurs). The data are presented with temporal discreteness equal to 0.1 of the wave period τ_p for $\alpha_{st} = 0.9$ and $R_0 = 86$.

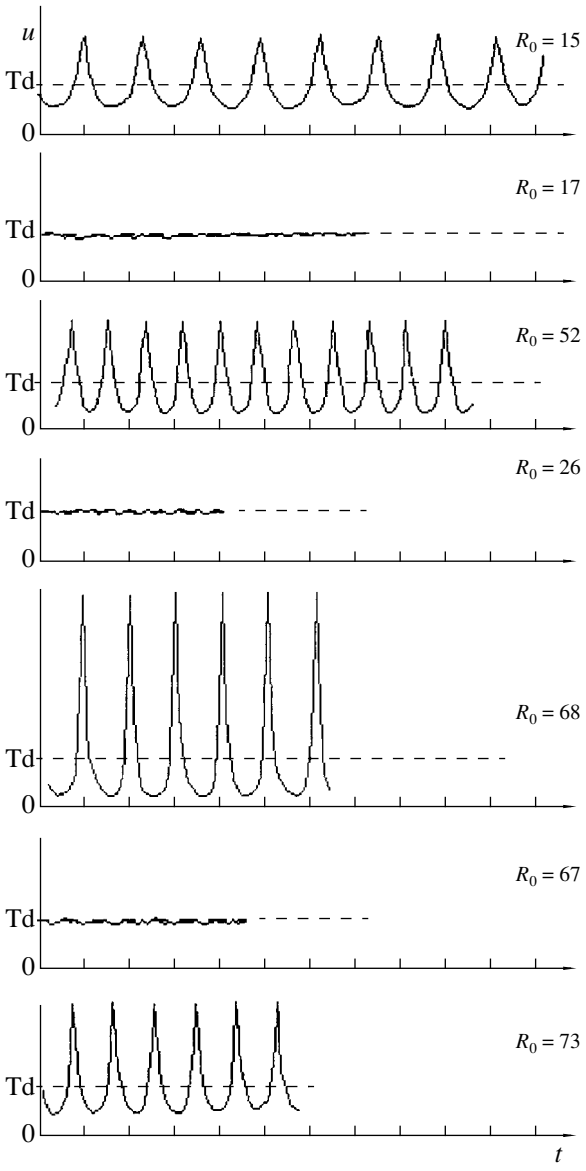

Fig. 3. Temporal dependence of instantaneous translational velocity for the wave propagation along the cylinder axis. The data correspond to different radii R_0 of the cylinder and various regimes occurring at $\alpha_{st} = 0.9$. The following structures are shown from above to below: the plane front ($R_0 \approx 15$); the classical spinning wave ($R_0 \approx 17$); the unsteady one-center wave ($R_0 \approx 52$); the steady conjugate spinning wave ($R_0 \approx 26$); the unsteady conjugate spinning wave ($R_0 \approx 68$), the flickering wave ($R_0 \approx 67$); and the many-center wave ($R_0 \approx 73$). The graduation mark on the time axis is equal to $\Delta\tau = 250$.

diverse variations during the period, the pattern observed being repeated in the next period. Even for the most complicated many-center wave, there exist the propagation periodicity (Fig. 2). Reflecting a tendency to chaotization, the period increases and the front structure becomes more complicated with increasing R_0. The onset of chaos is expected at small values of α_{st} and large R_0. In our opinion, the chaotic regime has the following features: the presence of many combustion centers, variation of their number due to their appearance and disappearance, and an often change in directions of their motion. However, the main feature of the chaotic regime of combustion is the absence of the periodicity in the unsteady structure of the front propagation.

Figure 3 shows instantaneous velocities characterizing wave propagation along the cylinder axis, as a function of time at different α_{st} and R_0. The region of both plane one-dimensional self-sustained oscillations of the front ($\alpha_{st} < \alpha_{st}^{crit} = 1$, $R_0 < R_0^{crit}$) and the spinning waves ($\alpha_{st} < \alpha_{st}^{crit} = 1$, $R_0 > R_0^{crit}$). Since $\alpha_{st} < \alpha_{st}^{crit}$, all the data presented relate to the unstable region. A curious fact was discovered when the effect of the cylinder radial dimension on the combustion regime was investigated. At small R_0, the velocity oscillates periodically near a certain average value $\bar{u}_z \approx$ Td (in accordance with [10]). After the threshold $R_0^{crit} \approx 16$ has been passed, the regime acquires the one-center nature and corresponds to the steady character of the front propagation along the cylinder axis. With further increasing R_0 (and preserving the one-center regime), the oscillations, whose amplitude grows with increasing sample diameters, appear on the cylinder axis again. There is a simple explanation for this, seemingly, unusual effect. When plane self-sustained oscillations occur, the instability is distributed uniformly over the sample cross section, i.e., all of its points are under the same conditions. For a classical-spinning wave, the instability region is localized in cylinder surface layers, and the substance conversion in the interior of the sample is governed by the heat flux transferred from the combustion center moving in the near-surface layers. As the cylinder radius grows, the one-center regime becomes unsteady. At the same time, velocity oscillations arise on the cylinder axis. The larger the cylinder radius, the more considerable the oscillations (Fig. 3). A similar situation arises in the case of conjugate regimes: At small R_0, both the centers on the cylinder surface and the combustion front on its axis move with the constant velocity (Fig. 3). However, with increasing R_0, the unsteady character of the front propagation along both the surface and the axis of the cylinder enhances (Fig. 3).

As is shown in this paper, an increase in R_0 leads also to forming the flickering and other many-center regimes. In these regimes, the character of the front propagation along the sample axis is controlled by the variation of the heat flux from the moving centers.

An important result of our calculations is the nonuniqueness of the steady-state spinning regimes discovered here and occurring at large values of R_0 (Fig. 4). Thus, the existence of two regimes (one-center and two-center waves) is possible at $R_0' < R_0 < R_0''$. More-

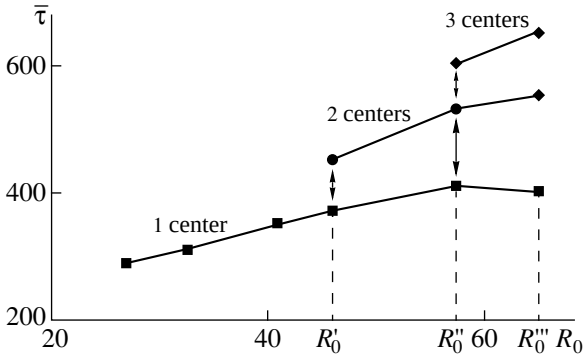

Fig. 4. Non-uniqueness of the steady-state spinning regimes for $\alpha_{st} = 0.86$. Here, $\bar{\tau}$ is the average time of the complete center revolution about the cylinder axis.

over, if $R_0'' < R_0 < R_0'''$, three regimes (one-center, two-center, and three-center waves) can occur. Realization of one or other regime depends on ignition conditions. The non-uniqueness of the spinning waves should be a subject of a more detailed study and needs in substantiation.

The three-dimensional spinning waves occurring in gas-free systems are ill-studied experimentally because of opacity of the samples. A possibility for forming gas-free spinning waves in solid samples has been discovered in [2]. The unsteady one-center spinning wave was realized, seemingly, in [11]. In a number of studies, a set of combustion centers was observed on the sample surface.

Analysis of the calculation results, which was carried out in this paper, allows the conclusion to be drawn that three-dimensional modeling unstable regimes for gas-free combustion is important principally. We consider the information obtained to be only the first step in investigating this complicated problem. Of urgent interest is a deeper study of the instability region for considering the problems of chaotization and chaotic flame propagation, the role of heat loss bounding regions of stable and unstable combustion with respect to various parameters, the thorough investigating nature of the non-uniqueness, and many others.

ACKNOWLEDGMENTS

The authors are grateful to professor I.P. Borovinskaya, one of the discoverers of spinning waves, for her participation in the discussion and fruitful advice.

REFERENCES

1. A. G. Merzhanov, A. K. Filonenko, and I. P. Borovinskaya, Dokl. Akad. Nauk SSSR **208**, 892 (1973).
2. Yu. M. Maksimov, A. T. Pak, G. V. Lavrenchuk, *et al*., Fiz. Goreniya Vzryva **15** (3), 156 (1979).
3. T. P. Ivleva, A. G. Merzhanov, and K. G. Shkadinskiĭ, Dokl. Akad. Nauk SSSR **239**, 1086 (1978) [Sov. Phys.–Dokl. **23**, 255 (1978)].
4. B. V. Novozhilov, Dokl. Akad. Nauk **326**, 485 (1992).
5. D. V. Strunin, Fiz. Goreniya Vzryva **29** (4), 42 (1993).
6. S. B. Shcherbak, Fiz. Goreniya Vzryva **19** (5), 9 (1983).
7. J. Puszynski, S. Kumar, P. Dimitriou, and V. Hlavacek, Z. Naturforsch. A **43**, 1017 (1988).
8. T. P. Ivleva and A. G. Merzhanov, Dokl. Akad. Nauk **369**, 186 (1999) [Dokl. Phys. **44**, 739 (1999)].
9. D. A. Frank-Kamenetskiĭ, *Diffusion and Heat Transfer in Chemical Kinetics* (Nauka, Moscow, 1987).
10. K. G. Shkadinskiĭ, B. I. Khaĭkin, and A. G. Merzhanov, Fiz. Goreniya Vzryva **7** (1), 19 (1971).
11. A. V. Dvoryankin and A. G. Strunina, Fiz. Goreniya Vzryva **27** (2), 41 (1991).

Translated by Yu. Verevochkin

Doklady Physics, Vol. 45, No. 4, 2000, pp. 142–144. Translated from Doklady Akademii Nauk, Vol. 371, No. 6, 2000, pp. 759–760.

PHYSICS

Chaotization of a Supercritical Atom

V. I. Matveev, D. U. Matrasulov,
and Corresponding Member of the RAS P. K. Khabibullaev

Received August 26, 1999

Synthesis and studying properties of superheavy chemical elements have recently turned out to be one of many urgent problems in modern physics [1, 2]. At present, a growing interest to synthesis and chemistry of actinides and transactinides stimulates intense investigating characteristics of superheavy elements. The relativistic character of superheavy atoms (we imply that due to a large electric charge of the nucleus, the motion of atomic electrons is described by relativistic equations) is one of basic features resulting in additional difficulties of such investigations. In this paper, we study the classical dynamics of a relativistic electron subjected to the action of a periodic perturbance in the electric field of a supercharged nucleus ($Z > 137$). An atom, whose nuclear charge exceeds 137, is referred to as a supercritical atom [3, 4]. Quantum-mechanical properties of supercritical atoms and quasi-classical dynamics for their energy levels, deeply embedded into the low energy continuum, have been considered in a series of papers by V.S. Popov and his coworkers [3–5]. As is well known [3, 6], the point-charge approximation is irrelevant to the relativistic-electron motion in the Coulomb field of a charge $Z > 137$. In this case, regularization of the problem should be performed with allowance for finite dimensions of the nucleus. This regularization includes the redefinition of the Coulomb potential in the following manner:

$$V(r) = \begin{cases} -\dfrac{Z\alpha}{r}, & \text{for } r > R \\ -\dfrac{Z\alpha}{b} f\left(\dfrac{r}{R}\right), & \text{for } 0 < r < R. \end{cases}$$

Here, $f(r/R)$ is a cutting function that allows for finite dimensions of the nucleus and R is the nuclear radius. In what follows, we consider the case $f(r/R) = 1$ (i.e., the charge is distributed over the nuclear surface). The relativistic momentum is defined by the expression

$$p = \sqrt{(\varepsilon - V)^2 - \frac{M^2}{r^2} - 1},$$

where ε is the electron energy and M is the orbital moment. This equation can be rewritten in the form

$$p = \begin{cases} \sqrt{\left(\varepsilon + \dfrac{Z\alpha}{r}\right)^2 - \dfrac{M^2}{r^2} - 1}, & \text{for } r > R \\ \sqrt{\left(\varepsilon + \dfrac{Z\alpha}{R}\right)^2 - \dfrac{M^2}{r^2} - 1}, & \text{for } 0 < r < R. \end{cases}$$

Turning points are defined as zeros of the momentum p. One of these points lies inside the nucleus and is given by the expression

$$r_1 = M\left[\left(\varepsilon + \frac{Z}{R}\right)^2 - 1\right]^{-1}.$$

The turning point laying outside the nucleus is determined by the equation

$$r_2 = \frac{|\varepsilon Z| - \sqrt{\varepsilon^2 Z^2 - (\varepsilon^2 - 1)(Z^2 - M^2)}}{\varepsilon^2 - 1}.$$

Therefore, the action variable allowing for finite dimensions of the nucleus (for $Z > M$) can be determined from the expression

$$\pi n = I_1 + I_2, \tag{1}$$

where

$$I_1 = \int_{r_1}^{R} \sqrt{\left(\varepsilon + \frac{Z}{R}\right)^2 - \frac{M^2}{r^2} - 1}\, dr,$$

and

$$I_2 = \int_{r_1}^{R} \sqrt{\left(\varepsilon + \frac{Z}{R}\right)^2 - \frac{M^2}{r^2} - 1}\, dr.$$

The Hamiltonian of a relativistic electron in the field of a supercharged nucleus ($Z > 137$) can be found

Department of Thermal Physics,
Academy of Sciences of Uzbekistan,
ul. Katartal 28, Kvartal Ts, Chilanzar, Tashkent,
700135 Uzbekistan

1028-3358/00/4504-0142$20.00 © 2000 MAIK “Nauka/Interperiodica”

from (1) in the action–angle variables:

$$H_0 = \varepsilon \approx -\frac{\sqrt{Z^2 - M^2}}{Z}\exp\left\{-\frac{\pi n}{\sqrt{Z^2 - M^2}}\right\}. \quad (2)$$

When deriving this expression, we took into account that $\varepsilon \sim 0$, for $Z \geq M$. The eigenfrequency is determined from the expression

$$\omega_0 = \frac{dH_0}{dn} = \frac{\pi}{Z}\exp\left\{-\frac{\pi n}{\sqrt{Z^2 - M^2}}\right\}. \quad (3)$$

It is worth noting that equation (2) is derived under the assumption $\sqrt{Z^2 - M^2} \gg R$; therefore, the dependence of H_0 on the nuclear radius is disregarded.

In the case of $Z > M$ ($r > R$), the path equation takes the form [9]

$$\frac{Z^2 - M^2}{r} = \sqrt{M^2\varepsilon^2 + (Z^2 - M^2)}\cosh\left(\phi\sqrt{\frac{Z^2}{M^2} - 1}\right) + \varepsilon Z. \quad (4)$$

For $Z \sim M$ ($\varepsilon \sim 0$), we have

$$\frac{Z^2 - M^2}{r} \approx \sqrt{M^2\varepsilon^2 + (Z^2 - M^2)}$$

$$\times (1 - \phi^2)\sqrt{\frac{Z^2}{M^2} - 1} + \varepsilon Z$$

or

$$\frac{Z^2 - M^2}{r} \approx \sqrt{Z^2 - M^2}(M - \phi\sqrt{Z^2 - M^2}) + \varepsilon Z.$$

For $r < R$, the path equation can be rewritten in the form

$$\frac{1}{r} = a_0\cos\phi, \quad (5)$$

where

$$a_0 = M^{-1}\left[\left(\varepsilon + \frac{Z}{R}\right)^2 - 1\right].$$

We now consider the interaction of this supercritical atom with a linearly-polarized monochromatic perturbing field

$$V = \epsilon\cos\omega t\sin\theta[x\sin\psi + y\cos\psi], \quad (6)$$

where θ and ψ are Eulerian angles.

The total Hamiltonian can be written out in the form

$$H = -\frac{\sqrt{Z^2 - M^2}}{Z}\exp\left\{-\frac{\pi n}{\sqrt{Z^2 - M^2}}\right\}$$
$$+ \epsilon\cos\omega t\sin\theta\sum(x_k\sin\psi\cos k\lambda + y_k\cos\psi\sin k\lambda), \quad (7)$$

where x_k and y_k are the Fourier components of the electron-dipole moment

$$x_k = \frac{i}{k\omega T}\int_0^T e^{ik\omega t}dx, \quad (8)$$

$$y_k = -\frac{i}{k\omega T}\int_0^T e^{ik\omega t}dx. \quad (9)$$

Evaluating integrals (8) and (9) by the steepest-descent method, we obtain

$$x_k = 0, \quad y_k = \frac{R^2\exp\left\{\dfrac{\pi n}{\sqrt{Z^2 - M^2}}\right\}}{\pi k^2}. \quad (10)$$

To study the stochasticity of a supercritical atom, it is necessary to find (as was carried out in [7, 8]) the resonance width

$$\Delta\nu_k = (8\omega_0' r_k\epsilon)^{1/2},$$

where $r_k = \sqrt{x_k^2 + y_k^2}$.

Employing the Chirikov's criterion [7, 8] to Hamiltonian (7), we find the critical external field from which the stochastization of the electron motion begins:

$$\epsilon_{cr} = \frac{\sqrt{Z^2 - M^2}\exp\{-\pi n/\sqrt{Z^2 - M^2}\}}{20Zk(k+1)^2(\sqrt{r_k} + \sqrt{r_{k+1}})^2}. \quad (11)$$

With regard to (10), the critical field is given by the equation

$$\epsilon_{cr} = \pi k\frac{\sqrt{Z^2 - M^2}\exp\{-2\pi n/\sqrt{Z^2 - M^2}\}}{20Z(2k^2 + 2k + 1)}. \quad (12)$$

Similarly to the consideration of [7, 8], we evaluate the diffusion coefficient

$$D = \frac{\pi}{2}\frac{\epsilon^2 R^2}{Z^3}\exp\left\{\frac{2\pi n}{\sqrt{Z^2 - M^2}}\right\}. \quad (13)$$

Thus, we have studied the stochastization process for a hydrogen-like atom with a supercharged nucleus ($Z > 137$). The analytical formulas obtained indicate that the critical field needed for the stochastization of a supercritical atom is very small. This fact is associated with the exponential dependence of Hamiltonian (2). The results obtained can be useful for studies of slow collisions of heavy ions (with the total charge of colliding ions exceeding 137) interacting simultaneously with a monochromatic radiation field.

REFERENCES

1. V. Pershina and B. Fricke, Preprint No. 98-26, GSI (Darmstadt, 1998).
2. S. Holmann, Preprint No. 99-02, GSI (Darmstadt, 1999).
3. I. Pomernchuk and Ya. Smorodinsky, J. Phys. USSR **9**, 97 (1945).
4. V. D. Mur, V. S. Popov, and D. N. Voskresenskiĭ, Pis'ma Zh. Éksp. Teor. Fiz. **28**, 140 (1978) [JETP Lett. **28**, 129 (1978)].
5. V. D. Mur and V. S. Popov, Yad. Fiz. **28**, 837 (1978) [Sov. J. Nucl. Phys. **28**, 429 (1978)].
6. V. S. Popov, D. N. Voskresenskiĭ, V. L. Eletskiĭ, and V. D. Mur, Zh. Éksp. Teor. Fiz. **76**, 431 (1979) [Sov. Phys. JETP **49**, 218 (1979)].
7. N. B. Delone, V. P. Kraĭnov, and D. L. Shepelyanskiĭ, Usp. Fiz. Nauk **140**, 355 (1983) [Sov. Phys. Usp. **26**, 551 (1983)].
8. D. U. Matrasulov, Zh. Tekh. Fiz. **69**, 127 (1999) [Tech. Phys. **44**, 249 (1999)].
9. L. D. Landau and E. M. Lifshitz, *Classical Field Theory* (Nauka, Moscow, 1973; Pergamon Press, Oxford, 1975).

Translated by V. Chechin

Doklady Physics, Vol. 45, No. 4, 2000, pp. 145–148. Translated from Doklady Akademii Nauk, Vol. 371, No. 4, 2000, pp. 469–472.

TECHNICAL PHYSICS

Scattering of Proper Waves of a Generalized Double-Sided Slot Waveguide by a Slot-Width Jump

E. I. Nefedov* and R. S. Popov**

Presented by Academician O.M. Belotserkovskiĭ April 6, 1999

Received June 3, 1999

1. Nowadays, advances of activity in fundamental science representing the basis of the pioneering technology and also in commerce (a small-scale and large-scale business), etc. depend principally on the possibility and ability of gaining and properly processing large and super-large data arrays. This fact implies the urgent necessity in convenient and reliable systems of high-performance data processing [1]. The design of such systems satisfying a variety of requirements for quality, high performance, cost, etc. is impossible without using three-dimensional integrated circuits capable of operating in microwave and extremely high-frequency wave ranges [2].

For solving the problem of designing basis components of three-dimensional integrated circuits ("structural units" of these integrated circuits), it is necessary to have good mathematical models for both transmission lines and various-type heterogeneities in them (basis components). Such models must primarily satisfy the requirement for consistency with the actual physical conditions. Indeed, for example, after a monolithic chip has been fabricated, it is impossible to a designer "manual" refining a ready device. This requirement is well satisfied by the mathematical models for transmission lines and their heterogeneities, which are constructed on the basis of a rigorous electrodynamic approach. (We imply, e.g., the method of partial domains [3–5], as well as the universal analytical method based on solving singular integral equations with application of the Schwinger transformation [4]).

In this paper, we formulate and solve the problem of transmitting a proper electromagnetic wave through a jump of a slot width in a generalized double-sided slot waveguide. The solution is given by both the rigorous electrodynamic method and using the approximate model based on the classical theory of a long transmission line. This is the key problem for three-dimensional integrated circuits operating in the microwave and extremely high-frequency wave ranges.

2. A generalized double-sided slot waveguide presents two connected slots of arbitrary widths and arbitrarily arranged with respect to each other on different sides of a dielectric plate [6]. The natural model of this waveguide is a structure placed in a rectangular waveguide, i.e., the closed model of a generalized double-sided slot waveguide. Such a model makes it possible to obtain characteristics of guided waves with a reasonable accuracy also for an open structure by means of removing screen walls at a distance on the order of the wavelength λ_0 in free space [6]. The electrodynamic characteristics of the regular generalized double-sided slot waveguide were investigated by both approximate and exact methods [6]. Here, the solution to this part of the problem is assumed to be known.

The model of a long transmission line is used for estimates and can also be applied as a zero approximation in a more rigorous analysis. The basis of this approach is an assumption of the conservation of the wave type in the case of the jump-like change in parameters of the transmission line. Under the condition of the conservation of the single-wave regime of the transmission line both ahead and back of the jump of the parameters, the coefficient of wave reflection from the joint of two transmission lines with wave resistances Z_1 and Z_2 can be determined from the following expression:

$$|R| = \left|\frac{Z_2 - Z_1}{Z_2 + Z_1}\right|.$$

Electrodynamic approach. Let the fundamental wave of the waveguide *A* be incident on a segment with the jump-like change in a slot width (waveguide *B*) (Fig. 1). When a wave is incident on a heterogeneity, a part of the wave is reflected backward into the waveguide *A*. There, it is redistributed between the fundamental and highest-type waves. The other part of the

* *Institute for Computer-Aided Design, Russian Academy of Sciences, Fryasino, Moscow oblast, 141120 Russia*

** *Institute of Radio Engineering and Electronics, Russian Academy of Sciences, Fryasino, Moscow oblast, 141120 Russia*

1028-3358/00/4504-0145$20.00

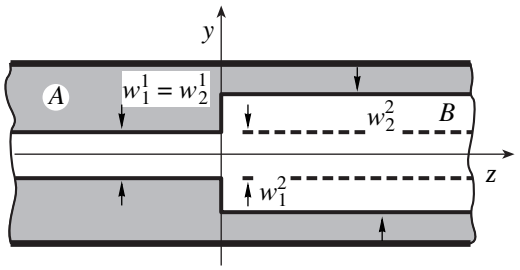

Fig. 1. Geometry of a heterogeneous section for a generalized double-sided slot waveguide.

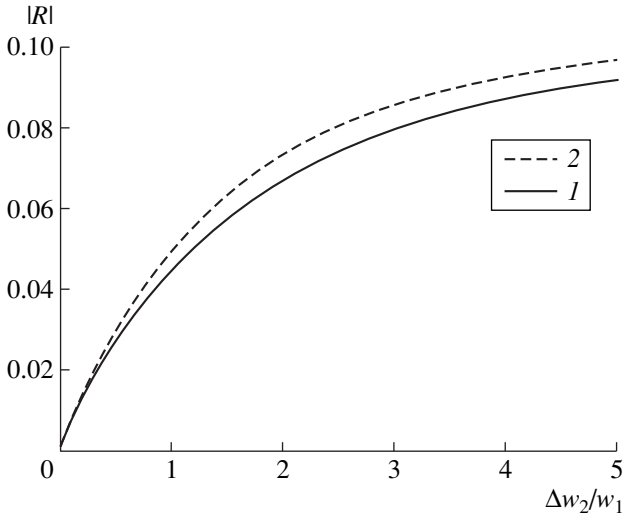

Fig. 2. Reflection coefficient for the fundamental wave of a generalized double-sided slot waveguide, which is reflected from a symmetric jump in the second-slot width, as a function of the jump magnitude: f = 20 GHz, ε_r = 2.22, $w_1 = w_2^1$ = 0.1 mm, d = 0.254 mm, $h_1 = h_2$ = 3.42 mm, and b = 3.56 mm.

wave goes into the waveguide *B*, whose total field also represents the superposition of all waves of this waveguide.

We represent the fields of proper waves of the waveguides *A* and *B* in the form

$$\tilde{e}_{ai,bj}(x, y, z) = \begin{pmatrix} a_i \\ b_j \end{pmatrix} \mathbf{e}_{ai,bj}(x, y) \exp(\mp\gamma_{i,j} z),$$

$$\tilde{h}_{ai,bj}(x, y, z) = \begin{pmatrix} a_i \\ b_j \end{pmatrix} \mathbf{h}_{ai,bj}(x, y) \exp(\mp\gamma_{i,j} z).$$

Here, i and j are the subscripts of the proper waves for the waveguides *A* and *B*, respectively; a_i and b_j are the amplitude coefficients of the proper waves; γ_{ij} are the propagation constants for the proper waves (the signs minus and plus correspond to waves propagating in the positive and negative directions of the *z*-axis, respectively), the fields of the waveguides *A* and *B* being sewn in the jump plane. If we impose the condition of continuity for the transverse components of the total electromagnetic field and the condition of vanishing the tangential components of the electric field at a metal surface, we obtain the set of linear algebraic equations with respect to the coefficients $\bar{a}_i$ and $\bar{b}_j$:

$$\rho I_{a1bn} + \sum_{i=2}^{\infty} \bar{a}_i I_{aibn} - \sum_{j=1}^{\infty} \bar{b}_j I_{bjbn} = -I_{a1bn},$$

$$\rho I_{ama1} + \sum_{i=2}^{\infty} \bar{a}_i I_{amai} + \sum_{j=1}^{\infty} \bar{b}_j I_{ambj} = -I_{ama1},$$

$$I_{aibj} = \int_S \mathbf{e}_{ai} \times \mathbf{h}_{bj} d\mathbf{S}.$$

Here, the normalization condition is

$$\int_S \mathbf{e}_i \times \mathbf{h}_j d\mathbf{S} = \delta_{ij},$$

where δ_{ij} is the Kronecker delta; and **S** is the cross section of the waveguide structure.

3. The reflection coefficient for the fundamental wave as a function of a magnitude of the slot-width jump is presented in Fig. 2 (curve *1*). In this case, the parameters of the transmission line are chosen in such a way that, at a given frequency, the single-wave regime takes place in both semi-infinite sections of the line (both in the waveguide *A* and waveguide *B*). In the same figure, we present the similar dependence obtained from the theory of a long transmission line (curve *2*). It is evident that this approximate model is quite acceptable for describing the slot-width jump of the generalized double-sided slot waveguide in the single-wave regime in regular transmission lines arranged on both sides of a heterogeneity.

A priori, it is clear that for low and high magnitudes of a jump in parameters of the waveguide structure, the value of the reflection coefficient must tend to zero and to that of the reflection coefficient from the infinite jump, respectively. It is also clear that, with increasing magnitudes of such a jump, the scattering characteristics of a heterogeneity depend less on its particular value (i.e., the characteristic must tend to "saturation"). The behavior of the curves presented in Fig. 2 is in complete agreement with the above considerations.

The modulus of reflection coefficient *R* as a function of the frequency is shown in Fig. 3 for a fundamental wave reflected from the joint between two semi-infinite sections of generalized double-sided slot waveguides. The presence of maxima and minima for the reflection and transmission coefficients is caused by the passage of the first highest-type wave from the cut-off domain to the running-wave domain. The reflection coefficient

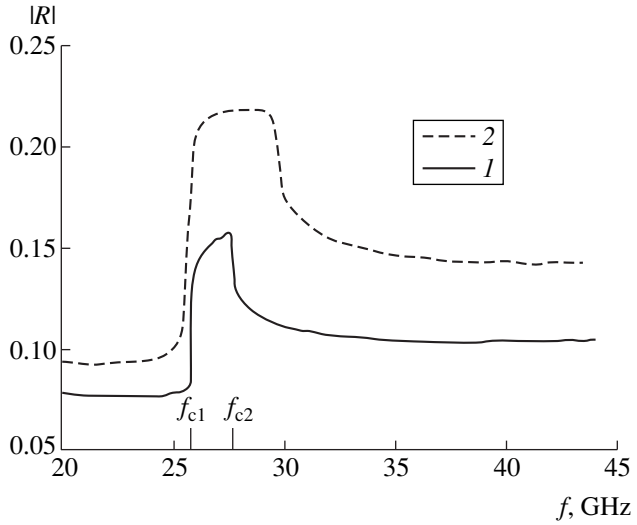

Fig. 3. Modulus of the reflection coefficient for the fundamental wave in a generalized double-sided slot waveguide as a function of the frequency. The reflection occurs from the symmetric jump in the width of the second slot: ε_r = 2.22, $w_1 = w_2^1$ = 0.1 mm, d = 0.254 mm, $h_1 = h_2$ = 3.42 mm, b = 3.56 mm; $\Delta w_2/w_1$ = (*1*) 2.8; (*2*) 5.5.

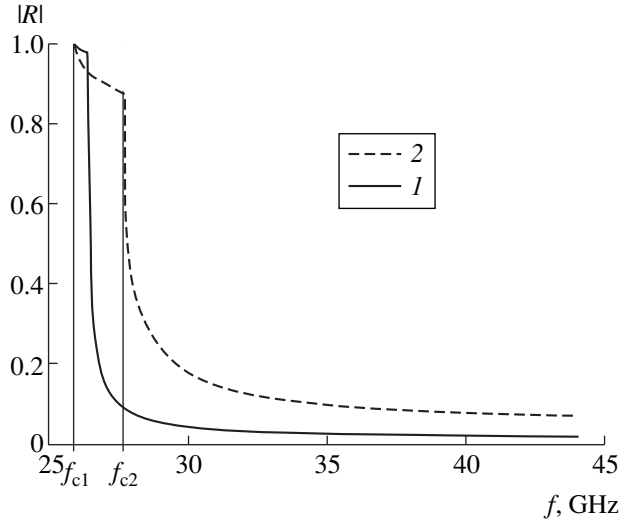

Fig. 4. Modulus of the reflection coefficient for the first highest-type wave of the generalized double-sided slot waveguide as a function of the frequency. The reflection occurs from the symmetric jump in the width of the second slot: ε_r = 2.22, $w_1 = w_2^1$ = 0.1 mm, d = 0.254 mm, $h_1 = h_2$ = 3.42 mm, b = 3.56 mm. (*1*) $\Delta w_2/w_1$ = 0.69; (*2*) $\Delta w_2/w_1$ = 2.8.

for the fundamental wave in the low-frequency region (section *1* in Fig. 3) behaves monotonically. This coefficient has a very low absolute value (compared to the reflection from the fin-line joint with the same geometry parameters) up to the cut-off frequency (f_{c1}) for the first highest-type wave in the waveguide *A*. Nearby this frequency, the curve begins to rise steeply and attains its maximum at the cut-off frequency of the first highest-type wave in the waveguide *B* (f_{c2}, segment *2* in Fig. 3). Furthermore, the amount of energy reflected into the fundamental wave of the waveguide *A* decreases sharply to a certain value, whose modulus exceeds the energy reflected in the single-wave regime. The mechanism governing the transformation of the fundamental-wave energy into that of highest-type waves implies that a symmetric slot-width jump of the generalized double-sided slot waveguide has properties of a band-rejection filter (rejecter). The *Q*-factor of this filter depends substantially on a magnitude of the jump in parameters of the generalized double-sided slot waveguide and decreases with increasing the difference $w_2^2 - w_2^1$ (cf. curves *1* and *2* in Fig. 3).

The modulus of the reflection coefficient *R* as a function of the frequency is presented in Fig. 4 for the first highest-type wave of the generalized double-sided slot waveguide. In the frequency region lower than f_{c1}, the highest-type wave turns out to be in the cut-off regime. At a frequency close to f_{c1}, we have $|R| \longrightarrow 1$ (Fig. 4). Therefore, all the remaining scattering parameters for the jump tend to zero. Thus, the electromagnetic energy transported by the first highest-type wave (near its cut-off frequency) is totally reflected from a transmission-line heterogeneity. With increasing the frequency, the absolute value of the reflection coefficient decreases weakly. This decrease is caused by the increasing energy exchange between the incident wave and the fundamental waves of the waveguides *A* and *B*. Since the propagation constants for these waves and the field configurations in the transverse cross section differ considerably, then the energy-exchange is also rather small. Therefore, the reflection coefficient $|R|$ decreases weakly from unity up to the frequency f_{c2}. As in the case when the fundamental wave of the generalized double-sided slot waveguide passes through a heterogeneity, the energy transformation from one wave type to another increases with the absolute value of the jump (cf. curves *1* and *2* in Fig. 4). This fact results in a decrease in the *Q*-factor of the total reflection of the wave near its cut-off frequency with increasing the difference in parameters of the transmission line ahead and back of the joint.

It is necessary to note that the similar behavior of the reflection coefficient for highest-type waves nearby their cut-off frequencies takes place in the case when the electromagnetic wave is incident onto an open end of the waveguide [7, 8]. This fact made it possible, in due time, to design a new class of resonance structures, called open resonators, having a more rarefied spectrum of eigenfrequencies compared to closed resonance structures [8]. A certain interest lies also in structures based on generalized double-sided slot waveguides with a smooth variation of parameters along the transmission line. Based on them, in particular, it is possible to develop, resonators with "nonfocusing mirrors" having a uniform (equidistant) spectrum

of eigenfrequencies. In other words, in this case, the spectrum of a string is realized in the open resonator [9].

4. Thus, we have investigated characteristics of scattering for a symmetric jump in the width of a single slot of a generalized double-sided slot waveguide. It has been shown that the reflection coefficient for the fundamental wave reflected from the joint of two semi-infinite segments of the generalized double-sided slot waveguide has a very small absolute value compared to the reflection from the fin-line joint with the same geometry parameters. Moreover, the slot-width jump has the filtering properties, and we can safely use it for these purposes, while designing the basis components of microwave three-dimensional integrated circuits. The modulus of the reflection coefficient for the first highest-type wave in the generalized double-sided slot waveguide tends to unity near its cut-off frequency similarly to the case of the incidence of an electromagnetic wave onto the waveguide open end [7, 8].

ACKNOWLEDGMENTS

This work was supported by the Air Force Research Laboratory (AFRL, Hanscom, Boston, USA), contract no. F61708-96-W0266 and by the International Scientific and Technological Center (ISTC), project no. 1023.

The authors are grateful to M. Davidovitz (AFRL) for his support of this work and discussion of its results, A.D. Shatrov for his very valuable comments and advises, and V.N. Gridin for his help in the course of this work.

REFERENCES

1. E. I. Nefedov, *Modern Radioelectronics* (Nauka, Moscow, 1986).
2. V. I. Gvozdev and E. I. Nefedov, *Microwave Three-Dimensional Integrated Circuits* (Nauka, Moscow, 1985).
3. B. Bhat and S. K. Koul, *Analysis Design and Application of Fin-Line* (Artech House, New York, 1987).
4. V. A. Neganov, E. I. Nefedov, and G. P. Yarovoĭ, *Strip–Slot Structures for Microwaves and Extremely High-Frequency Waves* (Nauka, Moscow, 1996).
5. K. C. Gupta, R. Garg, I. Bahl, and P. Bhartia, *Microstrip Lines and Slot Lines* (Artech House, Boston, 1996).
6. E. I. Nefyodov and R. S. Popov, in *IEEE AP-S International Symposium and URSI Radio Science Meeting*, 1997 (Montreal, Canada, 1997), Vol. 1, p. 210.
7. E. I. Nefedov and A. T. Fialkovskiĭ, *Strip Communication Lines. Electrodynamic Principles for Computer-Aided Design of Microwave Integrated Circuits* (Nauka, Moscow, 1980).
8. L. A. Vaĭnshteĭn, *Open Resonators and Open Waveguides* (Sov. Radio, Moscow, 1966).
9. E. I. Nefedov, *Open Coaxial Resonance Structures* (Nauka, Moscow, 1982).

Translated by V. Bukhanov

Doklady Physics, Vol. 45, No. 4, 2000, pp. 149–154. Translated from Doklady Akademii Nauk, Vol. 371, No. 5, 2000, pp. 611–616.

TECHNICAL PHYSICS

Robust Algorithms of Image Filtration in the Presence of Additive, Multiplicative, and Impulse Noises

V. F. Kravchenko*, Corresponding Member of the RAS V. I. Pustovoĭt, V. I. Ponomarev***, and A. B. Pogrebnyak*****

Received July 21, 1999

1. Systems for remote probing of the Earth's surface, which are based on spacecraft or aircraft, are widely used all over the world for both the ecological and agricultural monitoring and for the prospecting of natural resources [1–4]. Unfortunately, the quality of the initial images is often unacceptable so that to ensure both the desired reliability and the adequate interpretation of remote-probing data. Because of this, improving the image quality is one of the first stages as remote-probing data are processed [1, 2, 4]. The analysis of features intrinsic in, for example, radar images allows the following conclusions: As a rule, remote-probing data are distorted because the resolution of remote-probing systems is insufficient. The radar images are significantly distorted by random noise, which is a complex composition of both the Gaussian additive and multiplicative noises and a process of random pips. Under such conditions, the algorithms of the image-data processing must ensure the effective noise suppression and reproduction of well-defined borders on the images.

In this paper, we present new robust filtration algorithms applicable to radar-data processing. These algorithms are based on the robust theory of point estimates and combine ranked and robust maximum likelihood estimates (*R*- and *M*-estimates, respectively). The *RM*-filters obtained improve the quality of images (in particular, radar images under consideration) by means of the effective suppression of specl- and impulse noises to ensure the reproduction of well-defined borders on the images. Usually, a linear filtration consistent with the additive Gaussian noise is performed in receivers. Then, an image is formed in the remote-probing system on the basis of the principle of *a posteriori* Bayes minimum risk [1]. As was proved, for example, in [1, 2], such a method can ensure the restoration of slurred-over images and, to a certain degree, diminish the influence of multiplicative noise. Unfortunately, the realization of such algorithms significantly complicates the present-day remote-probing systems because the environmental parameters that are used to eliminate a parametric uncertainty of the original signals should be estimated. In addition, this method ignores impulse noise. At the output of an image former in the remote-probing system, the signal, after it has been consistently filtered and transformed into a digital form, can be written out in the form

$$q(x, y) = n_{\text{im}}(x, y[\Psi(\Delta x, \Delta y)* \times [n_e(x, y)e(x, y)] + n(x, y)]). \quad (1)$$

Here, $e(x, y) = |\dot{\mathbf{e}}(x,y)|$, $|\dot{\mathbf{e}}(x,y)|$ is the original complex-valued radar image; $n(x, y)$ is the additive receiver noise; $\Psi(\Delta x, \Delta y)$ is the positive point-scattering function; and $n_e(x, y)$ is the multiplicative noise determined by the signal reflection at a rough surface. The functional $n_{\text{im}}(x, y, s(x, y))$ denotes the impulse noise due to shot effects and has the form

$$n_{\text{im}}(x, y, s(x, y)) = \begin{cases} P_i, & \text{a pip with random amplitude} \\ 1 - P_i, & \text{otherwise.} \end{cases} \quad (2)$$

The high resolution of the image formers similar to a radar with a synthesized aperture is their main advantage. However, the images formed by such systems are significantly distorted by multiplicative specl-noise. If the influence of the point-scattering function is assumed to be restricted and determined by the width of its main lobe, then equation (1) can be used as a model of the signal and noise for the images at the output of the radars with synthesized apertures. It follows from the aforesaid that the radar images formed need the image noise filtration to be applied. At the same time, *a priori* information on the signal and noise distribution is complicated enough to be exactly analyzed. Because of this, *a priori* uncertainty related to both the type and the

* *Institute of Radio Engineering and Electronics, Russian Academy of Sciences, Mokhovaya ul. 11, Moscow, 103907 Russia*

** *Central Design Bureau of Unique Instrumentation, Russian Academy of Sciences, ul. Butlerova 15, Moscow, 117342 Russia*

*** *Kharkov State Aerospace University, Kharkov, Ukraine*

National Polytechnical Institute of Mexico, Mexico (City), Mexico

1028-3358/00/4504-0149$20.00 © 2000 MAIK "Nauka/Interperiodica"

parameters of the signal and noise distributions, which is usually eliminated on the basis of parametric approaches, will be settled below with the help of nonparametric methods.

2. In the literature on image processing [10–12], a number of nonlinear noise filtration methods, which were based on heuristic approaches, has been recently presented and studied. In contrast to heuristic methods, we here propose new robust image filters based on the classical theory of restoration and filtration of images, i.e., on the methods of robust point *R*- and *M*-estimates. In the classical linear theory of restoration, because of physical restrictions of the detectors in image formers, image distortions are often described as a linear shift modeled by the convolution operator in the presence of the Gaussian additive noise. The Wiener optimum linear filter [1, 2] is a known solution to such an inverse problem. In a spatial domain, such a filter can be realized by locally averaging the readings inside a moving square window scanning the image:

$$\hat{s}(i, j) = \frac{1}{(2K+1)^2}\sum_{m=-K}^{K}\sum_{n=-K}^{K} u(i-m, j-n), \quad i = 1, \ldots, M, \ j = 1, \ldots, N, \ M \times N. \tag{3}$$

Here, $\hat{s}(i, j)$ is the image estimate, $u(i, j)$ is the original image distorted by the Gaussian noise, $2K + 1$ is the moving-window size along both of the coordinate axes, and i and j are the running coordinates. Algorithm (3) is widely known as the standard linear smoothing filter, which is optimum only if both the image and the noise have the Gaussian distribution. Usually, this assumption is not valid for various types of images, in particular, for radar images formed by remote-probing systems. However, expression (3) can be used as a generating equation to find image filters with more acceptable noise-suppression properties. Namely, instead of the local arithmetic average, one can use robust estimates for a local average of the readings inside the moving window.

Average ranked estimates *R* belong to a class of nonparametric robust estimates based on statistical inferences from the theory of ranked criteria [14]. The sample median is a fairly-known ranked estimate. This estimate is obtained with the use of the most powerful ranked test, namely, the sign test, provided that *a priori* information on the distribution of the data X_i is entirely absent. Another well-known ranked estimate to be used below is the Wilcockson's *R*-estimate

$$\theta_{\text{Wil}} = \hat{\theta}_T = \operatorname*{med}_{i \le j}\{0.5(X_i + X_j)\}.$$

This estimate follows from the most powerful test, namely, the ranked criterion for the Wilcockson's sign ranks provided the distribution of initial data has a symmetric form.

The generalized form of the equation for robust *M*-estimates has been proposed in [13]:

$$\sum_{i=1}^{n}\psi(X_i - \theta) = 0, \ \psi(X, \theta) = \frac{\partial}{\partial\theta}\ln(f(X, \theta)),$$

where $f(X)$ is the probability density function for the sample data X_i and θ is a shift. The *M*-robust solution to the estimate θ is determined by imposing certain restrictions on the function $\psi(X)$ or the samples $X_i - \theta$. The simplest restriction on the range of the function $\psi(X)$ is the *M*-estimate for the normal distribution with long "tails" [13]:

$$\tilde{\psi}(X) = \min(b, \max(X, -b)) = [X]_{-b}^{b}. \tag{4}$$

Another way for obtaining the function $\tilde{\psi}(X)$ is disregarding anomalous readings, namely, pips over the initial data sample. This leads to the so-called lowered *M*-estimates. As was proved in paper [13], the cut median

$$\psi_{\text{med}[r]}(X) = \begin{cases}\text{sgn}(X), & |X| \le r\\ 0, & |X| > r\end{cases} \tag{5}$$

is the most robust lowered *M*-estimate. To keep the calculations down, we use below the simple cut function

$$\psi_{\text{cut}(r)}(X) = \begin{cases}X, & |X| \le r\\ 0, & |X| > r\end{cases} \tag{6}$$

to find the robust lowered *M*-estimates.

When deriving the filtration algorithms, we employ the simplified single-step method for calculating the lowered *M*-estimates of the average θ-value:

$$\theta_{\text{M}} \approx \frac{\sum_{i=1}^{n} X_i\tilde{\psi}(X_i - \text{med}\{\mathbf{X}\})}{\sum_{i=1}^{n} 1_{[-r, r]}(X_i - \text{med}\{\mathbf{X}\})}. \tag{7}$$

Here, $\tilde{\psi}$ is the normalized ψ-function: $\psi(X) = X\tilde{\psi}(X)$. It is evident that formula (7) represents the arithmetic average of $\sum_{i=1}^{n}\psi(X_i - \text{med}\{\mathbf{X}\})$, which is evaluated on the interval $[-r, r]$.

3. In the approach under consideration, instead of the arithmetic averaging in relation (7), we use *R*-estimates similar to the median average and Wilcockson's ones:

$$\theta_{\text{med}\,\mathbf{M}} = \text{med}\{X_i\tilde{\psi}(X_i - \text{med}\{\mathbf{X}\}), \ i = 1, \ldots, n\}, \tag{8}$$

$$\theta_{\text{Wil}\,\text{M}} = \operatorname*{med}_{i \le j}\{0.5[X_i\tilde{\psi}(X_i - \text{med}\{\mathbf{X}\}) + X_j\tilde{\psi}(X_j - \text{med}\{\mathbf{X}\})], \ i = 1, \ldots, n\}. \tag{9}$$

As is to be expected, new *RM*-estimates (8) and (9) have robust properties superior to those for the basic *R*- and *M*-estimates. As was noted above, ranked image filters (*R*-filters) can be easily obtained from generating equation (3) by changing from the arithmetic averaging to the universal ranked estimate. Choosing the ranked estimate in the form of the median one and performing the corresponding substitutions, we obtain a standard median filter. A more complicated rank estimate based on the Wilcockson's criterion determines the Wilcockson's standard filter [7, 8, 10]. To increase the robustness of standard filters, one can employ the methods known in the robust-estimate theory, for example, the censoring or others [9, 14]. The application of a censoring operation to a linear smoothing filter determines the α-censored filter (α-TM filter) [8, 10]:

$$\hat{e}_{\alpha\text{-TM}}(i, j) = \frac{1}{L - 2\alpha L}\sum_{k=\alpha L}^{L-\alpha L} R_q(k), \qquad (10)$$

where $L = (2K + 1)^2$ and $R_q(k)$ is the reading having the kth rank among the window elements $q(i + m, j + n)$ ($m, n = -K, \ldots, K$). Using the censoring in the Wilcockson's estimate and changing the arithmetic average in generating equation (3), we can easily obtain the Wilcockson's censored filter (Wilcockson's α-TM filter) [9, 10]:

$$\hat{e}_{\text{W }\alpha\text{-TM}}(i, j) = \operatorname*{med}_{k \le l}\left\{\frac{R_k + R_l}{2}\right\}, \qquad (11)$$

$$k, l = \alpha L, \ldots, L - \alpha L, \; L = (2K + 1)^2.$$

The proposed method for constructing new robust filters of the *RM*-type employs generating equation (3), robust estimates (7)–(9), and various influence functions $\psi(X)$.

The standard *M*-filter [11] is obtained with the use of the function $\psi(X)$ given by expression (4):

$$\hat{e}_{\text{STM}}(i, j) = \frac{1}{2K + 1}\sum_{m=-K}^{K}\sum_{n=-K}^{K}\tilde{\psi}(g(i + m, j + n)), \qquad (12)$$

where

$$\tilde{\psi}(g(i, j)) = \begin{cases} \hat{e}_{\text{med}}(i, j) - b, & g(i, j) < b, \\ q(i, j), & g(i, j) \le b \\ \hat{e}_{\text{med}}(i, j) + b, & g(i, j) > b, \\ g(i + m, j + n) = q(i + m, j + n) - \hat{e}_{\text{med}}(i, j). \end{cases}$$

Using *RM*-estimate (9), we obtain the Wilcockson's standard *M*-filter

$$\hat{e}_{\text{WSTM}}(i, j) = \operatorname{med}\left\{\frac{y_k + y_l}{2}, k \le l\right\}, \qquad (13)$$

$$\mathbf{y} = [\tilde{\psi}(g(i + m, j + n)), m, n = -K, \ldots, K],$$

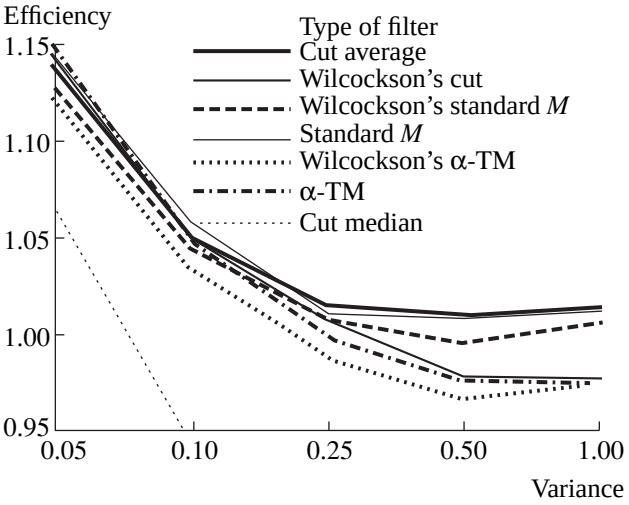

Fig. 1. Simulation results for Rayleigh multiplicative noise.

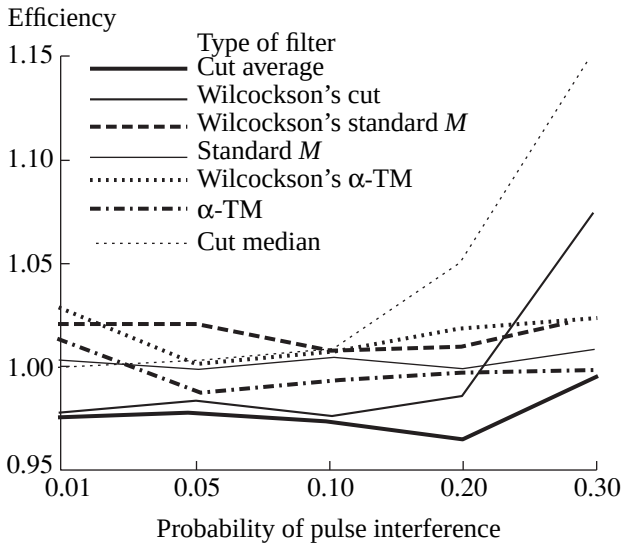

Fig. 2. Data processing results for images distorted by impulse noise.

where $k, l = -K, \ldots, K$ and the vector $\mathbf{y}$ denotes an intermediate sequence of data. Similarly, using cutoff function (6) in (7) and performing corresponding changes in (3), we obtain the cutoff *M*-filter

$$\hat{e}_{\text{CM}}(i, j) = \frac{1}{\sum\psi_{\text{cut}}(\mathbf{g}(i, j))}\sum_{m=-K}^{K}\sum_{n=-K}^{K}\psi_{\text{cut}}(\mathbf{g}(i, j))\mathbf{q}(i, j), \qquad (14)$$

$$\psi_{\text{cut}}(g(i, j)) = \begin{cases} 1, \text{ if } g(i, j) \le b \\ 0, \text{ if } g(i, j) > b, \end{cases}$$

where $g(i, j) = |q(i, j) - \text{med}\{\mathbf{q}(i, j)\}|$, $\mathbf{g}(i, j) = g(i + m, j + n)$, $\mathbf{q}(i, j) = q(i + m, j + n)$, with $m, n = -K, \ldots, K$.

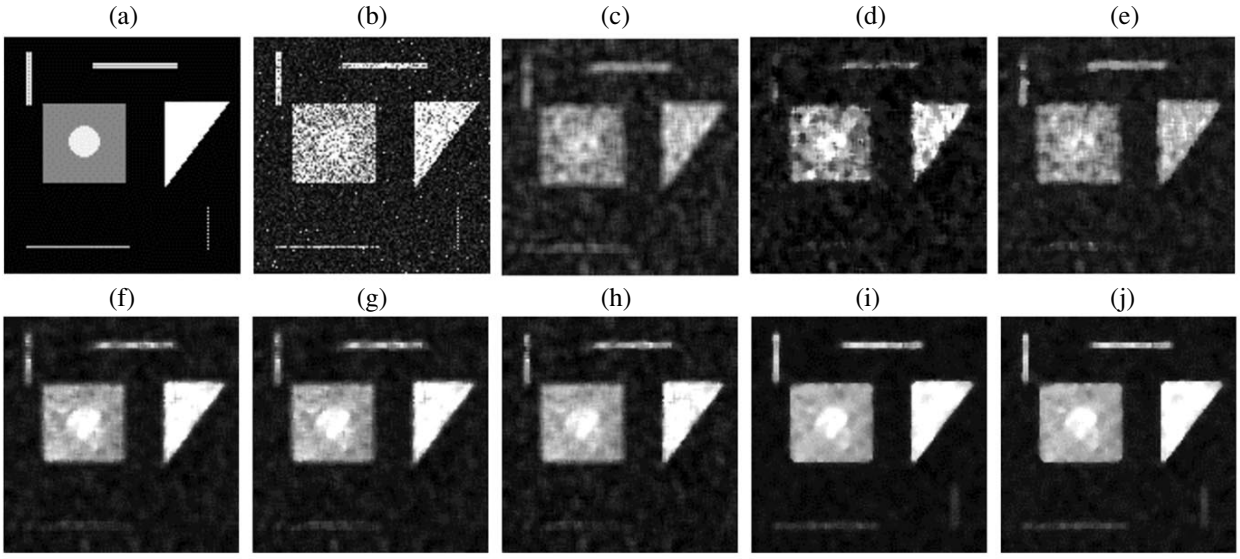

Fig. 3. (a) Initial test image, (b) model image typical for radars with synthesized apertures; outputs for various types of filters: (c) linear smoothing, (d) median, (e) Wilcockson's, (f) standard TM-, (g) Wilcockson's standard TM-, (h) cut average, (i) Wilcockson's cut, and (j) cut median.

Using *RM*-estimate (9) in (14), we obtain the Wilcockson's cutoff *M*-filter

$$\hat{e}_{\mathrm{WCM}}(i, j) = \mathrm{med}\left\{\frac{y_k + y_l}{2}, k \le l\right\}. \quad (15)$$

$$\mathbf{y} = \{q(i+m, j+n): |q(i+m, j+n) - \mathrm{med}\{q(i+m_1, j+n_1)\}| \le b\}, \quad m, n, m_1, n_1 = -K, \ldots, K. \quad (16)$$

The cutoff median filter is found by using *RM*-estimate (8) in (12):

$$\hat{e}_{\mathrm{MCM}}(i, j) = \mathrm{med}\{\mathbf{y}\}. \quad (17)$$

Here, the vector **y** is determined by expression (16).

4. We have performed a series of various tests to study properties of new algorithms (13), (14), (15), and (17). In addition, we have compared them with known relations (3) and algorithms (11) and (12). Filtration criteria were the mean-square error, the correlation coefficient ρ, and the noise-suppression efficiency $\varepsilon = 1/(2(1-\rho))$. To compare various filters, we use the convenient criterion for the relative efficiency of the noise suppression $\varepsilon_r = \varepsilon/\varepsilon_{rf}$, where ε_{rf} is the efficiency of a calibrating filter. To estimate and compare various filters, we performed the filtration of the test image shown in Fig. 3a by all the above-mentioned filters. In this case, we set the following parameters of the filters: the window measures 5×5 readings for all the filters, the censoring coefficient for filters (10) and (11) is α = 30%, and the adaptation parameter for filters (12)–(15) and (17) is b = 65. The simulation results suggest that filters (11) and (13) have the best properties in respect to the reproduction of well-defined borders on the images. Filter (12) has the worst response to a step signal (almost as the standard linear smoothing filter). To obtain quantitative characteristics of the noise suppression by the filters under consideration, we distorted the standard image "Lena" by noises with various distributions, namely, by the Gaussian additive white, Rayleigh multiplicative, and impulse noises. In this case, we vary the parameters of both the filters and the noises: the window size from 3×3 to 5×5 readings, the censoring coefficient α for filters (10) and (11) from 5 to 45%, and the adaptation parameter b from 5 to 250. The simulation results for Rayleigh multiplicative noise (with the linear smoothing filter serving as a calibrating one) are shown in Fig. 1. The data processing results for the images distorted by impulse noise (with the median filter serving as a calibrating one) are shown in Fig. 2. It follows from the visual comparative analysis of the figures that the *RM*-filters have an intermediate quality of filtration for various types of noises. Filter (13) ensures the best results provided the noise level is low and the window aperture is small. Wilcockson's cutoff filter (15) has the best quality provided the noise level is high. In addition, both the *RM*-filters ensure more well-defined borders on the images in comparison to analogous *M*-filters (12) and (14). To model noisy images typical for remote-probing systems, we distorted an original image (see Fig. 3a) by Rayleigh multiplicative noise with the variance of 0.25, convolved it with the uncertainty function $\Psi(\Delta x)\Psi(\Delta y)$, and, in addition, distorted by Rayleigh additive noise with the relative variance of

Simulation results of model images typical for radars with (*a*) lateral survey and (*b*) synthesized aperture

Type of filter (window size of 5×5 readings)	(*a*)		(*b*)	
	mean-square error	optimum values, b, α	mean-square error	optimum values, b, α
Linear smoothing	510.2	–	632.6	–
Median	636.8	–	466.0	–
Standard *M*-, (12)	508.6	5	460.3	15
Wilcockson's standard *M*-, (13)	509.5	10	463.8	20
Cut average, (14)	476.6	55	411.6	60
Wilcockson's cut, (15)	472.1	55	407.1	60
Cut median, (17)	458.5	60	395.9	80
α-TM-, (10)	510.4	45%	461.9	45%
Wilcockson's α-TM-, (11)	510.7	45%	461.9	45%

0.05 and by impulse noise with the pip probability of 0.01. To model images typical for radars with synthesized apertures, we distorted the original test image by Rayleigh multiplicative noise with the variance of 1.0, convolved it with the uncertainty function $\Psi(\Delta x) \times \Psi(\Delta y)$, added to Rayleigh additive noise with the relative variance of 0.05, and distorted by impulse noise with the pip probability of 0.01. The table lists quantitative characteristics of data processing for remote-probing model images and corresponding optimum tuning coefficients for the filters under consideration. It follows from the table that the *RM*-filters, on the whole, ensure the high quality of the remote-probing images processed. Both the cut average and Wilcockson's α-*TM* filters ensure the maximum noise suppression on the model image (*a*) typical for radars with lateral survey, provided the original test image distorted by a convolution serves as a calibrating one. Both the Wilcockson's cut and median cut filters ensure the best quality of images in respect to the minimum mean-square error for the model images under consideration.

The filtration results for a model image typical for radars with synthesized aperture are shown in Fig. 3 (the corresponding parameters are given in the table). Figure 3b shows the model image distorted as was described above. It follows from a visual comparative analysis of Fig. 3 that the best qualitative results are ensured by filters (15) and (17). They effectively suppress noise and reproduce well-defined borders on the images, with the cutoff median filter slightly distorting these borders. The *M*-filters insufficiently reproduce well-defined borders, while the standard filters (linear smoothing, median, and Wilcockson's ones) insufficiently suppress noise.

5. Thus, here we proposed and analyzed new robust *RM*-filters for the processing of remote-probing images, which use basic positive features of the *M*- and *R*-filters. It follows from our simulation results that all the *RM*-filters under consideration adequately reproduce well-defined borders on the images and suppress impulse noise. In actual practice, when noise is spatially correlated and involves anomalous interference, both of the standard filters, namely, the median and linear filters, do not ensure adequate noise suppression. In this case, the *RM*-filters described above make it possible to obtain images with high visual quality and better quantitative characteristics of noise suppression in comparison with the basic *M*-filters. The useful properties of the *RM*-filters may be due to their local adaptability associated with the method of calculating the *M*- and *R*-estimates.

REFERENCES

1. S. E. Fal'kovich, V. I. Ponomarev, and Yu. V. Shkvarko, *Optimum Receiving of Space-Time Signals in Radio Channels with Dissipation* (Radio i Svyaz', Moscow, 1989).
2. A. A. Goncharenko, V. F. Kravchenko, and V. I. Ponomarev, *Remote Probing in Heterogeneous Media* (Mashinostroenie, Moscow, 1991).
3. S. G. Zubkovich, *Statistic Characteristics of Signals Reflected from Earth's Surface* (Sov. Radio, Moscow, 1968).
4. V. N. Antipov, V. T. Goryainov, A. N. Kulin, *et al.*, *Radar Units with Digital Synthesis of Antenna Aperture* (Radio i Svyaz', Moscow, 1988).
5. J.-O. Eklund, T. S. Huang, B. J. Justusson, *et al.*, *Two-Dimension Digital Signal Processing. Transforms and Median Filters* (Berlin, 1981; Radio i Svyaz', Moscow, 1984).
6. J. Astola and P. Kuosmanen, *Fundamentals of Nonlinear Digital Filtering* (CRC Press, Boca Ratón, New York, 1997).

7. R. J. Crinon, in *Proceedings of IEEE International Conference Acoustics, Speech and Signal Processing*, 1985, pp. 668–671.
8. J. H. Lee and J. S. Kao, in *Proceedings of IEEE Symposium on Circuits and Systems*, 1987, pp. 268–271.
9. P. P. Gandhi and S. A. Kassam, in *Proceedings of IEEE Symposium on Circuits and Systems*, 1987, pp. 264–267.
10. I. Pitas and A. N. Venetsanopoulos, *Nonlinear Digital Filters: Principles and Applications* (Kluwer, Dordrecht, 1990).
11. Y. Fong, C. A. Pomalaza-Raez, and X. Wang, Opt. Eng. **28**, 749 (1989).
12. V. V. Lukin, V. P. Melnik, A. B. Pogrebniak, *et al.*, J. Electron. Imaging **5**, 410 (1996).
13. F. R. Hampel, E. M. Ronchett, P. J. Roussew, *et al.*, *Robust Statistics. The Approach Based on Influence Function* (Wiley, New York, 1986).
14. T. P. Hettmansperger, *Statistical Inference Based on Ranks* (Wiley, New York, 1984).

Translated by V. Chechin

Doklady Physics, Vol. 45, No. 4, 2000, pp. 155–156. Translated from Doklady Akademii Nauk, Vol. 371, No. 6, 2000, pp. 761–762.

TECHNICAL PHYSICS

An Intense Source of Optical Emission from Electrodeless Low-Frequency Discharge in Vapors of Sulfur and Mercury

Corresponding Member of the RAS A. N. Didenko, I. M. Ulanov, M. R. Predtechenskiĭ, and K. N. Kolmakov

Received December 9, 1999

Gas-discharge light sources play a major role among a variety of lighting devices. As a rule, the maximum power of intense arc gas-discharge lamps with different filling is limited by the maximum admissible current, since corrosion of the electrode material strongly depends on the current density. At present, the most powerful xenon arc lamp has a wattage of 50 kW and a service life of about 500 h. Alternatives to electric arc lamps are electrodeless induction lamps. However, the complexity and high cost of power supply units, as well as difficulties associated with a low coupling factor for a load (plasma) and a generator, prevent wide usage of intense high-frequency and microwave induction lamps. These problems can be solved by using the low-frequency induction discharge of the transformer type [1, 2]. The use of magnetic circuit in this type of induction discharge makes it possible to both operate at lower frequencies (10–100 kHz) and increase the coupling factor between a load and a power supply unit.

The achievements of modern electronics allow us to produce intense, small-size, and inexpensive power-supply units operating in the low-frequency radiowave region (10 to 100 kHz). Recently, amorphous magnetic materials with an extremely low loss in high magnetic fields (up to 1 T) in the same frequency range have become available. Thus, it is possible to develop devices based on the low-frequency induction discharges of the transformer type, which are competitive with those based on the high-frequency and microwave discharges.

The absence of electrodes in the low-frequency induction discharge of the transformer type allows development of high power-capacity thermoelectric facilities with an "unlimited" service life. In the case of the employment of this discharge in a lighting fixtures, the induction-lamp service life is limited only by the service life of the lamp-bulb material and is as long as 10000 h or even longer.

In this study, we have investigated emissive properties of the transformer discharge in vapors of sulfur and mercury in order to develop powerful lighting devices (up to 50 kW and higher).

The experimental setup involved a power-supply unit, an induction lamp, and measuring devices. The schematic diagram of such a setup is shown in Fig. 1. As a power-supply unit, we used either a PPCh standard generator (250 kW, 25 kHz) or a pilot module of a transistor power-supply unit (30 kW, 25 kHz) developed at the Institute of Nuclear Physics, Siberian Division, Russian Academy of Sciences. The induction lamp consisted of magnetic circuit (*1*) with a system of primary windings (*2*) and a quartz discharge chamber (*3*). The magnetic circuit was composed of four separate rings made of 3425 cold-rolled sheet trans-

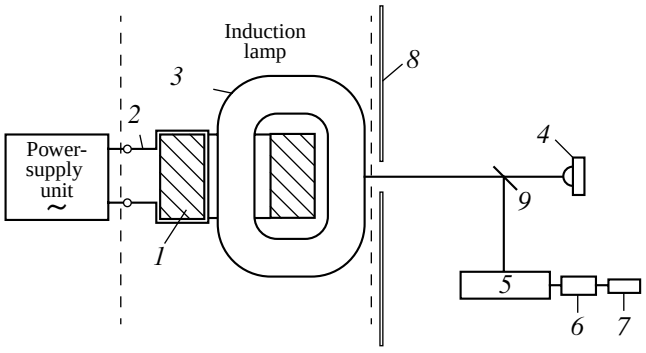

Fig. 1. Schematic diagram of the experimental setup for testing optical characteristics of low-frequency induction discharge in vapors of sulfur and mercury: (*1*) transformer magnetic circuit; (*2*) transformer primary windings; (*3*) quartz discharge chamber; (*4*) luxmeter; (*5*) monochromator; (*6*) PMT; (**7**) recorder; (*8*) screen; and (*9*) turning mirror.

Institute of Thermal Physics, Siberian Division, Russian Academy of Sciences, pr. Akademika Lavrent'eva 1, Novosibirsk, 630090, Russia
E-mail: konst@itp.nsc.ru; predtech@itp.nsc.ru

1028-3358/00/4504-0155$20.00 © 2000 MAIK "Nauka/Interperiodica"

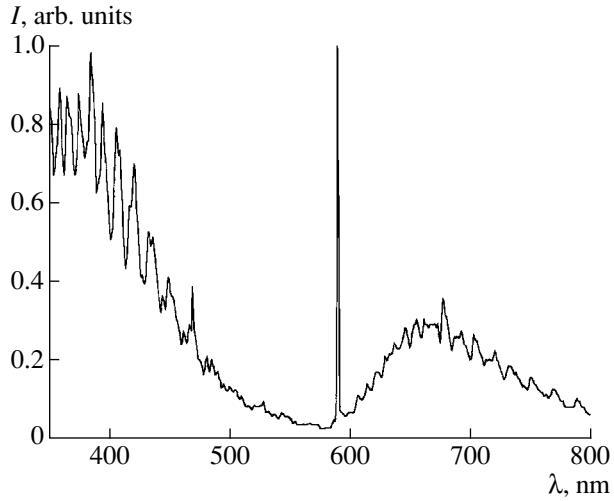

Fig. 2. Spectral distribution for the light emission of a discharge in sulfur vapors (P_{Ar} = 115 Pa and P_S = 50 Pa).

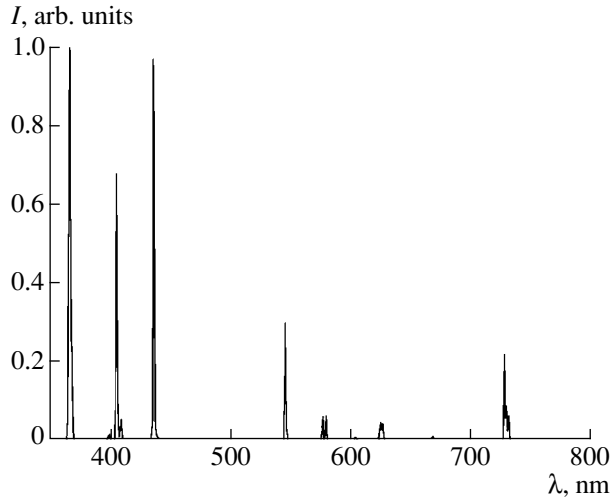

Fig. 3. Spectral distribution for the light emission of a discharge in mercury vapors ($P_{Hg} \approx 10^4$ Pa and P_{Ar} = 200 Pa).

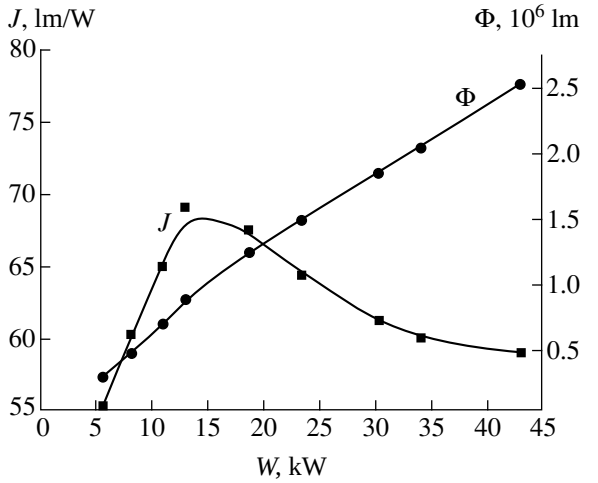

Fig. 4. Integrated light flux Φ and light efficiency J for a discharge in mercury vapors as a function of the total discharge power.

former steel. The magnetic-circuit total cross section was $S \approx 300$ cm^2. The quartz discharge chamber had the shape of a closed torus with the cross-section diameter of 80 mm. The perimeter of the discharge chamber midline was ~1.8 m.

Figure 2 shows the spectral distribution for the radiation emitted in the visible region by the low-pressure discharge in sulfur vapor (P_{Ar} = 115 Pa, P_S = 50 Pa). Our experiments have demonstrated that the low-pressure discharge with a partial sulfur pressure of 2 to 50 Pa has the low energy efficiency (light efficiency $J \sim 4$ lm/W), but a "good" spectral distribution in the blue and red frequency regions of the emissive spectrum.

Figure 3 shows the spectral distribution in the visible region for the discharge in mercury vapors ($P_{Hg} \sim 10^4$ Pa). Figure 4 shows the light efficiency and total-light flux for the discharge in mercury vapors as a function of the power consumed. It is seen that the mercury low-frequency induction discharge of the transformer type with a moderate pressure (~10^4 Pa) produces the integral light flux attaining 2.5×10^6 lm for the total discharge power of ~43 kW. This exceeds the efficiency characteristic of the best mercury arc lamps and the best high-pressure and superhigh-pressure xenon lamps (see, e.g., [3]).

Thus, the possibility of developing high-intensity gas-discharge light sources based on the low-frequency induction discharge of the transformer type has been shown experimentally. The advantages of this light source compared to arc lamps, as well as high-frequency and microwave lamps, are, respectively, the absence of disadvantages associated with the electrode service life and simplicity and low cost of the power supply unit and the lamp itself. The large extent of the luminous area and the high total light flux attained make it possible to apply this device even today in UV-drying technology and in other fields of industry in which intense UV-light fluxes are required.

REFERENCES

1. V. A. Kogan and I. M. Ulanov, Teplofiz. Vys. Temp. **31**, 105 (1993).
2. I. M. Ulanov, N. A. Rubtsov, S. N. Soldatov, and A. S. Vasil'kovskaya, Teplofiz. Aéromekh. **4**, 93 (1997).
3. *Handbook for Lighting Fixtures*, Ed. by Yu. A. Aĭzenberg (Énergoatomizdat, Moscow, 1983).

Translated by V. Troitskiĭ

Doklady Physics, Vol. 45, No. 4, 2000, pp. 157–159. Translated from Doklady Akademii Nauk, Vol. 371, No. 6, 2000, pp. 763–765.

TECHNICAL PHYSICS

Special Features of Self-Propagating High-Temperature Synthesis in Two-Layer S/Fe Thin Films and Metal–Dielectric Transitions in Iron Monosulfide

V. G. Myagkov, L. E. Bykova, V. S. Zhigalov, A. I. Pol'skiĭ, and G. N. Bondarenko

Presented by Academician V.V. Osiko September 17, 1999

Received June 18, 1999

Nowadays, self-propagating high-temperature synthesis (SHS) in thin two-layer films has only begun to be investigated [1, 2]. This process is characterized by three principal parameters: (1) an initiation temperature T_0 above which the SHS arises spontaneously; (2) self-maintained nature of the SHS front propagation, this front being observed visually; and (3) variation of sample resistance (up to two orders of magnitude) following the passage of the SHS front. The substantial distinction of the SHS in thin films from the SHS in powders consists in the fact that there exist two types of the former process. The first of them is similar to the SHS in powders in which new equilibrium phases are formed among reaction products. The metastable and amorphous phases were also discovered among them [1, 2]. The second type is characterized by the fact that, after the passage of the SHS front along the sample and a decrease in the substrate temperature T_s below the initiation temperature T_0 ($T_s < T_0$), the second front arises on the film surface. This front moves in the direction opposite to that of the SHS front. For eutectic systems, initial reagents are formed in products of the second-type reaction, therefore, the SHS can be initiated repeatedly. This new phenomenon was called the multiple SHS (MSHS) and represents a reversible structural phase transition [3, 4]. Hypothetically, the mechanism of the MSHS is specified by mechanisms of phase stratification arising in the case of eutectic solidification, as well as eutectoid and spinodal decomposition [3, 4]. In [4], it was shown that the resistance of the second-type samples varies virtually reversibly after the MSHS front has passed. It is known that the metal–dielectric transition [5, 6] is also characterized by a critical temperature T_c at which the jump and the change in conductivity take place. The self-maintained motion of the metal–dielectric-transition front exists in VO_2 film samples [5]. This fact presumes that the MSHS is similar to the metal–dielectric phase transition.

This study is devoted to investigation of the SHS in S/Fe two-layer film systems. The result of this investigation is the conclusion that the MSHS in S/Fe two-layer films and the metal–dielectric transition in iron monosulfide coincide.

S/Fe two-layer film samples were obtained by the consequent vacuum deposition of an iron layer (20–50 nm thick) and a sulfur layer (40–100 nm thick) on glass and mica substrates. The ratio between the thicknesses of iron and sulfur were taken to be ~ 1 : 2.2, which is close to the atomic ratio 1 : 1. A conversion degree η was determined by the variation of the magnetic moment of the iron layer and is described in studies [1, 2]. The SHS in S/Fe thin films was initiated by two methods. In the first case, a sulfur layer was deposited on the iron film at various substrate temperatures T_s. In Fig. 1 (curve *a*), we present the conversion degree η for the S(110 nm)/Fe(50 nm) sample as a function of a substrate temperature T_s. From this dependence, it follows that the formation of the chemical compound of iron and sulfur takes place at substrate temperatures close to T_s = 420 K. In this case, the S/Fe two-layer films were heated to the temperature T_s > 420 K. An essential distinction of the reaction in the S/Fe films from that in the samples, in which the SHS takes place, is an impossibility to visually observe the front motion. This can be associated with the fact that the reaction between sulfur and iron involves small sample depths, as a result of which the front motion is difficult to observe. An alternative explanation is that the SHS kinetics in these samples is not of the wave nature, and the reaction propagates perpendicularly to the film surface. Therefore, the SHS cycle consists in the following procedures: samples are heated with a rate of ~20 K/s, hold for 15 s, and cooled with a rate of ~10 K/s. This time is sufficient for passage of the SHS front including the time of induction. The magnetic analysis shows

Kirenskiĭ Institute of Physics, Siberian Division, Russian Academy of Sciences, Akademgorodok, Krasnoyarsk, 660036 Russia

1028-3358/00/4504-0157$20.00

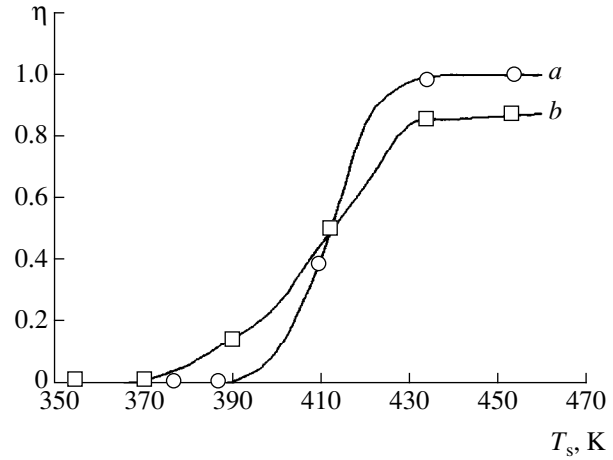

Fig. 1. Conversion degree η as a function of the substrate temperature T_s: (*a*) during depositing a sulfur layer (~110 nm thick) onto an iron film (~50 nm thick); (*b*) after heating a two-layer S(65 nm)/Fe(30 nm) film with a rate of ~20 K/s, holding for 15 s, and subsequent cooling with a rate of ~10 K/s (a MSHS cycle).

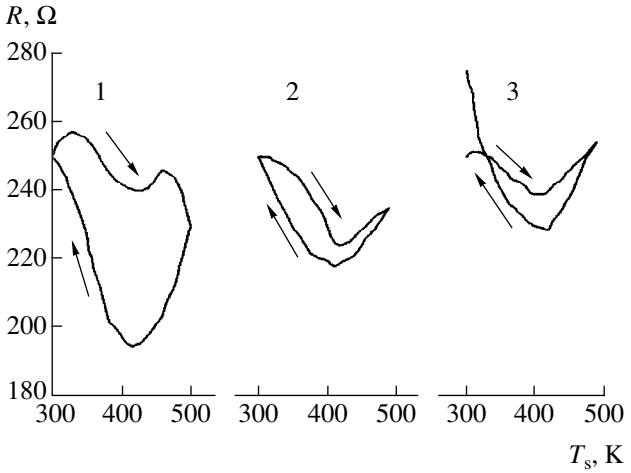

Fig. 2. Electrical resistance *R* of a two-layer film sample S(65 nm)/Fe(30 nm) as a function of a substrate temperature T_s for three subsequent MSHS cycles. Arrows show the direct and back variations of the resistance.

that, after the first cycle of heating, the iron layer 20–25 nm thick is involved in the reaction. The conversion degree η was not constant. It depended on the thickness of both iron and sulfur films, on the heating rate, and attained in the experiments the range of values η = 0.15 to 0.85. In Fig. 1 (curve *b*), we present the experimental dependence of the conversion degree η on a substrate temperature T_s for S(65 nm)/Fe(30 nm) samples. This dependence confirms also that the formation of the compound of iron and sulfur occurs at temperatures close to 420 K. The dependences $\eta(T_s)$ presented in Fig. 1 are typical for the SHS in thin two-layer films [1, 2]. Diffraction patterns taken from the samples, after the reaction between S and Fe has occurred, show the presence of residual iron, stoichiometric iron sulfide FeS, and also reflections, that were referred to a group of intermediate pyrrhotines. This group consists of the homologous series of Fe_nS_{n+1} having the FeS structure with a deficiency of iron [7, 8]. The curves $R(T_s)$ depend strongly on the conversion degree η. This dependence is presented in Fig. 2 for three first cycles of the SHS and η = 0.85. As is seen from Fig. 2, no jump-like variation of the electrical resistance takes place in the S/Fe samples during their heating as it was observed after the SHS front has passed [1, 2]. This is associated with the fact that the resistances of initial and reacted films are close. The direct and back variations of the $R(T_s)$ dependences for the electrical resistance on a substrate temperature T_s do not coincide. However, the type of the electrical conductivity changes from semimetallic to semiconductive with decreasing the substrate temperature in the neighborhood of T_s = 420 K. The similar dependences $R(T_s)$ for various SHS cycles and the coincidence between the initiation temperature and temperature corresponding to the change of the electrical-conductivity type (Fig. 2) confirm the fact that the MSHS phenomenon or its variety arise in the S/Fe film samples during cyclic heating with an initiation temperature T_0 = 420 K. It is well known [5, 6, 8] that, in massive FeS samples, the metal–dielectric phase transition with a critical temperature T_c = 420 K is observed. The structural mechanism of this transition is considered to be associated with a change in the crystal lattice. At a temperature $T > T_c$, FeS iron monosulfide has a perfect hexagonal lattice of the NiAs type. At temperatures $T < T_c$, iron atoms are grouped into triangular clusters in the basis plane forcing the sulfur atoms to displace along the *c*-axis [6–8]. The consequence of this fact is forming a superstructure with a doubled lattice parameter along the *c*-axis (2C superstructure). In such a superstructure, the electrical conductivity along the *c*-axis decreases by three orders of magnitude and varies only insignificantly in the basis plane [8]. The superstructures associated with ordering cation vacancies and having periods multiple to that of the FeS basis lattice are also formed in Fe_nS_{n+1} intermediate pyrrhotines ($n > 7$). For example, the Fe_7S_8 structure forms 4C, Fe_9S_{10}–5C, and $Fe_{11}S_{12}$–6C superstructures [7]. These long-period superstructures (modulated phases) arise in intermetallic [9], polytypic [10], and other chemical compounds. Nowadays, they represent an object of investigations [11]. As was said above, the mechanism of the MSHS is associated with phase-stratification mechanisms. It is well known [12] that, in the spinodal decomposition, modulated structures with a period of 10–500 nm arise. During the spinodal decomposition, there exist also nanometer-scale (nanoscale) modulated structures composed of alternating ordered and disordered phases [13, 14]. In this case, the processes of the phase stratification and ordering proceed simultaneously. The dynamics of developing such nanoscale modulated phases was considered

in [15]. This presumes a unique mechanism of phase stratification, ordering, and formation of modulated phases.

The coincidence between the initiation temperature T_0 for the MSHS in the S/Fe film samples having the critical temperature T_c and the metal–dielectric transition in FeS iron monosulfide ($T_0 = T_c = 420$ K), as well as close dependences $R(T_s)$ for various cycles of initiation and identical mechanisms of reversible structural transitions of the MSHS and the metal–dielectric transition make it possible to assume that these mechanisms coincide. On the basis of aforesaid, we can present the following mechanism for the MSHS in S/Fe two-layer films. With increasing the sample temperature, the interfacial boundary between iron and sulfur becomes unstable, and the process of intense diffusion proceeds perpendicularly to the interface up to a depth of 20–25 nm. As a result of this process, the synthesis of iron sulfides occurs. With decreasing temperature, the nanoscale stratification takes place at $T_s < T_0$: the iron and sulfur atoms displace within the lattice forming the nanoscale clusters (nanoclusters), whose ordered arrangement, in turn, forms superstructures. Since the reaction products represent primarily FeS iron monosulfide, this substance determines the initiation temperature $T_0 = 420$ K and temperature dependences $R(T_s)$. In the next cycles ($n > 2$) at $T_s > T_0$, the MSHS proceeds between the nanoclusters of iron and sulfur. At $T_s < T_0$, the phase stratification arises similarly to the first cycle. The actual picture is complicated by the process of afterburning, which can take place for $n > 2$ [2]. Strictly speaking, the MSHS in the S/Fe two-layer films occurs within the temperature interval $T_0 = 370$–430 K (Fig. 1). From the iron–sulfur state diagram [8], it follows that, in this temperature interval, not only structural transitions arise in FeS ($T_0 = 420$ K) but also in the intermediate pyrrhotines ($T_0 = 370$–420 K). On the basis of above statements and results of studies [1, 2, 4], we can assume that the SHS and the MSHS in two-layer film systems are initiated at temperatures corresponding to the minimum temperature of structural phase transitions on the phase diagram.

The only motivation of this study is a necessity to show that the structural phase transitions (the multiple self-propagating high-temperature synthesis and the metal–dielectric transition) can coincide. Among compounds for which the metal–dielectric transitions are observed in the form of the phase-transition wave, VO_2 vanadium dioxide [5] is present. The dependences for the front velocity on the substrate temperature during the metal–dielectric transition in VO_2 films and for the MSHS-front motion [3, 4] are also similar. Therefore, it should be expected that the metal–dielectric transition in VO_2 films is also determined by the MSHS reactions.

ACKNOWLEDGMENTS

This work was supported by the Russian Foundation for Basic Research, project no. 99-03-32184.

REFERENCES

1. V. G. Myagkov and L. E. Bykova, Dokl. Akad. Nauk **354**, 777 (1997).
2. V. G. Myagkov, V. S. Zhigalov, L. E. Bykova, and V. K. Mal'tseva, Zh. Tekh. Fiz. **68**, 58 (1998) [Tech. Phys. **43**, 1189 (1998)].
3. V. G. Myagkov, Dokl. Akad. Nauk **364**, 330 (1999) [Dokl. Phys. **44**, 45 (1999)].
4. V. G. Myagkov, L. E. Bykova, and G. N. Bondarenko, Zh. Éksp. Teor. Fiz. **115**, 1756 (1999) [JETP **88**, 963 (1999)].
5. A. A. Bugaev, B. P. Zakharchenya, and F. A. Chudnovskiĭ, *Metal-Semiconductor Phase Transition and Its Application* (Nauka, Leningrad, 1979).
6. G. V. Loseva, S. G. Ovchinnikov, and G. A. Petrakovskiĭ, *Metal–Dielectric Transition in Sulfides of 3d-Metals* (Nauka, Novosibirsk, 1983).
7. D. Vaughan and J. Craig, *Mineral Chemistry of Metal Sulfides* (Cambridge Univ. Press, Cambridge, 1978; Mir, Moscow, 1981).
8. D. N. Abishev and A. S. Pashinkin, *Magnetic Iron Sulfides* (Nauka, Alma-Ata, 1981).
9. C. S. Barret and T. B. Massalskiĭ, *Structure of Metals: Crystallographic Methods, Principles, and Data* (Pergamon, New York, 1980, 3rd ed.; Metalurgiya, Moscow, 1984), Part 1.
10. A. R. Verma and P. Krishna, *Polymorphism and Polytypism in Crystals* (Wiley, New York, 1966; Mir, Moscow, 1969).
11. P. Antony and D. Hariton, Phys. Rev. Lett. **78**, 270 (1997).

Translated by V. Bukhanov

Doklady Physics, Vol. 45, No. 4, 2000, pp. 160–163. Translated from Doklady Akademii Nauk, Vol. 371, No. 6, 2000, pp. 766–769.

TECHNICAL PHYSICS

Orientational Dependence of Mechanical Properties in Ni_3Al Single Crystals

Yu. I. Chumlyakov*, J. Wang, Corresponding Member of the RAS S. P. Efimenko***, I. V. Kireeva*, L. V. Brazhnikova*, N. S. Surikova*, and E. Yu. Panchenko***

Received October 14, 1999

The interest in the intermetallic Ni_3Al single crystals atomically ordered according to the $L1_2$-type is caused by the anomalous temperature dependence of critical-cleaving stresses τ_{cr}. These stresses increase with the test temperature up to $T = T_p$ [T_p is the peak temperature for the $\tau_{cr}(T)$ curve] and then abruptly decrease at $T > T_p$ [1]. Another feature of the mechanical behavior of Ni_3Al crystals lies in a strong orientational dependence of τ_{cr} and T_p within the range of the temperature anomaly. Asymmetry effects of τ_{cr} are also observed, i.e., dependence of critical-cleaving stresses for a fixed crystal orientation on the sign (tension or compression) of stresses applied [2, 3]. Theoretical approaches are developed [4] to explain these non-Schmid behavior of plasticity in Ni_3Al intermetallic compounds. These approaches are based on analysis of transverse slip processes of $a\langle 110\rangle$ screw superdislocations from the {111} octahedron planes to the {010} cube planes. Formation of the Kear–Wilsdorf dislocation barriers results in a blocking of gliding screw dislocations. The more intense transverse slipping dislocations from {111} to {010} planes occur, the larger resistance is undergone by the $a\langle 110\rangle\{111\}$ dislocations to their motion in the primary slip system. The tensor components of external applied stresses affect processes of transverse slipping in the primary slip system $[\bar{1}01]\{111\}$ and in the $\langle 110\rangle$ {010} system of transverse slipping. Components of the stress tensor also affect splitting the leading partial dislocation into the partial Shockley dislocations in the primary plane and in the plane of transverse slipping. Based on these facts, we can explain experimental data on the orientational dependence and asymmetry of τ_{cr} [1–5].

Up to now, systematic experimental data for binary Ni_3Al crystals of the stoichiometric composition, which are devoted to studies of the orientational dependence and asymmetry of τ_{cr} are absent in literature. This is associated with a difficulty of synthesizing large single crystals from which the samples for studying strain by tension could be prepared. Only one study is known [5], in which stoichiometric Ni_3Al single crystals were obtained, and their mechanical properties under compression deformation were studied. Systematic experiments under deformation by tension of Ni_3Al single crystals of the stoichiometric composition are necessary to understand their properties. First, it is important to explain how the deviation from the stoichiometry affects the orientational dependence of τ_{cr} and T_p. Second, by comparison of data on tension of crystals of different orientations with the results of the compression experiments [5], a possibility arises to study the asymmetry phenomenon. These experiments allow us to study the validity of the Boas–Schmid law for stoichiometric Ni_3Al single crystals. Another possibility for these crystals is the existence of the orientational dependence and asymmetry for τ_{cr}, as it is usually observed in nonstoichiometric binary Ni_3Al crystals and single crystals of ternary Ni_3AlMe alloys [1–3, 5].

The crystals under investigation were grown in magnesium oxide crucibles by the Bridgman method in the helium ambient. Furthermore, the crystals were homogenized at 1473 K for 24 h in the inert gas. The samples for tests by tension have the shape of a double-

Table 1. Schmid factors for tension in the $[\bar{1}01](111)$ primary slip system for Ni_3Al single crystals

Crystal orientation	Schmid factor
001	0.41
016	0.482
013	0.5
012	0.485
011	0.41

* *Siberian Physicotechnical Institute, Novo-Sobornaya pl. 1, Tomsk, 634050 Russia*

** *Institute of Metal Research, Chinese Academy of Sciences, 72 Wenhua Road, Shenxang, China*

*** *Baikov Institute of Metallurgy, Russian Academy of Sciences, Leninskiĭ pr. 49, Moscow, 117334 Russia*

1028-3358/00/4504-0160$20.00

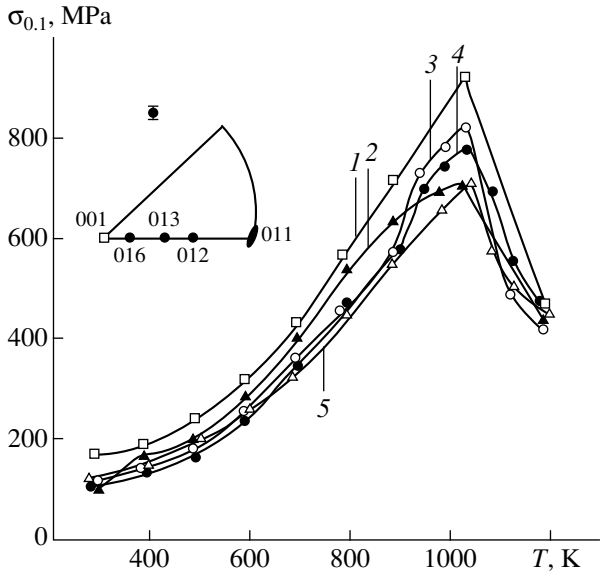

Fig. 1. Temperature dependence of the axial stresses $\sigma_{0.1}$ for stoichiometric Ni_3Al single crystals under tension. (*1*) [001] tension axis; (*2*) [011]; (*3*) [016]; (*4*) [013]; (*5*) [012].

blade with the working part $1 \times 3 \times 12$ mm in size. Orientation of the samples was determined by a diffractometer. The crystals were cut off by the electric-spark tool, and the damaged layer was removed by the mechanical polishing and chemical etching in the aqua regia (1 part of NHO_3 + 3 parts of HCl), and electrolytic lapping in the electrolyte (80 g of Cr_2O_3 + 210 ml of H_3PO_4) at the voltage $U = 22$ V for the time $t = 2$–3 min. The tests were carried out in vacuum of 1.3×10^{-3} MPa at the PRV setup. Experimental results were obtained by averaging over 3–5 samples.

The yield-stress $\sigma_{0.1}$ as a function of the test temperature $T = 300$–1173 K for tension of Ni_3Al crystals of different orientation is presented in Fig. 1. It is seen that for all the orientations studied, three regions can be isolated in the curves $\sigma_{0.1}(T)$: the first one ($T = 300$–373 K) is characterized by a weak dependence of $\sigma_{0.1}(T)$; in the second region ($373 \text{ K} < T < T_p = 1023$ K), an anomalous dependence of $\sigma_{0.1}(T)$ is observed at which the increase of deforming stresses occurs with increase in T; and, finally, at $T > T_p$ in the third region, the normal temperature dependence $\sigma_{0.1}(T)$ takes place.

The peak temperature T_p and critical-cleaving stresses τ_{cr} for the primary octahedral slip system $[\bar{1}01](111)$ (Fig. 2) weakly depend on the orientation (Fig. 1). The Schmid factors for the $[\bar{1}01](111)$ primary slip system are presented in Table 1. This behavior of T_p and $\tau_{cr}(T)$ (Figs. 1, 2) turns out to be untypical for ternary Ni_3AlTi crystals and binary crystals deviated from the stoichiometry [1–3, 5], in which a strong orientational dependence of T_p and τ_{cr} is also observed on the sign of applied (tension or compression) stresses. Maximum values of T_p and τ_{cr} are attained for the [001] orientation and a significant decrease in T_p, and τ_{cr} occurs when approaching to the [001] orientation at $T < T_p$ [1–3, 5].

Finally, one more important difference in mechanical behavior of stoichiometric Ni_3Al single crystals from the ternary Ni_3AlTi alloys (Al-enriched Ni_3Al crystals) [1–3, 5] is the absence of the asymmetry phenomenon: the values of τ_{cr} turn out to be independent of

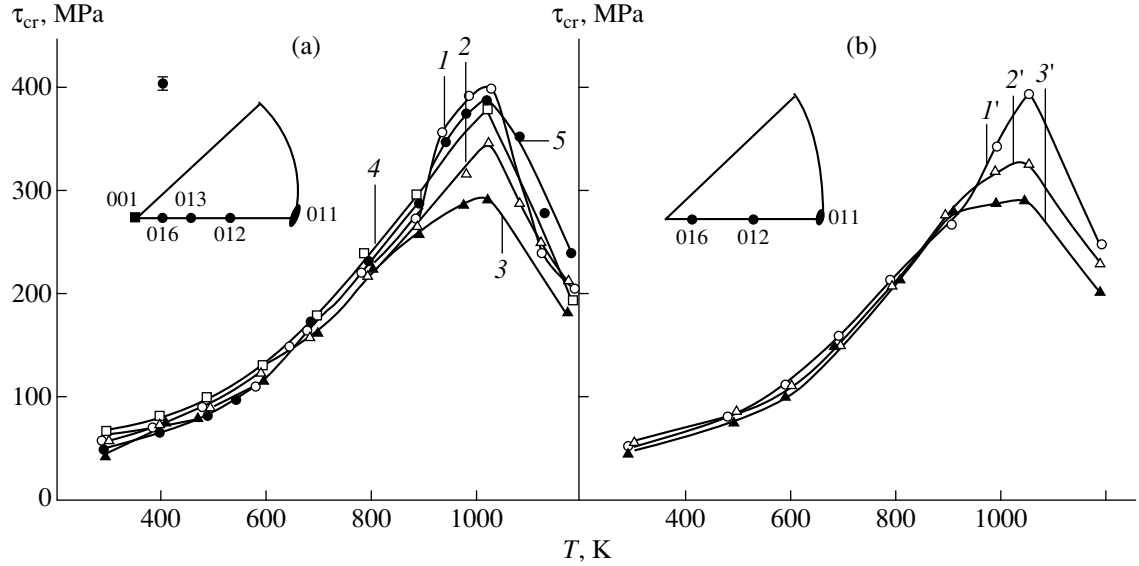

Fig. 2. Temperature dependence of critical-cleaving stresses τ_{cr} for stoichiometric Ni_3Al single crystals under (a) tension and (b) compression [5]; (*1*, *1*') [016] tension / compression axis; (*2*, *2*') [012] tension axis; (*3*, *3*') [011]; (*4*) [011]; (*5*) [013]. (*1*–*5*) tension; (*1*'–*3*') compression.

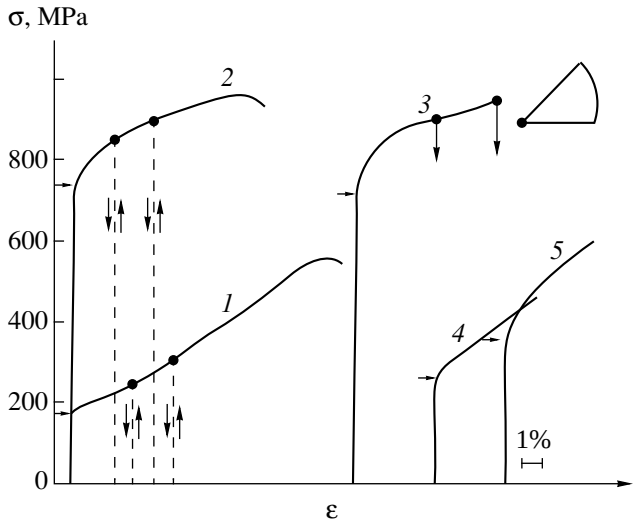

Fig. 3. Strain hardening curves for [001] Ni_3Al single crystals of the stoichiometric composition under tension. (*1*, *2*) one-stage deformation; (*3*–*5*) two-stage deformation. (*1*, *4*, and *5*) T_{def} = 300 K; (*2* and *3*) T_{def} = 873 K.

the deformation direction, i.e., tension or compression (Fig. 2). The data on compression deformation are taken for comparison from [5]. As is seen from Fig. 2, at the stage of the anomalous dependence of $\tau_{cr}(T)$, the values of τ_{cr} turn out to be close to each other under tension and compression. Consequently, in stoichiometric Ni_3Al single crystals, the Boas–Schmid law is valid under both tension deformation and compression deformation in contrast to nonstoichiometric binary and ternary Ni_3Al crystals [1–3, 5]. Thus, the results of this work show that, when developing a theory of anomalous temperature dependence for $\tau_{cr}(T)$ in $L1_2$-intermetallic compounds, we should take into account not only the action of the external-stress fields on the core structure of gliding $a\langle 110\rangle(111)$ screw dislocations [4], but also the change in the gliding dislocation structure caused by a deviation in the composition of the Ni_3Al intermetallic compound from the stoichiometry or when doping this compound with a third element.

Ni_3Al crystals preserve their strength after unloading and repeated loading at $T < T_p$ (Fig. 3, curves *1* and *2*). This fact implies that the dislocation structure formed turns out to be stable after the first loading and does not relax in the loading–unloading cycle [6, 7]. If a crystal deformed up to ε = 4% at T_1 = 873 K is unloaded and cooled down to T_2 = 300 K, the level of deforming stresses attained in the case of a high-temperature deformation does not preserve under repeated low-temperature deformation (Fig. 3, curves *3*–*5*).

We denote the strain, at which the deformation occurring at T_1 = 873 K is finished, as σ_f^I. We also denote the stress corresponding to the plastic-flow onset at the second low-temperature stage at T_2 as $\sigma_{0.1}^{II}$. Then $\sigma_f^I/\sigma_{0.1}^{II}$ = 3.5, and the macroscopic jump of stresses $\Delta = \sigma_f^I - \sigma_{0.1}^{II}$ = 460 MPa (Table 2 and Fig. 3).

It is seen from Fig. 3 and Table 2 that the dislocation "frame" arising in [001] crystals of multiple orientations, does not resist the dislocation motion in the case of the low-temperature deformation. This conclusion follows from the comparison of the yield stress for crystals deformed according to the two-stage scheme at T_1 = 873 K up to ε = 4%, and then at T_2 = 300 K, and the yield stress of crystals deformed only at T_2 = 300 K (Table 2, Fig. 3, curves *3*–*5*). Dislocations introduced into a crystal at high-temperature T_1 increase the strain-hardening coefficient Θ, which rises with growing ε at the temperature T_1 and higher in ⟨001⟩ crystals of the multiple orientation stronger than in ⟨012⟩ ones.

Such a feature of the macroscopic jump of stresses under the two-stage deformation is associated with the anomalous dependence of deforming stresses (Figs. 1, 2). The dislocations of the high-temperature "frame" turn out to be weakly interacting with fresh dislocations providing the plastic flow at the second low-temperature deformation stage.

Thus, we have studied, for the first time, the orientational dependence of critical-cleaving stresses in stoichiometric Ni_3Al single crystals under the deformation by tension. It is found within the temperature range of observation of anomalous dependence for $\tau_{cr}(T)$ that the Boas–Schmid law holds and the values of τ_{cr} turn out to be independent of the crystal orientation and the direction of deformation (tension or compression).

Table 2. Mechanical properties of Ni_3Al single crystals under tension

Orientation of the tension axis	Stage I					Stage II				
	T_{def}, K	$\sigma_{0.1}^I$, MPa	σ_f^I, MPa	ε^I, %	Θ^I, MPa	$\sigma_{0.1}^{II}$, MPa	ε^{II}, %	Θ^{II}, MPa	Δ, MPa	Δ, %
	873	540	670	4.0	3250	210	5.0	2800	460	69
[012]			710	10	1700	220	5.0	4600	490	69
[012]	300	120	490	34	1250					

Consequently, the non-Schmid effects observed previously in ternary Ni_3AlTi crystals and nonstoichiometric binary Ni_3Al crystals [1–3, 5] are a result of the action on the core structure of a screw $a\langle 110\rangle\{111\}$ dislocation related not only to the external-stress field, but also to the deviation from the stoichiometry and doping with a third element [1–5].

ACKNOWLEDGMENTS

This work was supported by the Russian Foundation for Basic Research, project no. 96-02-10048.

REFERENCES

1. S. M. Copleys and B. H. Kear, Trans. Metal. Soc. AIME **239**, 977 (1967).
2. F. E. Heredia and D. P. Pope, Acta Metal. Mater. **39**, 2027 (1991).
3. M. S. Kim, S. Hanada, S. Watanabe, and O. Izumi, Metal. Trans. A **21**, 107 (1990).
4. V. Paidar, D. P. Pope, and V. Vitek, Acta Metal. **32**, 435 (1984).
5. D. Golberg, M. Demura, and T. Hirano, Acta Mater. **46**, 2695 (1998).
6. N. D. Bakhteeva, B. A. Grinberg, A. V. Nemchenko, and Yu. N. Akshentsev, Fiz. Met. Metalloved. **85** (4), 149 (1998).
7. B. A. Grinberg, M. A. Ivanov, T. O. Barabash, and A. G. Blokhin, Fiz. Met. Metalloved. **81** (4), 29 (1996).

Translated by T. Galkina

Doklady Physics, Vol. 45, No. 4, 2000, pp. 164–166. Translated from Doklady Akademii Nauk, Vol. 371, No. 4, 2000, pp. 473–475.

ENERGETICS

On a Necessity of Extending the Concept of Equivalence in Mathematical Models

Academician Ya. B. Danilevich* and Yu. P. Petrov**

Received March 10, 1999

In studying objects and systems, whose mathematical models are presented by sets of ordinary differential equations, equivalent transformations are widely used. According to the traditional definition of the equivalence, transformations are considered to be equivalent if all solutions of a transformed system coincide with those of the initial one. The theory of equivalent transformations is well developed.

However, in a number of practical problems of power engineering, the traditional classical definition of equivalence is inadequate and needs further extension. We call equivalent in the extended sense two sets of differential equations if all solutions to these sets coincide for calculated values of parameters, and, in addition, under small variations of parameters, the solutions to the transformed set differ a little from the solutions to the initial set on the entire interval $0 \le t < \infty$.

This new definition, i.e., the equivalence in the extended sense, is necessary, e.g., for investigating the maintenance of the stability under small variations (unavoidable in actual practice) of parameters for control systems in energy-producing facilities. Generally, combinations of differential equations of various orders are primary and physically meaningful mathematical models for both a controlled object and a feedback-realizing device (controller). Such systems, being inconvenient for straightforward investigating, are transformed almost without exception into the standard Cauchy form by employing equivalent (in the classical sense) transformations. If all the solutions to the transformed closed system asymptotically approach zero with time lapse, and this feature is preserved under variation of parameters, the conclusion is drawn that the control system under investigation is stable and maintains stability under variations of its parameters [1, 2]. However, if the transformations of the equations for the system are equivalent in the classical sense but not in the extended one, such conclusion will be wrong, and this may be a source of accident for a system being designed.

We present an example of transformations that are equivalent in the classical sense but are not equivalent in the extended sense.

We consider a control system, whose mathematical model is represented by the following set of equations:

$$[mD^3 + (2+2m)D^2 + (4+m)D + 2]x = (D^2 + 2D + 1)u, \quad (1)$$

$$(D^2 + 4D + 5)x = (D+1)u. \quad (2)$$

Here, $D = \frac{d}{dt}$. Equations (1) and (2) describe a controlled object and a device in the feedback circuit, respectively, x is a regulated variable, u is the controlling action, and m is the parameter, whose calculated value is equal to unity. We transform equation (1) into the Cauchy form for the calculated value $m = 1$. Performing the well-known transformations, we obtain

$$\dot{x}_1 = -2x_1 + x_2 + u,$$
$$\dot{x}_2 = x_3, \quad (3)$$
$$\dot{x}_3 = -x_2 - 2x_3,$$

where the new variables x_1, x_2, x_3, and u are related to the original ones x, u by the equations

$$x_1 = x; \quad x_2 = \dot{x}_1 + 2x_1 - u; \quad x_3 = \dot{x}_2, \quad u = u. \quad (4)$$

Substituting (4) into (2), we obtain the equation for the feedback circuit expressed in terms of the new variables:

$$u = -x_1 - 2x_2 - x_3. \quad (5)$$

Substituting (5) into (3), we obtain the following equations for a closed system:

$$\dot{x}_1 = -3x_1 - x_2 - x_3,$$
$$\dot{x}_2 = x_3, \quad (6)$$

* *Department of Electric-Power Problems, Russian Academy of Sciences, Dvortsovaya nab. 18, St. Petersburg, 191186 Russia*

** *St. Petersburg State University, Universitetskaya nab. 7/9, St. Petersburg, 199164 Russia*

1028-3358/00/4504-0164$20.00

$$\dot{x}_3 = -x_2 - 2x_3.$$

The characteristic polynomial for set (6)

$$\lambda^3 + 5\lambda^2 + 7\lambda + 3 \quad (7)$$

has the roots $\lambda_1 = -3$ and $\lambda_2 = \lambda_3 = -1$. Therefore, all solutions to equations (6) are of the form

$$x_i = c_1 e^{-3t} + (c_2 t + c_3) e^{-t} \quad (8)$$

and are asymptotically attenuating as t increases.

For $m = 1$, the straightforward substituting (2) into (1) yields the equation for the closed system, which has the form

$$(D^3 + 5D^2 + 7D + 3)x = 0. \quad (9)$$

Taking into account (4), we obtain from (9) that the solution $x = x_1$ conserves the form of (3).

Thus, for the calculated value of the parameter $m = 1$, all the solutions to initial system (1), (2) coincide with the solutions to transformed system (6). This should be expected since the transformations used are equivalent in the classical sense. Are they also equivalent in the extended sense?

To study this point, we transform equation (1) into the Cauchy form for $m \neq 1$; i.e., we assume that the parameters of the object deviate from the calculated values. As a result, we obtain

$$\dot{x}_1 = -\frac{2}{m}x_1 + \frac{1}{m}x_2 + \frac{1}{m}u,$$

$$\dot{x}_2 = x_3, \quad (10)$$

$$\dot{x}_3 = -x_2 - 2x_3.$$

Next, we substitute the value of u from equation (5) into (10). In doing so, we assume that the parameters of the feedback-circuit device (controller) remain unchanged. Since the parameters of the controlled object and the controller can be independent (either totally or partially) of one another, such an assumption may well satisfy the actual situation.

We find the following equations for the closed system:

$$\dot{x}_1 = -\frac{3}{m}x_1 - \frac{1}{m}x_2 - \frac{1}{m}x_3,$$

$$\dot{x}_2 = x_3, \quad (11)$$

$$\dot{x}_3 = -x_2 - 2x_3$$

with the characteristic polynomial

$$\lambda^3 + \left(2 + \frac{3}{m}\right)\lambda^2 + \left(1 + \frac{6}{m}\right)\lambda + 3\frac{1}{m}.$$

It follows from this expression that the solutions to system (10) are very close to the solutions to system (8) for the values of m differing little from $m = 1$. Moreover, for all $0 < m < \infty$, the solutions remain tending to zero as $t \longrightarrow \infty$.

Thus, based on studying transformations of system (11), we should conclude that the control system under study would be stable and would maintain stability for both small and large (within the range $0 < m < \infty$) deviations of the parameter m from the calculated value $m = 1$.

However, the straightforward substitution of the value u from (2) into (1) yields the following equation for the closed system:

$$\{[(1-m)D^2 + (2-m)D + 3](D+1)^2\}x = 0. \quad (12)$$

For $m = 1$, its solutions, as should be expected, coincide with the solutions to system (11) for $m = 1$ (i.e., the direct evidence of the equivalence in the classical sense is available). However, for $m > 1$, the difference between solutions to systems (11) and (12) increases indefinitely with t, since solution to equation (12) for $m > 1$ (but not for $m < 1$) includes a term increasing indefinitely with time. Transformations that changed equations (1), (2) into equation (11) are not equivalent in the extended sense (although they are equivalent in the classical sense).

While studying equation (11), we can arrive at the erroneous conclusion that the stability of the closed system being studied is maintained under small variations of parameters. Erroneous conclusions of this kind are rather dangerous, since systems realized on the basis of these conclusions can lose their stability under small variations of parameters, the variations being necessarily of definite sign. Such systems can withstand the most severe tests and function properly for an indefinite period of time. Furthermore, under small drift of parameters, which is unavoidable in actual practice, these systems can suddenly lose their stability and terminate in an accident [3]. Certainly, errors can be easily avoided for moderate-order systems like those of (1), (2). However, when calculating modern control systems of high orders, even employing efficient and perfect methods (for example, proposed in [1, 2]) may cause an error if the difference between equivalence in the classic and extended sense is not taken into account.

To ensure against errors, it is desirable to develop a theory of transformations equivalent in the extended sense. For a particular case of linear control systems, methods of transformation were proposed and studied in [4], which exclude appearance of systems losing

their stability under small variations of parameters. For nonlinear systems, more complicated cases of stability loss are possible, which call for further profound investigation.

REFERENCES

1. V. T. Polyak and Ya. Z. Tsypkin, Avtom. Telemekh., No. 9, 45 (1990).
2. M. É. Braverman and L. I. Rozonoér, Avtom. Telemekh., No. 11, 17 (1991); No. 1, 41 (1992).
3. Yu. P. Petrov, Izv. Vyssh. Uchebn. Zaved., Élektromekh., No. 11, 106 (1991).
4. Yu. P. Petrov, *Synthesis of the Optimum Control System in the Case of Incompletely Known Perturbing Forces* (Leningr. Gos. Univ., Leningrad, 1987).
5. Yu. P. Petrov, *The Third Class of Physical and Technological Problems Intermediate between Well-Posed and Ill-Posed Ones* (St. Petersburg, 1998).

Translated by V. Tsarev

Doklady Physics, Vol. 45, No. 4, 2000, pp. 167–170. Translated from Doklady Akademii Nauk, Vol. 371, No. 4, 2000, pp. 476–479.

MECHANICS

An Estimate of the Entrainment of Dispersed Particles with Unknown Distributions by Liquid and Gas Flows on Evidence Derived from Solutions to the Equations of Motion

N. V. Sokolov

Presented by Academician O.M. Belotserkovskiĭ July 1, 1999

Received July 5, 1999

The problem of estimating the transport capacity of liquid and gas flows has been previously considered using various levels of source information, namely, for unknown distributions of dispersed particle in sizes and incomplete data on the probability of catching mass from that inherent in the initial particles [1–4]. However, a very important case when solutions to the equations of motion for a gaseous or liquid medium and dispersed particles immersed into it are available [5], with granulometric data on the composition being absent, still remains to be analyzed.

In this paper, we try to fill in this gap. Employing stochastic approaches in mechanics, we use the following expression [1–3]:

$$\varepsilon = \int_0^\infty P_-(r)dF(r). \tag{1}$$

Here, ε is the relative entrainment, i.e., the mass fraction of the dispersed particles entrained by a liquid or gas flow; $P_-(r)$ is the probability of entraining a mass from that inherent in a particle with the initial radius r; and $F(r)$ is the mass distribution function in sizes of the initial particles. $F(r)$ is the mathematical expectation of the mass fraction of the initial particles with their sizes less than r, which are caught by the fluid flow. We will treat $F(r)$ as an unknown function.

We then transform equation (1) using the integration by parts and taking into account that $F(0) = 0$ and $F(\infty) = 1$. As a result, equation (1) takes the form

$$\varepsilon = P_-(\infty) - \int_0^\infty F(r)dP_-(r). \tag{2}$$

In practical cases, $P_-(\infty) = 0$.

To estimate the value of $F(r)$, we use the inequality

$$\int_0^\infty r^{-n}dF(r) \geq \int_0^r \frac{dF(\xi)}{r^n} + \int_r^{r_{\max}} \frac{dF(\xi)}{r_{\max}^n}, \tag{3}$$

where ξ is the integration variable, $r_{\max}$ is the maximum size of the particles, which are brought into the fluid flow (if data determining $r_{\max}$ are absent, we set $r_{\max} = \infty$). Since

$$\int_0^r \frac{dF(\xi)}{r^n} + \int_r^{r_{\max}} \frac{dF(\xi)}{r_{\max}^n} = \frac{F(r)}{r^n} + \frac{1}{r_{\max}^n}[1 - F(r)], \tag{4}$$

it follows from expression (3) that

$$F(r) \leq \begin{cases} \dfrac{\overline{r^{-n}} - r_{\max}^{-n}}{r^{-n} - r_{\max}^{-n}}, & \text{if} \quad r < \dfrac{1}{\sqrt[n]{\overline{r^{-n}}}} \\ 1, & \text{if} \quad r \geq \dfrac{1}{\sqrt[n]{\overline{r^{-n}}}}. \end{cases} \tag{5}$$

Here, the notation $\overline{r^{-n}}$ stands for the integral $\int_0^\infty r^{-n}\,dF(r)$ that means, in the physical sense, a generalized characteristic of dispersity and can be directly found for $n = 1$, 2, and 3, even with unknown distribution functions of particles in sizes [1–4].

Then, using equality (2) and inequality (5) and taking into account that the function $P_-(r)$ could have local maxima and minima (that are associated with the influence of diffusion, adhesion, and crushing and aggrega-

Water Problems Institute,
Russian Academy of Sciences,
Novaya Basmannaya ul. 10, Moscow, 107078 Russia

1028-3358/00/4504-0167$20.00

tion of the particles in flows), we obtained the expression for the upper bound of the relative entrainment:

$$\varepsilon \le \int_0^{\frac{1}{\sqrt[n]{\overline{r^{-n}}}}} \frac{\overline{r^{-n}} - r_{\max}^{-n}}{r^{-n} - r_{\max}^{-n}} \Theta\left(\operatorname{sgn}\left(\frac{dP_-(r)}{dr}\right)\right) dP_-(r) + \int_{\frac{1}{\sqrt[n]{\overline{r^{-n}}}}}^{\infty} \Theta\left(\operatorname{sgn}\left(\frac{dP_-(r)}{dr}\right)\right) dP_-(r). \quad (6)$$

Here, $\Theta\left[\operatorname{sgn}\left(\frac{dP_-(r)}{dr}\right)\right]$ is the step function of the sign of the derivative of $P_-(r)$: $\Theta(+) = 0$ and $\Theta(-) = -1$. The function $\Theta\left[\operatorname{sgn}\left(\frac{dP_-(r)}{dr}\right)\right]$ can be written in the following form:

$$\Theta\left[\operatorname{sgn}\left(\frac{dP_-(r)}{dr}\right)\right] = \frac{1}{2}\left[\frac{dP_-(r)}{dr} - \left|\frac{dP_-(r)}{dr}\right|\right] \Big/ \left|\frac{dP_-(r)}{dr}\right|,$$

if $\frac{dP_-(r)}{dr} \neq 0$.

Relation (6) is appropriate in the case when there exist solutions to the equations of motion for a gaseous or liquid medium and dispersed particles immersed into it, with granulometric data on the composition being absent.

Expression (6) can be rewritten in the form

$$\varepsilon \le (\overline{r^{-n}} - r_{\max}^{-n}) \sum_{i=1}^{k} \left| \int_{a_i}^{b_i} \frac{dP_-(r)}{r^{-n} - r_{\max}^{-n}} \right| + \sum_{i=k+1}^{k+l} [P_-(a_i) - P_-(b_i)], \quad (7)$$

or by repeatedly integrating by parts

$$\varepsilon \le (\overline{r^{-n}} - r_{\max}^{-n}) \sum_{i=1}^{k} \left[\frac{P_-(a_i)}{a_i^{-n} - r_{\max}^{-n}} - \frac{P_-(b_i)}{b_i^{-n} - r_{\max}^{-n}} + n \int_{a_i}^{b_i} \frac{r^{-(n+1)} P_-(r)}{(r^{-n} - r_{\max}^{-n})^2} dr \right] + \sum_{i=k+1}^{k+l} [P_-(a_i) - P_-(b_i)].$$

Here, a_i and b_i are the initial and terminal points, respectively, of the ith section, on which the probability $P_-(r)$ decreases on the interval $[0, \sqrt[n]{\overline{r^{-n}}}]$ for $i \le k$ or on the segment $[\sqrt[n]{\overline{r^{-n}}}, \infty]$ for $i > k$;

$$a_1 < b_1 < a_2 < b_2 < \ldots < a_i < b_i < \ldots < a_{k-1} < b_{k-1} < a_k < b_k \le \sqrt[n]{\overline{r^{-n}}} \le a_{k+1} < b_{k+1} < \ldots < a_l < b_l \le \infty,$$

k and l are the numbers of the sections, on which the probability $P_-(r)$ decreases on the intervals $[0, \sqrt[n]{\overline{r^{-n}}}]$ and $[\sqrt[n]{\overline{r^{-n}}}, \infty]$, respectively.

If the derivative of this probability is negative at all radii (i.e., the probability of the mass entrainment decreases monotonically with increasing the particle size) and data determining $r_{\max}$ are absent, inequality (6) takes the simpler form:

$$\varepsilon \le -\overline{r^{-n}} \int_0^{\frac{1}{\sqrt[n]{\overline{r^{-n}}}}} r^n dP_-(r) + P_-\left(\frac{1}{\sqrt[n]{\overline{r^{-n}}}}\right). \quad (8)$$

It is worth noting that, after integrating by parts once again, relation (8) can be rewritten in a more compact form:

$$\varepsilon \le n\overline{r^{-n}} \int_0^{\frac{1}{\sqrt[n]{\overline{r^{-n}}}}} r^{n-1} P_-(r) dr. \quad (9)$$

To use practical inequalities (6)–(9), we must evaluate the function $P_-(r)$ by solving the equations of motion for dispersed particles in flows. For example, if spherical particles precipitate according to the Stokes law in a laminar flow inside a rectangular slit channel and the particle content is less than 0.5% of the volume, we can write out the equations

$$\frac{4}{3}\pi(\rho_1 - \rho_0) r^3 g - 6\pi\eta r \dot{x} = \frac{4}{3}\pi\rho_1 r^3 \ddot{x}, \quad 6\pi\eta r[u(x) - \dot{y}] = \frac{4}{3}\pi\rho_1 r^3 \ddot{y}. \quad (10)$$

Here, x and y are the Cartesian coordinates along which the precipitation of the dispersed particles and the fluid flow occur, respectively; $u(x)$ is the fluid velocity profile in the rectangular channel; g is the gravitational acceleration; r is the radius of the dispersed particles; ρ_0 and ρ_1 are the densities of the fluid and the particles in the flow, respectively; η is the fluid viscosity; and t is the elapsed time from the instant of the particle injection into the flow.

Assuming zero initial velocity of the particle precipitation, the solution to set of equations (10) can be written out in the following form:

$$y = \int_0^t e^{-\frac{\tau_2}{Kr^2}}\left[\frac{1}{Kr^2}\int_0^{\tau_2} e^{\frac{\tau_1}{Kr^2}} u[\varphi(\tau_1, h_0)]d\tau_1 + A_1\right]d\tau_2, \quad (11)$$

$$x = \varphi(t, h_0) = ar^2 t - ba^2 r^4\left[1 - e^{-\frac{t}{Kr^2}}\right] + h_0. \quad (12)$$

Here,

$$\varphi(\tau_1, h_0) = ar^2\tau_1 - ba^2 r^4\left[1 - e^{-\frac{\tau_1}{Kr^2}}\right] + h_0;$$

$$a = \frac{2g(\rho_1 - \rho_0)}{9\eta}; \quad b = \frac{\rho_1}{(\rho_1 - \rho_0)g}, \quad K = \frac{2\rho_1}{9\eta};$$

h_0 is the initial distance of a particle to the origin (in the case of the uniform distribution of particles in height, h_0 is the uniformly distributed random variable; A_1 is an integration constant determined from the value of the velocity component along the y-axis at the instant of the particle injection in the flow region under consideration; and τ_1 and τ_2 are the time integration variables.

It follows from (11) and (12) that

$$L = \int_0^{t_*} e^{-\frac{\tau_2}{Kr^2}}\left[\frac{1}{Kr^2}\int_0^{\tau_2} e^{\frac{\tau_1}{Kr^2}} u[\varphi(\tau_1, h^*(r))]d\tau_1 + A_1\right]d\tau_2, \quad (13)$$

$$h^*(r) = \begin{cases} H - ar^2 t_* + ba^2 r^4\left[1 - e^{-\frac{t_*}{Kr^2}}\right], \\ \text{if } H - ar^2 t_* + ba^2 r^4\left[1 - e^{-\frac{t_*}{bar^2}}\right] \geq 0 \\ 0, \text{ if } H - ar^2 t_* + ba^2 r^4\left[1 - e^{-\frac{t_*}{bar^2}}\right] < 0. \end{cases} \quad (14)$$

Here, H is the flow depth; $h^*(r)$ is the coordinate of the initial level from which a particle manages to attain the bottom in the residence time of the particle inside a fixed region of the flow; L is the length of this fixed region, in which the dispersed particles are caught; and t_* is an auxiliary parameter determined from equation (13) for $h^*(r) > 0$.

For a given minimum value of r, when carrying out the calculations, we assume $h^*(r)$ to be slightly less than H and then diminish its value by increasing the auxiliary parameter until equality (13) is satisfied. The quantity obtained is the desired value of $h^*(r)$.

Such calculations must be repeated for sequential values of particle sizes until $h^*(r)$ is of the order of zero.

Note that $h^*(r_2) = 0$ for any $r_2 \geq r_1$ provided that $h^*(r_1) = 0$. Because of this, for all large r, we set $h^*(r) = 0$.

Using the quantity $h^*(r)$ determined from the solution to equations (13) and (14), we find the function

$$P_-(r) = \int_0^{h^*(r)} d\Phi_\zeta(x), \quad (15)$$

where $\Phi_\zeta(x)$ is the function of the initial distribution of particles in depth. In the case of the uniform distribution of particles in depth, equation (15) takes the form

$$P_-(r) = \frac{h^*(r)}{H}. \quad (16)$$

Provided that the applicability conditions for the Stokes law are satisfied and the particle precipitation occurs from a laminar flow of fluid with an approximate piston regime of motion, with the initial distribution of the particles in depth being uniform and the particle concentration being less than 0.5%, the probability $P_-(r)$ takes the form

$$P_-(r) = \begin{cases} 1 - (r/r_{s_0})^2, \text{ if } r < r_{s_0} \\ 0, \text{ if } r \geq r_{s_0}. \end{cases} \quad (17)$$

Here, r_{s_0} is the minimum radius (the size of separation) of the particles that are completely caught by the flow. Under these conditions, we find from inequality (9) that

$$\varepsilon \leq \begin{cases} 1 - \frac{n}{n+2}[r_{s_0}(\overline{r^{-n}})^{1/n}]^{-2}, \text{ if } r_{s_0} \geq \frac{1}{\sqrt[n]{\overline{r^{-n}}}} \\ \frac{2}{n+2}\overline{r^{-n}} r_{s_0}^n, \text{ if } r_{s_0} < \frac{1}{\sqrt[n]{\overline{r^{-n}}}}. \end{cases} \quad (18)$$

The relation obtained can also be used to estimate the relative entrainment of particles by the flows subjected to centrifugal forces.

It is interesting to note that, as it follows from inequality (18) for $n \longrightarrow \infty$, provided all particles injected into a fluid flow have the same size, equal or greater than the size of separation, the relative entrainment is zero, (as was to be expected from the definition of r_{s_0}).

To experimentally verify relation (18), we used the data, obtained in collaboration with L.E. Nezhyta, on catching dispersed kaolin particles in the centrifugal "Plava-E" separator with the capacity index Σ = 842 m^2. The particles in the flow had an unknown distribution, the specific surface S = 1164 m^2/kg, and the density of 2600 kg/m^3. The characteristics given

Experimental and calculated estimates of the relative entrainment

Q, 10^{-6} m^3/s	Relative entrainment, ‰	
	experimental	according to (18)
2.9	15	≤21.2
3.64	17	≤23.7
7.14	20	≤33.3
10	39	≤39.4

allowed us to find directly $\overline{r^{-1}} = S\rho_1/3$ [1–3]. The size of separation was evaluated from the well-known formula

$$r_{s_0} = \sqrt{\frac{9\eta Q}{2(\rho_1 - \rho_0)g\Sigma}},$$

where Q is the volume velocity of the flow in the centrifugal separator.

The results of our calculations and experiments are presented in the table and confirm the validity of proven inequality (18). At the same time, using solutions to the equations of motion for particles and fluid allows us to improve the accuracy of estimating the relative entrainment, with the domain of application being constricted.

More complex dependencies of the drag forces for particles can be similarly used to evaluate the function $P_-(r)$ entering into inequalities (6)–(9). In the equations of motion, we can also allow for effects associated with the Brownian motion, adhesion, turbulent diffusion, crushing and aggregation of particles in flows, and electromagnetic forces. In these more complex cases, the function $P_-(r)$ is determined from other formulas, but the method of estimating the entrainment by flows remains the same and inequalities (6)–(9) can be also used.

Thus, we have analyzed the case when solutions to the equations of motion for both a fluid and dispersed particles immersed into it are known, with granulometric data on the composition being absent. Using the solutions to the equations of motion, we have managed to estimate the entrainment of dispersed particles with unknown distributions by gas and liquid flows.

ACKNOWLEDGMENTS

The author is grateful to Academician G. G. Chernyĭ for discussing at his seminar the problems of estimating the transport capacity of gas and liquid flows for various input data that initiated this paper.

REFERENCES

1. N. V. Sokolov, Dokl. Akad. Nauk SSSR **287**, 177 (1986).
2. N. V. Sokolov, Dokl. Vses. Akad. S-kh. Nauk im. V. I. Lenina, No. 7, 31 (1989).
3. N. V. Sokolov, Dokl. Akad. Nauk **325**, 549 (1992).
4. N. V. Sokolov, Dokl. Akad. Nauk **337**, 60 (1994).
5. *Mechanics and Scientific-Technical Progress*, Ed. by L. I. Sedov, G. G. Chernyĭ, and G. A. Lyubimov (Nauka, Moscow, 1987), Vol. 2.

Translated by V. Chechin

Doklady Physics, Vol. 45, No. 4, 2000, pp. 171–174. Translated from Doklady Akademii Nauk, Vol. 371, No. 4, 2000, pp. 480–483.

MECHANICS

A New Family of Phase Patterns in Three-Dimensional Dynamics of a Solid Body Interacting with Matter

M. V. Shamolin

Presented by Academician A.Yu. Ishlinskiĭ May 20, 1999

Received July 22, 1999

1. Setting the problem. At the present time, solving the problem of motion of a solid body in a resisting matter completely depends on developing mathematical methods and possible model constraints inherent in the problem. For example, the well-known Kirchhoff problem of motion of a solid body in a perfect incompressible fluid, being quiescent at infinity and executing vortex-free motion [1], deals with only one aspect of the problem. This aspect is related to the problem of integrability of corresponding dynamic systems (in our case, with the existence of the complete set of analytic and meromorphic first integrals).

It is easy to note that the Kirchhoff problem is one of the first approximations to the description of the interaction between a body and a medium because, on introducing an arbitrarily small viscosity, the dynamic Kirchhoff systems cease to be conservative. Thus, asymptotic limiting sets appear in the phase space of resulting systems because they become dissipative "as a whole." Therefore, no complete set of even-continuous first integrals can be asserted [2].

In connection with this comment, we indicate another aspect of the problem, namely, the complete qualitative analysis of dynamic systems (the topology of phase-space splitting into trajectories). It is the aspect that is an object of the present analysis.

2. Initial conditions and choice of variables. We consider a problem of a three-dimensional motion of a dynamically symmetric solid body under the condition that the line of action of the force **S** applied to the body from the matter does not change its orientation with respect to the body, a part of the body surface having the shape of a flat disk. The matter flows around the disk [3] according to laws of a jet flow around a body [4, 5]. The force **S** is aligned with the normal to the disk and is a quadratic form of the velocity of the disk center. The gravity force acting on the body is assumed to be negligible compared to the resisting force of the matter.

Institute of Mechanics, Moscow State University, Michurinskiĭ pr. 1, Moscow, 117192 Russia

The choice of six dynamic phase variables v, α, β (i.e., spherical coordinates of the velocity vector for the disk center) and p, q, r (the components of the body absolute angular velocity in the coordinate system linked with the body) allows us to consider the six-order system of dynamic equations as independent. Moreover, because the resisting force admits a group of the body rotation about the axis of dynamic symmetry (which passes through the center of mass and the center of the disk), the longitudinal component of the angular velocity being conserved: $p = p_0 = \text{const}$ [3, 6].

3. Dynamic equations of motion. If (A, B, B) are the principal moments of inertia for the body, m and σ are its mass and the distance between the center of mass and the disk, respectively, $z_1 = q\cos\beta + r\sin\beta$, $z_2 = r\cos\beta - q\sin\beta$, $z_i = Z_i v$, $i = 1, 2$, $\alpha^{\cdot} = \alpha' v$, $\beta^{\cdot} = \beta' v$, $v^{\cdot} = v' v$, then, in the absence of the proper rotation ($p_0 = 0$), dynamic equations of motion take the form

$$v' = v\Psi(\alpha, Z_1, Z_2), \tag{1}$$

$$\alpha' = -Z_2 + \sigma(Z_1^2 + Z_2^2)\sin\alpha + \frac{\sigma}{B}F(\alpha)\cos\alpha + \frac{s(\alpha)}{m}\sin\alpha, \tag{2}$$

$$Z_2' = \frac{1}{B}F(\alpha) - Z_2\Psi(\alpha, Z_1, Z_2) - Z_1^2\cot\alpha, \tag{3}$$

$$Z_1' = -Z_1\Psi(\alpha, Z_1, Z_2) + Z_1 Z_2\cot\alpha, \tag{4}$$

$$\beta' = Z_1\cot\alpha.$$

Here, $\Psi(\alpha, Z_1, Z_2) = -\sigma(Z_1^2 + Z_2^2)\cos\alpha + \frac{\sigma}{B}F(\alpha)\sin\alpha - \frac{s(\alpha)}{m}\cos\alpha$, $F(\alpha)$, $s(\alpha)$ are the pair of dynamic functions. They are determined with the use of an experimental information about features of jet flows

1028-3358/00/4504-0171$20.00

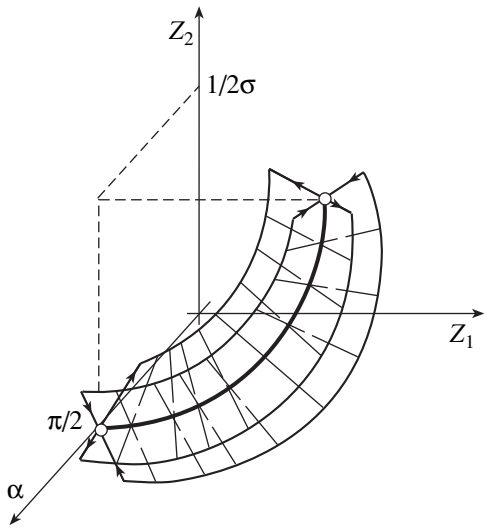

Fig. 1.

around bodies [7]. The typical representatives for the classes of functions $\{F\}$ and $\{s\}$ are the functions

$$F_0(\alpha) = A'B'\sin\alpha\cos\alpha,$$
$$s_0(\alpha) = B'\cos\alpha(A', B' > 0). \quad (5)$$

Equations (1)–(4) and (2)–(4) form closed subsystems of the fourth and third orders, respectively.

Under certain natural conditions, the set of equations (1)–(4) together with condition (5) reflects principal topological features for the division of the general set (1)–(4) into trajectories. In addition, vector fields of the general set (1)–(4) and also of equations (1)–(4) together with condition (5) are topologically equivalent.

4. System rest points. In the phase space of the set of equations (2)–(4), rest points can be projections of nonsingular phase trajectories in the fourth-order phase space of the set of equations (1)–(4). Indeed, the set of equations (1)–(4) has equilibrium positions filling in one-dimensional manifolds. Therefore, the problem of rest points is divided into two ones: for the set of equations (1)–(4) in the fourth-order phase space and for the shortened set of equations (2)–(4) in the phase space $\{(\alpha, Z_1, Z_2) \in \Re^3: 0 < \alpha < \pi, Z_1 > 0\}$.

The rest points of the set of equations (1)–(4) are given by the following relations including the parameter v_1:

$$\alpha = \frac{\pi}{2}, \quad \left(Z_2 - \frac{1}{2\sigma}\right)^2 + Z_1^2 = \frac{1}{4\sigma^2}, \quad v = v_1. \quad (6)$$

In the phase space of the set of equations (1)–(4), system (6) specifies a two-dimensional manifold (circular cylinder) completely filled with rest points.

The set of equations (2)–(4) has rest points in the space $\{(\alpha, Z_1, Z_2) \in \Re^3: 0 \le \alpha \le \pi, Z_1 \ge 0\}$, which are specified by the relations

$$\alpha = \pi k, k \in \{0, 1\}, Z_1 = Z_2 = 0, \quad (7)$$

$$\alpha = \frac{\pi}{2}, \quad \left(Z_2 - \frac{1}{2\sigma}\right)^2 + Z_1^2 = \frac{1}{4\sigma^2}. \quad (8)$$

System (8), and only it, specifies in the phase space rest points, to which manifolds of the rest points of the set of equations (1)–(4) are projected.

Due to the simplicity of the mechanical interpretation of steady motions corresponding to rest points (7), (8), we will call these points explicit equilibrium positions (EEP).

Definition 1. *We will call implicit equilibrium positions* (*IEP*) *the rest points of the set of equations* (2)–(4), *which do not lie in the planes*

$$\{(\alpha, Z_1, Z_2) \in \Re^3: Z_2\sin\alpha\cos\alpha = 0\}.$$

5. Implicit equilibrium positions. We introduce the notation $n_0^2 = \frac{F'(0)}{B}$. For simplicity, we consider the set of equations (2)–(4) combined with condition (5). The representation of the IEP by the system of equations

$$Z_2 = \frac{\sigma n_0^2}{2}\sin\alpha, \quad Z_1^2 = n_0^2\left[1 - \frac{\sigma^2 n_0^2}{4}\right]\sin^2\alpha,$$
$$\sigma n_0 < 2, \quad \cos\alpha = -\frac{\sigma n_0^2 m}{2s(0)}$$

is the necessary and sufficient condition for the existence of IEP (not laying in the integral plane $\{(\alpha, Z_1, Z_2) \in \Re^3: Z_1 = 0\}$, onto which the phase pattern of the corresponding system from the plane dynamics [7, 8] is mapped. At $\sigma n_0 > 2$, IEP "descend" onto the integral plane $\{(\alpha, Z_1, Z_2) \in \Re^3: Z_1 = 0\}$ [7, 8].

6. Classification of the rest points of the system and its symmetries. We now introduce two dimensionless parameters: $\mu_1 = 2\frac{s(0)}{mn_0}$ and $\mu_2 = \sigma n_0$.

Statement 1. (i) *Rest points filling in circumference* (8) *at* $Z_2 < \frac{1}{2\sigma}$ *are saddles in each area perpendicular to the circumference* (Fig. 1), *while at* $Z_2 > \frac{1}{2\sigma}$, *they are attracting*;

(ii) *At* $k = 0$, *the rest point* (7) *is repulsing.*

(iii) *At* $k = 1$, *the rest point* (7) *is repulsing or attracting if* $\mu_2 < \mu_1$ or $\mu_2 > \mu_1$, *respectively.*

The vector field of the set of equations (2)–(4) possesses the property of central symmetry with respect to

the points (πk, 0, 0), i.e., in the coordinates (α, Z_1, Z_2), this field changes its direction after the replacement

$$\begin{pmatrix} \pi k + \alpha \\ Z_1, Z_2 \end{pmatrix} \longrightarrow \begin{pmatrix} \pi k - \alpha \\ -Z_1, -Z_2 \end{pmatrix}, \quad k \in \{0, 1\}.$$

Moreover, the plane $\{(\alpha, Z_1, Z_2) \in \Re^3: Z_1 = 0\}$ is integral, and the vector field of the system possesses the following symmetry: α- and Z_2-components remain invariable, and the Z_1-component changes its sign after the replacement

$$\begin{pmatrix} \alpha \\ Z_1, Z_2 \end{pmatrix} \longrightarrow \begin{pmatrix} \alpha \\ -Z_1, Z_2 \end{pmatrix}, \quad k \in \{0, 1\}.$$

For the further analysis, we introduce definitions for the layer family $\Pi_{(\alpha_1, \alpha_2)} = \{(\alpha, Z_1, Z_2) \in \Re^3: \alpha_1 < \alpha < \alpha_2\}$, and in this case $\Pi_{\left(-\frac{\pi}{2}, \frac{\pi}{2}\right)} = \Pi$, $\Pi_{\left(\frac{\pi}{2}, \frac{3\pi}{2}\right)} = \Pi'$. Note, that, in fact, the layer $\Pi_{(0, \pi)}$ is the phase space of the set of equations (2)–(4).

7. Introducing into the phase-pattern classification. We will study those dynamic systems of the form (2)–(4), for which IEP exist only outside the plane $\{(\alpha, Z_1, Z_2) \in \Re^3: Z_1 = 0\}$. In the general space of physical parameters, only the domain

$$\left\{(\mu_1, \mu_2) \in \Re^2: \ \frac{s(\alpha)}{m\cos\alpha} \geq \frac{\sigma F(\alpha)}{B\sin\alpha}, \right.$$
$$\left. \forall \alpha \in \left(0, \frac{\pi}{2}\right), \sigma n_0 < 2 \right\} \tag{9}$$

will be, basically, investigated.

The typical topological classification of EEP was given above. For the complete classification of phase patterns, we present here a number of statements solving many urgent problems of a qualitative character.

Statement 2. *In the case of the set of equations* (2)–(4), *trajectories going to infinity exist and are unique. Their* α- *and* ω-*limiting sets are infinite points* $(+0, +\infty, +\infty)$ *outside the integral plane* $\{(\alpha, Z_1, Z_2) \in \Re^3: Z_1 = 0\}$ *and points* $(+0, 0, +\infty)$ *laying in it.*

Statement 3. *For systems of equations of the form* (2)–(4), *there exist no closed characteristics in the domain of parameters* (9).

The principal problem in the classification of (three-dimensional) phase patterns is that of the behavior of stable and unstable separatrices of existing (in our case, nonisolated and nonhyperbolic) saddles.

Statement 4. (I) *In the layer* Π', *stable separatrices for points* (8) *at* $Z_2 < \frac{1}{2\sigma}$ *have the origin of coordinates as* α-*limiting sets* (Fig. 2).

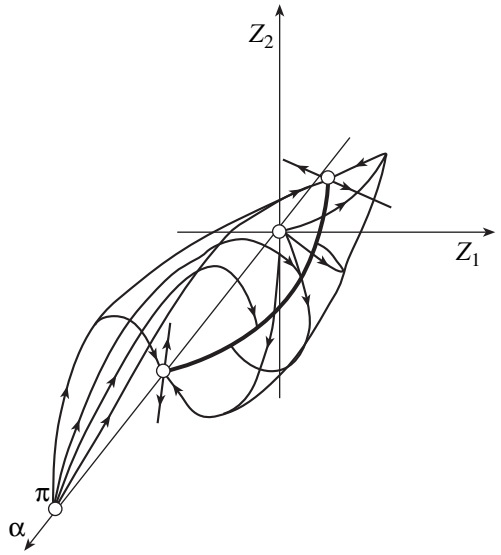

Fig. 2.

(II) *In the domain of parameters* (9), *separatrices, entering into points* (8) *at* $Z_2 < \frac{1}{2\sigma}$ *in the layer* Π', *have the point* $(\pi, 0, 0)$ *as an* α-*limiting set* (Fig. 2).

8. The principal classification theorem. We consider a problem of the behavior of separatrices emerging from points (8) at $Z_2 < \frac{1}{2\sigma}$. For this purpose, we define (by analogy with [7, 8]) the index of the separatrix property (ISP) for this system.

Definition 2. *By ISP* (*we will denote it as* isp), *we imply the number* $I \in N_0 \cup \left\{l + \frac{1}{4}, l \in N_0\right\}$. *By definition, if there exist separatrices emerging from points* (8) *at* $Z_2 < \frac{1}{2\sigma}$ *into the layer* Π *and having points* (8) *at* $Z_2 > \frac{1}{2\sigma}$ $(I \in N_0)$ *or the infinite point* $\left(I \in \left\{l + \frac{1}{4}, l \in N_0\right\}\right)$ *as the* ω-*limiting set, then* isp = *I. In this case, such separatrices envelop circumference* (8) *and go out l times into the domain* $\{(\alpha, Z_1, Z_2) \in \Re^3: Z_2 < 0\}$. *At the same time, there exist no such separatrices enveloping circumference* (8) *and going out* $l + 1$ *times into the domain* $\{(\alpha, Z_1, Z_2) \in \Re^3: Z_2 < 0\}$.

The classification theorem. *For an arbitrary* isp *from the domain of definition, there exists a point in the parameter space of the system of equations* (2)–(4), *for which, in accordance with Definition* 2, *the behavior of separatrices under consideration is realized in the system phase space.*

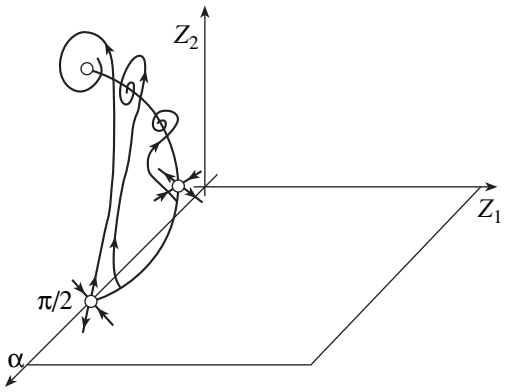

Fig. 3.

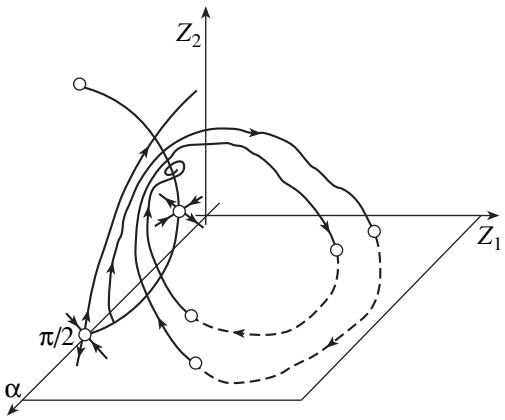

Fig. 4.

9. Classification of a certain set of three-dimensional phase patterns. By virtue of the principal theorem, we can perform a complete classification of phase patterns for the set of equations (2)–(4) when its parameters take values corresponding to domain (9). There exists an infinite number of such topologically nonequivalent patterns.

In order to perform the complete classification of the patterns, we should investigate separatrices going out from points (8) at $Z_2 < \frac{1}{2\sigma}$ into the layer Π'. Such separatrices can have limiting sets belonging to IEP. The equilibrium position (of IEP) in the half-space $\{(\alpha, Z_1, Z_2) \in \Re^3: Z_1 > 0\}$ is of a saddle type with one attracting proper direction and two repulsing ones. One stable branch (of the given IEP) has the point $(\pi, 0, 0)$ as an α-limiting set. The unstable directions, over which an entire plane is pulled, have attracting points (8) for $Z_2 > \frac{1}{2\sigma}$ and also an infinite point as limiting sets (see Statement 2).

Topological types of three-dimensional phase patterns are "coded" by the isp index. This index "is responsible" for separatrix surfaces far from IEP.

10. Examples for three-dimensional phase patterns. Certain fragments of phase patterns for the set of equations (2)–(4), which are, generally speaking, topologically nonequivalent, are shown in Figs. 3 and 4 (Fig. 3: isp = 0; Fig. 4: isp = 2).

REFERENCES

1. H. Lamb, in *Hydrodynamics*, 6th ed. (Cambridge University Press, Cambridge, 1932; Gostekhizdat, Moscow, 1947), p. 928.
2. M. V. Shamolin, Usp. Mat. Nauk **53**, 209 (1998).
3. M. V. Shamolin, Izv. Ross. Akad. Nauk, Mekh. Tverd. Tela, No. 2, 65 (1997).
4. S. A. Chaplygin, *Selected Papers* (Nauka, Moscow, 1976).
5. M. I. Gurevich, *Jet Theory for Ideal Fluid* (Nauka, Moscow, 1979).
6. M. V. Shamolin, Dokl. Akad. Nauk **364**, 627 (1999) [Dokl.–Phys. **44**, 110 (1999)].
7. M. V. Shamolin, Vestn. Mosk. Univ., Ser. 1: Mat., Mekh., No. 4, 57 (1996).
8. M. V. Shamolin, Dokl. Akad. Nauk **337**, 611 (1994) [Phys.–Dokl. **39**, 587 (1994)].

Translated by V. Devitsyn

Doklady Physics, Vol. 45, No. 4, 2000, pp. 175–178. Translated from Doklady Akademii Nauk, Vol. 371, No. 5, 2000, pp. 617–620.

MECHANICS

Elastic Characteristics of an Interfacial Layer Formed by Polymeric Matrix Composites

Academician I. F. Obraztsov, Yu. G. Yanovskiĭ, and V. E. Zgaevskiĭ

Received September 2, 1999

Polymeric materials used today represent, as a rule, heterogeneous systems with a large relative interfacial area. A polymeric layer formed at this area has a complex microstructure and the microscopic-scale mechanical characteristics of this layer differ from those far from the interface [1].

It was understood for long [2, 3] that allowance for features of the interfacial layer is important in describing macroscopic, rheological, and mechanical properties of heterogeneous polymeric materials. However, at that time, this urgent problem faced a fundamental difficulty, namely, the lack of direct quantitative data on the structure and properties of the interfacial layer.

Recently, an efficient tool of investigation called the numerical experiment, associated with the essential development of methods of molecular physics and appearance of a new generation of computers, became available. Such an experiment yields direct quantitative characteristics of macromolecule conformation occurring in specific interfacial layers [4, 5]. These data allow elastic properties of the interfacial layer to be calculated as functions of its molecular and structure parameters.

In this paper, we describe elastic properties of the interfacial layer consisting of macromolecules, whose one end is attached to a surface of a filling agent. Our description is based on the approach proposed in [6]. We also use data concerning conformation of macromolecules in the interfacial layer, which were obtained on the basis of the direct numerical experiment [5].

We consider a small element of the filling-agent surface to be plane and set a uniform distribution of "active" centers over it. In each of these centers, an initial segment of a macromolecule is rigidly fixed. The number of such centers per unit area is denoted as χ. The existence of the impermeable surface changes conformation of macromolecules attached to the surface compared to that of free (unfixed) macromolecules situated far from the surface. We assume that the other (free) ends of macromolecules belonging to the interfacial layer are attached to a three-dimensional polymer network having known mechanical characteristics. Figure 1 shows a scheme of this near-surface layer. The filling-agent surface includes the coordinate X_2- and X_3-axes. The X_1-axis is directed along the normal to the surface element. Dots on the surface represent sites of macromolecule-tail attachments. The dots also denote nodes of the polymer network and sites of its attachments to macromolecules belonging to the interfacial layer of the thickness h. Evidently, the scheme under consideration describes only approximately an actual physical medium, where, in our opinion, other types of the macromolecule attachment to the surface exist necessarily. Nevertheless, the scheme proposed can turn out to be useful for analysis of possible approaches to estimating features of mechanical characteristics of the interfacial layer.

We consider an effect of the surface as a certain force acting on each macromolecule and changing the conformation of a macromolecule attached to the surface. This force causes deformation of the macromolecule, the initial state being considered as the conformation of a free macromolecule. This representation makes it possible to use the classical dependence between the stress and elongation and to introduce a phenomenological coefficient (front factor) to take the surface effect into account. Within the scope of this rep-

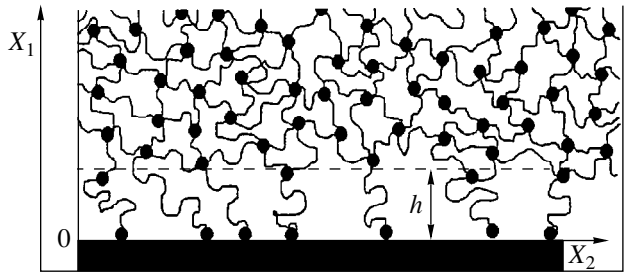

Fig. 1. Schematic diagram of the interfacial layer.

Institute of Applied Mechanics,
Russian Academy of Sciences,
Leninskiĭ pr. 32a, Moscow, 117334 Russia

1028-3358/00/4504-0175$20.00

resentation, the stress tensor of the interfacial layer σ_{ls} can be written as [6]

$$\sigma_{ls} = 2C\lambda_{ln}\lambda_{sn}\alpha_{(n)}^2 - p\delta_{ls} - \sigma_{ls}^0. \quad (1)$$

Here, $C = \frac{T\chi R^{02}}{6Na^2h}$, where T is the absolute temperature expressed in energy units, χ is the number of macromolecules attached to a unit area of the surface, R^{02} is the root-mean-square distance between ends of a macromolecule, which is measured far from the surface, N is the number of macromolecule segments, a is the linear size of a segment; $\lambda_{ln} = \frac{\partial x_l'}{\partial x_n}$, where x_n and x_l' are the coordinates of a point belonging to the interfacial layer before and after the deformation, respectively; $\alpha_{(n)}$ is the relative variation of coordinates of a point in the interfacial layer, which is caused by the effect of the surface (and is presented in the coordinate axes shown in Fig. 1); p is the omnidirectional pressure; δ_{ls} is the Kronecker delta; and σ_{ls}^0 is the actual stress caused by fictitious surface forces.

In accordance with the notation accepted, the summation is implied over two identical indices (except that in parentheses). Relation (1) is written for an incompressible body [6]. In this case, the following equalities hold true:

$$\alpha_2 = \alpha_3 = \alpha_1^{1/2}. \quad (2)$$

In the coordinate system shown in Fig. 1, the components of the stress tensor σ_{ls}^0 are:

$$\sigma_{11}^0 = 2C(\alpha_1^2 - \alpha_2^2),$$
$$\sigma_{22}^0 = \sigma_{33}^0 = 0, \quad (3)$$
$$\sigma_{ik}^0 = 0, \text{ if } i \neq k.$$

We consider small strains of the interfacial layer and present λ_{ik} in the form

$$\lambda_{ik} = \delta_{ik} + u_{ik}, \quad (4)$$

where u_{ik} is the derivative of the ith displacement component with respect to the kth coordinate. We can present the function u_{ik} as the following sum of its symmetric (ε_{ik}) and antisymmetric (ω_{ik}) parts:

$$u_{ik} = \varepsilon_{ik} + \omega_{ik}, \quad (5)$$

where $\varepsilon_{ik} = \frac{1}{2}(u_{ik} + u_{ki})$ and $\omega_{ik} = \frac{1}{2}(u_{ik} - u_{ki})$.

From the zero resulting moment of forces applied to an elementary volume of the interfacial layer, it follows that $\omega_{ik} = 0$. Thus, relation (4) can be rewritten in the form

$$\lambda_{ik} = \delta_{ik} + \varepsilon_{ik}, \quad (6)$$

where, by definition, ε_{ik} are the components of the small-strain tensor.

Substituting (6) into (1) and ignoring the terms of the second-order smallness with respect to the strains, we obtain

$$\sigma_{is} = 2C(\delta_{in}\delta_{sn}\alpha_{(n)}^2 + \delta_{sn}\alpha_{(n)}^2\varepsilon_{in} + \delta_{in}\alpha_{(n)}^2\varepsilon_{sn}) - p\delta_{is} - \sigma_{is}^0. \quad (7)$$

In the case of the uniaxial tension along the X_1-axis, we find from (7)

$$\sigma_{11} = 2C(\alpha_1^2 + 2\alpha_1^2\varepsilon_{11}) - p - \sigma_{11}^0. \quad (8)$$

In addition, $\sigma_{22} = \sigma_{33} = 0$ and, consequently, p can be derived from the relation

$$C(\alpha_2^2 + \alpha_3^2 + 2\alpha_2^2\varepsilon_{22} + 2\alpha_3^2\varepsilon_{33}) - p = 0. \quad (9)$$

Substituting into (8) the value of p found from (9) under the condition of interfacial-layer incompressibility

$$\varepsilon_{11} + \varepsilon_{22} + \varepsilon_{33} = 0 \quad (10)$$

and using relations (2) and (3), we obtain

$$\sigma_{11} = 2C(2\alpha_1^2 + \alpha_2^2)\varepsilon_{11}. \quad (11)$$

Relation (11) leads to the following expression for the elastic modulus of the interfacial layer strained along the X_1-axis:

$$E_1 = 2C(2\alpha_1^2 + \alpha_2^2). \quad (12)$$

The relationship

$$p = 2C(\alpha_2^2 + 2\alpha_2^2\varepsilon_{22}) = 2C(\alpha_3^2 + 2\alpha_3^2\varepsilon_{33}) \quad (13)$$

follows also from the condition $\sigma_{22} = \sigma_{33} = 0$.

Using (13) and the incompressibility condition, we find the following relations between strains occurring along and across the axes of tension, respectively:

$$\varepsilon_{11} = -2\varepsilon_{22} = -2\varepsilon_{33}. \quad (14)$$

As a result, the corresponding Poisson's ratios are equal to

$$\nu_{12} = \nu_{13} = 0.5. \quad (15)$$

Similarly, if tension along the X_2-axis occurs, expression (7) yields

$$\sigma_{22} = 2C(\alpha_2^2 + 2\alpha_2^2\varepsilon_{22}) - p. \quad (16)$$

Under the condition $\sigma_{11} = \sigma_{33} = 0$, relations (2), (3),

(10), and (16) lead to the formula

$$\sigma_{22} = 4C\frac{\alpha_2^2(2\alpha_1^2+\alpha_2^2)}{\alpha_1^2+\alpha_2^2}\varepsilon_{22}, \quad (17)$$

which allows elastic modulus of the interfacial layer for strains along the X_2-axis to be expressed as

$$E_2 = 4C\frac{\alpha_2^2(2\alpha_1^2+\alpha_2^2)}{\alpha_1^2+\alpha_2^2}. \quad (18)$$

It follows also from the condition $\sigma_{11} = \sigma_{33} = 0$ that

$$p = 2C(\alpha_2^2 + 2\alpha_1^2\varepsilon_{11}) = 2C(\alpha_3^2 + 2\alpha_3^2\varepsilon_{33}). \quad (19)$$

Using (2), (19), and the incompressibility condition, we derive the following relations for strains occurring along and across the axes of tension, respectively:

$$\varepsilon_{22} = -\frac{\alpha_1^2+\alpha_2^2}{\alpha_2^2}\varepsilon_{11} = -\frac{\alpha_1^2+\alpha_2^2}{\alpha_1^2}\varepsilon_{33}. \quad (20)$$

As a result, the corresponding Poisson's ratios are

$$\nu_{21} = \frac{\alpha_2^2}{\alpha_1^2+\alpha_2^2}, \quad \nu_{23} = \frac{\alpha_1^2}{\alpha_1^2+\alpha_2^2}. \quad (21)$$

Similarly, for tension occurring along the coordinate X_3-axis, elastic modulus of the interfacial layer for strains along the direction of this axis is defined by the formula

$$E_3 = 4C\frac{\alpha_2^2(2\alpha_1^2+\alpha_2^2)}{\alpha_1^2+\alpha_2^2} \quad (22)$$

and the corresponding Poisson's ratios are

$$\nu_{31} = \frac{\alpha_2^2}{\alpha_1^2+\alpha_2^2}, \quad \nu_{32} = \frac{\alpha_1^2}{\alpha_1^2+\alpha_2^2}. \quad (23)$$

Formula (1) and conditions of the corresponding pure-shear loading with formula (2) taken into account yield the relations

$$\begin{aligned}\sigma_{12} &= 2C(\alpha_1^2+\alpha_2^2)\varepsilon_{12},\\ \sigma_{13} &= 2C(\alpha_1^2+\alpha_2^2)\varepsilon_{13},\\ \sigma_{23} &= 4C\alpha_2^2\varepsilon_{23}.\end{aligned} \quad (24)$$

As a result, expressions for the elastic-shear moduli are written out as

$$G_{12} = G_{13} = C(\alpha_1^2+\alpha_2^2), \quad G_{23} = 2C\alpha_2^2. \quad (25)$$

The relations derived lead to the following equalities:

$$\begin{aligned}&E_2 = E_3, \quad \nu_{12} = \nu_{13}, \quad \nu_{21} = \nu_{31}, \quad \nu_{23} = \nu_{32},\\ &\frac{\nu_{12}}{E_1} = \frac{\nu_{21}}{E_2}, \quad G_{23} = \frac{E_2}{2(1+\nu_{23})},\\ &\nu_{12}+\nu_{23}+\nu_{31} = 3/2.\end{aligned} \quad (26)$$

Thus, within the framework of the description proposed, the interfacial layer is represented as an incompressible transversely isotropic medium with the following five independent constants: E_1, E_2, ν_{12}, G_{12}, and G_{23}. Consequently, this layer cannot be described within the scope of relations valid for an isotropic medium. The dependence between stresses and strains (the generalized Hooke's law) has the form

$$\begin{aligned}\varepsilon_{11} &= \frac{1}{E_1}\sigma_{11} - \frac{\nu_{12}}{E_1}\sigma_{22} - \frac{\nu_{12}}{E_1}\sigma_{33},\\ \varepsilon_{22} &= -\frac{\nu_{12}}{E_1}\sigma_{11} + \frac{1}{E_2}\sigma_{22} - \frac{\nu_{23}}{E_2}\sigma_{33},\\ \varepsilon_{33} &= -\frac{\nu_{12}}{E_1}\sigma_{11} - \frac{\nu_{23}}{E_2}\sigma_{22} + \frac{1}{E_2}\sigma_{33},\\ \varepsilon_{12} &= \frac{1}{2G_{12}}\sigma_{12},\\ \varepsilon_{13} &= \frac{1}{2G_{13}}\sigma_{13},\\ \varepsilon_{23} &= \frac{1}{2G_{23}}\sigma_{23}.\end{aligned} \quad (27)$$

The relationships derived can be used for numerically evaluating elastic properties of matrix composites with allowance for features of the interfacial layer. In this case, values of α_n enter into the formulas as a parameter, which should be determined beyond the scope of the approach under discussion. Relationship (2) allows only one parameter α_1 to be used, which we denote furthermore as α. Depending on both the number of the segments N and the density χ of macromolecules attached to the filling-agent surface, this parameter can be evaluated according to the data taken from [4, 5]. In these studies, distances between ends of a free macromolecule (R^0) and of that, whose one end is attached to the surface (R), are determined by methods of collisional molecular dynamics (a numerical experiment). Based on these data, values of $\alpha = R/R^0$ are found. The constant C in expression (1) depends on N, h, and χ. According to the data of [7, 8], the scaling dependence

$$h = aN\chi^{1/3} \quad (28)$$

is reproduced in the case when the surface density of attached macromolecules is not very low.

Using (28), we express C in terms of N and χ as:

$$C \simeq \frac{T\chi^{2/3}}{2a^3N}. \quad (29)$$

Relation (29) and values of α allow dependences of E_1, E_2, G_{12}, and G_{23} to be constructed as functions of N and χ. Figure 2a shows the ratios between the elastic moduli of the interfacial layer and $2CN$ as a function of N for small surface density of attached macromolecules (the macromolecules do not interact). Figure 2b pre-

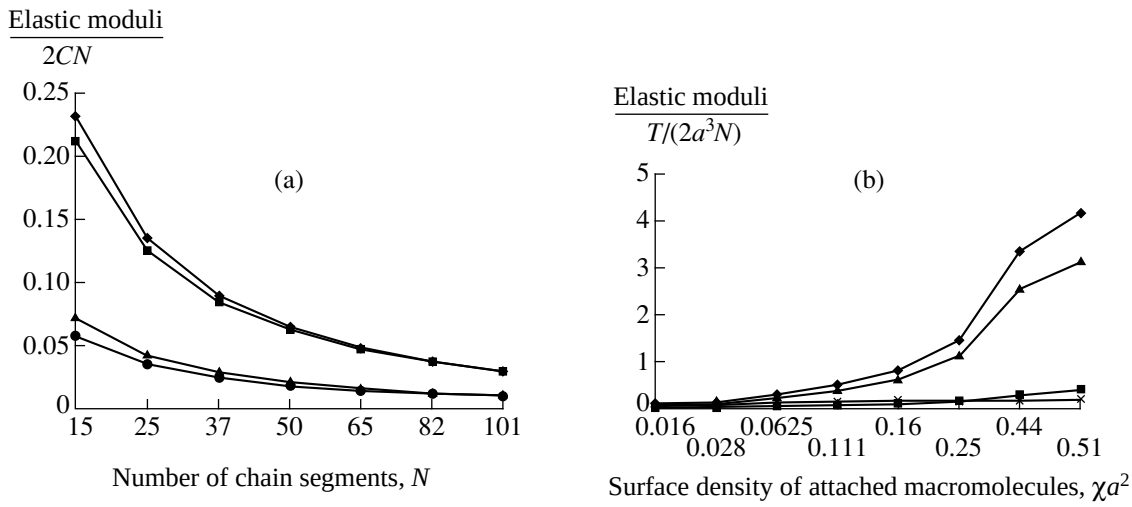

Fig. 2. Dependence of the elastic moduli of the interfacial layer on (a) the length of macromolecular chains and (b) the surface density of macromolecular chains: (◆) E_1, (■) E_2, (▲) G_{12}, and (●) G_{23}.

sents the ratios between the elastic moduli of the interfacial layer and the quantity $\frac{T}{2a^3N}$ as functions of χa^2 for $N = 15$.

Thus, the following conclusions can be made.

An interfacial layer formed by those macromolecules, whose one end is attached to active centers of a filling-agent surface, represents transversely isotropic medium characterized by five elastic constants. Structure anisotropy of the interfacial layer is explained by both the effect of the surface on the macromolecule conformation and, in the case of a high surface density of attached macromolecules, by their interaction with each other. Elastic properties of the interfacial layer depend strongly on the density of attached macromolecules on the filling-agent surface.

ACKNOWLEDGMENTS

This work was supported by the Russian Foundation for Basic Research, project no. 99-01-01250.

REFERENCES

1. J. B. Donnet, in *Proceedings of IRC'94* (Moscow, 1994), Vol. 1, pp. 129–138.
2. Yu. S. Lipatov and L. M. Sergeeva, *Adsorption of Polymers* (Naukova Dumka, Kiev, 1972).
3. *Structure and Properties of Polymeric Surface Layers*, Ed. by. Yu. S. Lipatova (Naukova Dumka, Kiev, 1972).
4. A. S. Lemak, N. K. Balabaev, Yu. N. Karnet, and Yu. G. Yanovskiĭ, Mekh. Kompoz. Mater. Konstr. **1**, 152 (1995).
5. A. S. Lemak, N. K. Balabaev, Yu. N. Karnet, and Yu. G. Yanovsky, J. Chem. Phys. **108**, 797 (1998).
6. V. É. Zgaevskiĭ and Yu. G. Yanovskiĭ, Mekh. Kompoz. Mater. Konstr. **3**, 105 (1997).
7. P. G. Khalatur, Makromol. Chem., Macromol. Symp. **44**, 23 (1991).
8. S. Grest Gary, J. Chem. Phys. **105**, 5532 (1996).

Translated by Yu. Verevochkin

Doklady Physics, Vol. 45, No. 4, 2000, pp. 179–182. Translated from Doklady Akademii Nauk, Vol. 371, No. 5, 2000, pp. 621–624.

MECHANICS

Stability of a Hypersonic Boundary Layer with a Pressure Gradient

Corresponding Member of the RAS V. M. Fomin, A. A. Maslov, A. A. Sidorenko, and A. N. Shiplyuk

Received August 31, 1999

The local pressure gradient, caused by either an incident shock wave or a reverse flow turn, is known to violently affect characteristics of a hypersonic boundary layer and, under certain conditions, can result even in its separation. The investigation of both laminar and turbulent separation flows is of great interest, because they arise often in the case of air flow around aircrafts. The effect of a pressure gradient and a separation induced by it on the primary instability of a laminar boundary layer remains to be a less investigated matter.

As previous studies have shown, the influence of a pressure gradient on the value of the Reynolds number in the laminar-to-turbulent transition decreases with increasing the Mach number [1, 2]. In the case of a hypersonic boundary layer, the pressure gradient selectively affects various types of perturbances. For example, oblique waves of the first mode are much more stable in the presence of unfavorable (positive) pressure gradients than two-dimensional waves [3]. The theoretical analysis [4] of stability for a boundary layer shows that favorable (negative) pressure gradients exhibit a stabilizing action on perturbances of the second mode decreasing a peak value of the growth coefficient and shifting it to the higher-frequency region, thereby narrowing the frequency range for perturbances being intensified.

In experimental investigations of the boundary-layer stability, as a rule, the development of natural perturbances is studied. A disadvantage of this approach is the impossibility to obtain the complete spatial characteristic for the wave field of perturbances in the boundary layer and, thus, the impossibility of detailed comparison with results of theoretical analysis.

The method of artificial perturbances is free of the disadvantage indicated and has found wide application in investigating stability of incompressible flows. The first successful attempt of using artificial perturbances in a compressible boundary layer was made in [5] and, nowadays, the attempts are made to use this method for investigating stability of a hypersonic boundary layer [6, 7].

The method of artificial wave packets based on artificial perturbances is widely applied for investigating stability of a supersonic boundary layer [8, 9]. This method offers undeniable advantages, because it enables us to obtain a complete space–time characteristic of the wave field in a boundary layer.

The concept of the method is based on introducing a local periodic perturbance with a given phase and a reasonably small amplitude. Thus, a wave packet is formed in the boundary layer. This packet can be presented as a result of interference of a set of plane waves (at the linear phase of evolution). Three-dimensional analysis makes it possible to obtain the distributions for amplitudes and phases at each point and to reconstruct the field of artificial perturbances. The further spatial spectral analysis makes it possible to isolate individual plane waves with characteristic tilt angles and phase velocities and to follow their evolution.

The use of artificial perturbances for investigating the stability of a boundary layer with a pressure gradient and the separation area is especially urgent because there are additional types of perturbances in this case (second-mode perturbances or Görtler vortices), which are difficult to separate. In spite of attempts to apply this method for studying a hypersonic boundary layer, this paper represents the first successful experience in using the artificial perturbances for investigating the stability of a high-velocity boundary layer.

The experiments were carried out in the T-326 hypersonic wind tunnel of the Institute of Theoretical and Applied Mechanics, Siberian Division, Russian Academy of Sciences. The Mach number of the approach stream was chosen to be $M_\infty = 5.92$, and the unit Reynolds number was $Re_1 = 12.5 \times 10^6$ m^{-1}. As an experimental model, we used an acute-angled cone 166 mm long with a semi-apex angle of 7° and a compression angle of 10°. The axial-symmetry conditions for flows around the cone were fulfilled. For the flow parameters indicated, a laminar boundary layer with the separation area near the break of the cone generatrix

Institute of Theoretical and Applied Mechanics, Siberian Division, Russian Academy of Sciences, Institutskaya ul. 4/1, Novosibirsk, 630090 Russia

1028-3358/00/4504-0179$20.00

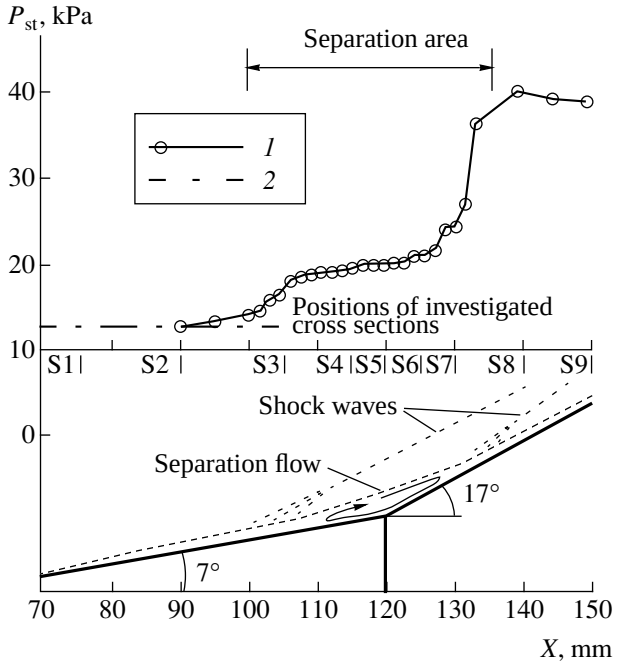

Fig. 1. Static-pressure distribution at the model wall and the diagram for the flow near the separation area: (*1*) experimental data; (*2*) calculation results for nonviscous flow at the cone.

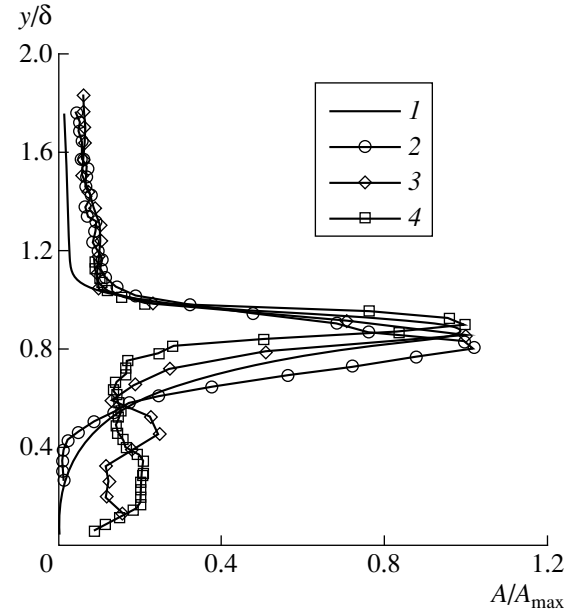

Fig. 2. Distributions of the normalized pulsation amplitude for the mass flow rate across the boundary layer (f = 40 kHz): (*1*) calculation according to the locally cocurrent theory; (*2*) artificial perturbances, the cross section S2; (*3*) natural perturbances, the cross section S2; (*4*) natural perturbances, the cross section S5.

was realized in the model. The configuration of the flow near the separation area was investigated by various methods including visualization of the limiting streamlines, Schlieren visualization, measurement of the thermal flow on the model surface, measurement of the velocity field by a Pitot tube and a thermal flowmeter. The flow diagram obtained on the basis of these investigations is presented in Fig. 1. In the same figure, the static-pressure distribution at the model surface is shown. As is seen from Fig. 1, the separation area is localized within 100–135 mm. It is worth noting that in this case, the laminar separation of the boundary layer with the laminar join arises. This fact is confirmed by the obtained distributions of flow parameters in the boundary layer.

In the same figure, positions of the cross sections (S1–S9), in which we investigated the distribution of pulsation characteristics of the boundary layer, are given. The first two cross sections S1 and S2 are located upstream of the separation area; the cross sections S4, S5, and S6 are in the region of the developed separation flow; the cross sections S8 and S9 are downstream of the join line; and the cross sections S3 and S7 lie in the vicinity of the separation and join points.

In this study, we used as a source of perturbances an electric discharger placed at a distance of 60 mm from the tip of the model and operating at a frequency $f = 40$ kHz [a dimensionless frequency parameter is $F = 2\pi f/(\mathrm{Re}_1 U_e) = 0.22 \times 10^{-4}$]. The principle of the source action is based on the electric discharge in a closed chamber connected with the model surface through an orifice 0.4 mm in diameter. The average and pulsation characteristics of the flow in the boundary layer were measured by a direct-current thermal flowmeter with the frequency range up to 200 kHz.

The equipment used in this experiment and methods of data acquisition enable us to investigate the evolution of artificial perturbances, whose amplitudes attain the level of natural pulsations of the boundary layer. For detecting a signal corresponding to an artificially introduced perturbance, we used a narrow-band filter tuned at the perturbance-source frequency. Recording the alternating component of the thermal-flowmeter signal was synchronized with igniting the electric discharge in the perturbance-source chamber. In order to eliminate an influence of a random non-correlated noise and contribution of natural perturbances, we performed multiple summing up and averaging the thermal-flowmeter signal.

In a hypersonic boundary layer, the transverse distribution of natural-pulsation amplitudes is known to have a pronounced maximum or a “critical layer” located near the upper interface of the boundary layer in which a larger fraction of the pulsation energy is concentrated [10]. The investigations of evolution of natural perturbances (Fig. 2) have shown that, for the given model, this feature is observed in both the boundary layer and free shear flow above the separation area. The measurements of artificial-perturbance distributions and their comparison with calculation results show that

the perturbance introduced has a similar distribution, which is characteristic of the first-mode vortex perturbances. Therefore, the spatial distribution for the characteristics of artificial perturbances were investigated only in the "critical layer."

In each of the cross sections indicated, we have obtained the distributions for amplitudes and phases of artificial perturbances in the transversal direction, owing to which we have managed to obtain the spatial spectrum. For analysis, we used the Fourier transformation with application of spectral windows. The amplitude spectra over the transversal wave number β are presented in Fig. 3. The value of the two-dimensional-wave amplitude ($\beta = 0$) was chosen as a normalizing coefficient for each cross section. It is seen that the source generates a wave packet with a majority of waves having low tilt angles (the cross section S1). Thereafter, the plane-wave contribution ($\beta = 0$) decreases sharply, and the oblique waves begin to play the principal role (the cross section S3). The wave with the tilt angle of ~60° ($\beta = 0.7$), which manifests itself already in the second cross section, is detected in the wave spectra for all other cross sections. It is necessary to note an increase in the contribution of the two-dimensional wave in the spectrum of the S4 cross section located immediately downstream of the separation line. This testifies to the fact that the circular separation line is a generator of two-dimensional perturbances. In the process of evolution of the wave packet in the mixing layer above the separation area, the plane wave decays rapidly, and the oblique wave with the wave-vector tilt of ~60° (the cross sections S5–S9) begins to dominate anew. For the cross sections (S7, S9) located downstream of the separation area, we observe a peak corresponding to a wave propagating at an angle of ~80° ($\beta \simeq 1.8$) in the transversal wave spectra. The appearance of strongly oblique perturbances is characteristic for the phenomenon of the subharmonic resonance [11] and evidences in favor of the onset of nonlinear processes in the boundary layer.

Owing to the fact that the flow under study is rather complicated, while the number of cross sections investigated is limited, it seems to be impossible to perform the complete spectral analysis in the longitudinal direction. To obtain the longitudinal phase velocities C_x for the waves with various tilt angles χ, we used a simplified procedure. The longitudinal wave number α_r was estimated from the phase spectra $\varphi(\beta)$ obtained from the formula $\alpha_r(\beta) = \dfrac{\Delta\varphi(\beta)}{\Delta x}$, and the phase velocity of perturbances was determined as $C_x(\chi) = \dfrac{\lambda f}{U_e}$, where $\chi = \arctan\dfrac{\beta}{\alpha_r}$ is the angle between the wave front and the main-stream direction, U_e is the velocity at the boundary-layer interface, and $\lambda = \dfrac{2\pi}{\alpha_r}$ is the perturbance wavelength.

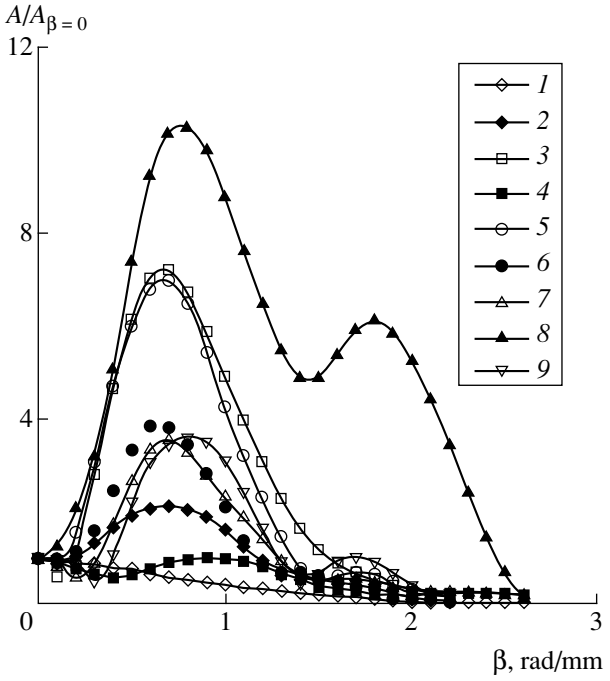

Fig. 3. Amplitude spectra of artificial perturbances as a function of the transversal wave number β: numbers (*1–9*) correspond to the cross sections S1–S9.

It is necessary to note that these estimates are of an integral nature, therefore, we can make only general conclusions on the structure of the wave packet. In Fig. 4, we present the dependences $C_x(\chi)$ and $C_x'(\chi) = 1 - \dfrac{1}{M_e\cos\chi}$ for the perturbance phase velocity and the maximum velocity of propagation of acoustic perturbances, respectively, on the wave-front tilt angle. In the same figure, the results of the theoretical calculations for the phase velocity of vortex perturbances with a frequency of 40 kHz as a function of the tilt angle χ are shown. Figure 4 demonstrates that, for the perturbances located below the curve C_x', the major contribution is caused by acoustic waves, while above this curve—by the vortex waves. In the separation area and further downstream, the perturbance phase velocities with the angles χ below 55° are smaller than C_x'. Thus, the acoustic perturbances prevail in this zone. At the same time, an increase in the integral phase velocity C_x for $\chi = 20°–35°$ indicates the presence of waves of the vortex nature with these angles χ. For tilt angles above 55°, the vortex perturbances dominate.

This study is the pioneering example of the use of artificial perturbances for investigating complicated processes occurring when a hypersonic boundary layer

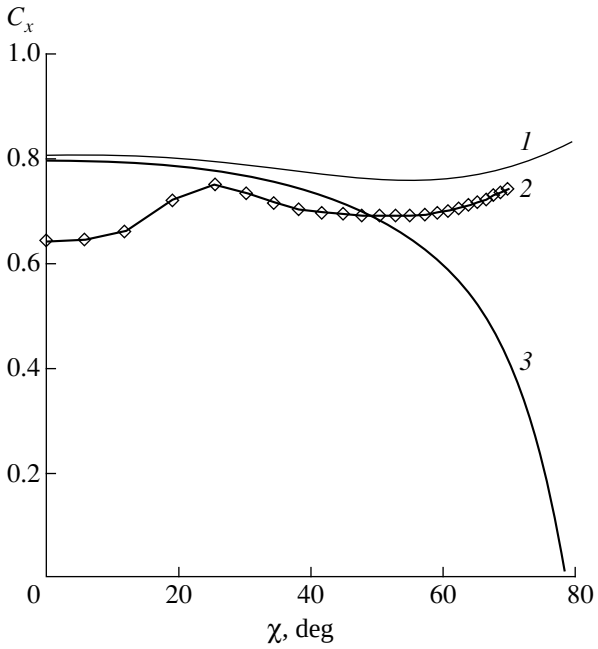

Fig. 4. Phase velocity of artificial perturbances as a function of the wave-vector tilt angle χ: (*1*) results of calculations according to the locally cocurrent theory; (*2*) experimental data; (*3*) maximum phase velocity of acoustic perturbances C_x'.

interacts with a local pressure gradient. The wave spectra obtained and the estimates made for wave-tilt angles show that the appearance of two-dimensional perturbances is observed in the separation area, which is associated with a high susceptibility of the boundary layer in the inhomogeneity zones. From the estimates of perturbance phase velocities, it follows that the acoustic waves prevail at the wave-vector tilts lower than 55°, while the vortex waves dominate at higher tilt angles.

ACKNOWLEDGMENTS

This work was supported by the Russian Foundation for Basic Research, project no. 98-01-00735.

REFERENCES

1. N. M. Shapiro, J. Aeronaut. Sci. **23**, 81 (1956).
2. H. Weil, J. Aeronaut. Sci. **18**, 311 (1951).
3. Y. H. Zurigat, A. H. Nayfeh, and J. A. Masad, AIAA Papers, No. 90-1451 (1990).
4. M. R. Malik, AIAA Papers, No. 87-1414 (1987).
5. M. K. James, Jr., Air Force Reports, No. BSD-TR-67-213, V2 (1967).
6. T. C. Corke and D. A. Cavalieri, AIAA Papers, No. 97-1817 (1997).
7. W. L. Dale and P. S. Steven, AIAA Papers, No. 98-0436 (1998).
8. A. D. Kosinov, A. A. Maslov, and S. G. Shevel'kov, Izv. Akad. Nauk SSSR, Mekh. Zhidk. Gaza, No. 6, 54 (1990).
9. A. D. Kosinov and S. G. Shevel'kov, in *Proceedings of IUTAM Symposium, 1991* (Springer, Berlin, 1991), pp. 741–745.
10. A. A. Maslov, A. A. Sidorenko, and A. N. Shiplyuk, Prikl. Mekh. Tekh. Fiz. **38**, 71 (1997).
11. A. D. Kosinov, N. V. Semionov, S. G. Shevelkov, and O. I. Zinin, in *Proceedings of IUTAM Symposium, 1994* (Springer, Berlin, 1994), pp. 196–205.

Translated by V. Bukhanov

Doklady Physics, Vol. 45, No. 4, 2000, pp. 183–185. Translated from Doklady Akademii Nauk, Vol. 371, No. 6, 2000, pp. 770–772.

MECHANICS

On the Structure of a Stable (in the Lyapunov Sense) Attractor

O. V. Druzhinina and A. A. Shestakov

Presented by Academician V.V. Rumyantsev July 7, 1999

Received July 14, 1999

An urgent problem in the Lyapunov stability theory [1–3] is finding criteria that make it possible to distinguish simple-attracting sets (simple attractors) from strange-attracting sets (strange attractors) [4–6]. There is a principal distinction in the behavior of dynamic systems with simple and strange attractors, because the former systems are regular, while the latter ones are random.

In this paper, it is shown that if the invariant set $A \subset R^n$ of a dynamic system φ: $R^n \longrightarrow R^n$ is compact, attracting, stable in the Lyapunov sense, and there exists a trajectory, whose closure is dense in A, then the set A is a stable torus and, hence, the dynamic system will be regular.

According to the assumption of Ruelle and Takens, all trajectories of strange attractors are unstable in the Lyapunov sense, and this was taken by these authors as a starting point for explaining the turbulence phenomenon. They proceed from the following turbulence definition: "… the motion of a liquid medium is turbulent if this motion is described by the integral curve of a vector field, which tends to an nonempty set A being not an equilibrium state or a closed orbit" [6]. Theorems proved by us elucidate the attractor structure in various systems in the case of the absence of the turbulence in the Ruelle–Takens sense.

Following [7, 8], we refer to the invariant set $M \subset R^n$ of the dynamic system φ: $R^n \longrightarrow R^n$ as stable in the Lyapunov sense as $t \longrightarrow +\infty$ provided that the condition

$$\forall \varepsilon > 0\ \exists \delta > 0,\ \ d(m, x) < \delta \Rightarrow d(\varphi(t, m), \varphi(t, x)) < \varepsilon$$

is satisfied at each point m of this set for all $t \in R^+$, where $x \in M$ and d is the metric of the space R^n.

In other words, the stability of a set in the Lyapunov sense implies that all points of this set are stable in the Lyapunov sense. We note, that the equilibrium state, periodic trajectory, and almost-periodic trajectory with a compact closure are sets stable in the Lyapunov sense.

State Russian Open Technical University of Communications, Chasovaya ul. 22/2, Moscow, 125808 Russia

We will denote positive and negative limiting sets of a point $x \in R^n$ as $\omega(x)$ and $\alpha(x)$, respectively. An open sphere of a radius δ with the center at the point $y \in R^n$ is denoted as $B_\delta(y)$.

In [8], the following statement on the uniform stability of the compact set $M \subset R^n$ is established.

Statement 1. *Let M be a compact set stable in the Lyapunov sense as $t \longrightarrow +\infty$, and $m_1 \in M$. Then, for each number $\varepsilon > 0$, there exists a number $\delta > 0$, such that*

$$d(m_1, m_2) < \delta \Rightarrow d(\varphi(t, m_1), \varphi(t, m_2)) < \varepsilon\ \ \forall t \in R^+,\ \ m_2 \in M. \quad (1)$$

Next, we formulate lemmas required in what follows.

Lemma 1. *Let*: (*1*) *A be a compact set stable in the Lyapunov sense as $t \longrightarrow +\infty$*; (*2*) *$A$ be an attractor as $t \longrightarrow +\infty$, i.e., for arbitrary neighborhood U of the set A, there exist a neighborhood V of the set A, such that*

$$\varphi(t, V) \subset U\ \ \forall t \in R^+ \quad \text{and} \quad \omega(x) \subset A\ \ \forall x \in V; \quad (2)$$

(*3*) *there exists a trajectory $C(a)$, $a \in A$, which is dense everywhere in the set A. Then, for an arbitrary $\lambda > 0$, there exists a number $\delta(\lambda) > 0$, such that*

$$\forall b_1, b_2 \in A \quad (3)$$
$$d(b_1, b_2) < \delta(\lambda) \Rightarrow d(\varphi(t, b_1), \varphi(t, b_2)) < \lambda\ \ \forall t \in R.$$

Lemma 1 is a direct corollary of Statement 1, as well as of the definition of the attractor, and the presence in the set A of the trajectory dense everywhere.

Corollary 1. *For arbitrary two points $b_1, b_2 \in A$, $b_1 \neq b_2$, the relation*

$$\exists \mu > 0,\ d(\varphi(t, b_1), \varphi(t, b_2)) > \mu\ \ \forall t \in R \quad (4)$$

takes place.

Lemma 2. *Let the prerequisites of Lemma* 1 *be satisfied. Then, the set A is the minimum set of almost periodic* (*in the Bohr sense*) *trajectories.*

Proof. We prove initially, that

$$\exists a \in A \quad \overline{C^+(a)} = A. \quad (5)$$

1028-3358/00/4504-0183$20.00

By virtue of condition (3) of Lemma 1,

$$\exists a \in A \quad \overline{C(a)} = A.$$

We assume that if $b \in \alpha(a)$, then $\omega(b) \supset C(a)$. Indeed, let $x = \varphi(a, t_1)$, and we choose a number $\varepsilon > 0$. Since the point $b \in \alpha(a)$ is stable in the Lyapunov sense, then, for an arbitrary number $c \in R$, there exist $t_2 < c$ and $t_1 > t_2$, such that $d(\varphi(t_2 + t, a), \varphi(t, b)) > \varepsilon$ $\forall t \in R^+$ and $d(x, \varphi(t_1 - t_2, b)) > \varepsilon$. This proves the inclusion. Since $\alpha(a)$ is invariant and closed, then $\alpha(a) \supset \omega(a)$ and, thus, $\omega(a) \supset C(a)$. Since $\overline{C^+(a)} \supset \omega(a)$, then $\overline{C^+(a)} = A$. Thus, statement (5) is established.

We now show that the set A is the minimum one. To do this, we choose $b \in A$ and $\varepsilon > 0$. Then, by virtue of arguments proved above, there exists the point $a_1 \in A$, such that $\overline{C^+(a_1)} = A$ and $d(\varphi(t, a_1), \varphi(t, b)) < \varepsilon$ $\forall t \in R^+$. Since ε is arbitrary, then $\overline{C^+(b)} = A$.

Because the point b is arbitrary, each half-trajectory of the set A is dense everywhere in A, and hence, the set A consists of almost periodic trajectories. Thus, Lemma 2 is proved.

Let A be an attractor as $t \longrightarrow +\infty$. Denote the attraction set as $\Pi(A)$, such that

$$\Pi(A) = \{x \in R^n: \omega(x) \in A\}.$$

In addition, for an arbitrary point $a \in A$, we define

$$K(a) = \{x \in \Pi(A): d((\varphi(t, x), \varphi(t, a)) \longrightarrow 0, (t \longrightarrow +\infty))\}.$$

It is easy to show that for different points a_1 and a_2, the sets $K(a_1)$ and $K(a_2)$ are nonintersecting and

$$\Pi(A) = \bigcup\{K(a): a \in A\}. \tag{6}$$

We now establish equality (6). Indeed, let $x \in \Pi(A)$ and $\tau_n \longrightarrow +\infty$. Since $\omega(x) \subset A$, then we can choose a subsequence $s_n \longrightarrow +\infty$, such that $\varphi(s_n, x) \longrightarrow y \in A$ as $s_n \longrightarrow +\infty$. We define the sequence $y_{s_n} = \varphi(s_n, y)$. Since $y_{s_n} \in A$, then we can choose the convergent subsequence y_{s_k}, such that $y_{s_k} \longrightarrow a$ as $k \longrightarrow +\infty$. The point a is stable in the Lyapunov sense. Therefore, $d(\varphi(s_k, a)\ \varphi(s_k, x)) \longrightarrow 0$ as $k \longrightarrow +\infty$. Consequently, from the stability of the point a, it follows that $x \in K(a)$. Thereby, the validity of relation (6) is proved.

Lemma 3. *The attraction set $\Pi(A)$ is open and stable in the Lyapunov sense as $t \longrightarrow +\infty$.*

Proof. The property of openness for the set $\Pi(A)$ is established in [8]. We will prove that the set $\Pi(A)$ is stable in the Lyapunov sense. By virtue of Statement 1, for an arbitrary $\varepsilon > 0$, there exists $\delta(\varepsilon) > 0$, such that

$$a, b \in A,$$
$$d(a, b) < \delta \Rightarrow d(\varphi(t, a), \varphi(t, b)) < \varepsilon \ \forall t \in R^+.$$

Let $\varepsilon > 0$ and $y \in \Pi(A)$. We choose the number $\lambda > 0$, such that $B_\lambda(y) \in \Pi(A)$ and the inequality

$$r(\varphi(t, x), A) < \frac{1}{2}\delta\left(\frac{\varepsilon}{2}\right), \ x \in B_\lambda(y), \ t > \tau$$

is satisfied for a certain $\tau > 0$, where r is the distance from the point to the set.

The existence of the number τ follows from the definition of the attractor. Due to the continuity of the dynamic system, we can choose $\lambda_1 < \lambda$, such that the following expressions hold:

$$d(\varphi(t, x), \varphi(t, y)) < \frac{1}{2}\delta\left(\frac{\varepsilon}{2}\right),$$
$$x \in B_{\lambda_1}(y), \quad t \in [0, \tau].$$

Hence,

$$d(\varphi(t, x), \varphi(t, y)) < \varepsilon \ \forall (t, x) \in R^+ \times B_{\lambda_1}(y).$$

Thus, Lemma 3 is proved.

Let A be a set for which conditions (*1*)–(*3*) of Lemma 1 are satisfied. We show that if $a \in A$ then, for each neighborhood N_1 of the point a, there exists the neighborhood $N_2 \subset N_1$, such that

$$x \in (N_2 \cap K(b)) \Rightarrow b \in N_1. \tag{7}$$

Actually, let N_1 be the neighborhood of a point $a \in A$. We may take that N_1 is an open sphere $B_\lambda(a)$ with the radius λ and $B_\lambda(a) \subset \Pi(A)$. From the property of stability in the Lyapunov sense of the point a, it follows that

$$\exists \delta_1 > 0$$
$$x \in B_{\delta_1}(a) \Rightarrow d(\varphi(t, x), \varphi(t, a)) < \frac{1}{2}\delta(\lambda) \ \forall t \in R^+. \tag{8}$$

The choice of the number $\delta(\lambda)$ is performed according to (3). Let $x \in B_{\delta_1}(a) \cap K(b)$. For large values of s, we have $d(\varphi(s, b), \varphi(s, x)) < \frac{1}{2}\delta(\lambda)$. Consequently,

$$d(\varphi(-s, \varphi(s, b)), \varphi(-s, \varphi(s, a))) = d(b, a) < \lambda.$$

Implication (7) follows from the inequality obtained and condition (3) of Lemma 1.

The following theorem also takes place:

Theorem 1. *Let the invariant set $A \subset R^n$ of the dynamic system φ: $R^n \longrightarrow R^n$ be compact, attracting as $t \longrightarrow +\infty$, stable in the Lyapunov sense as $t \longrightarrow +\infty$, and there exist in A a trajectory everywhere dense.*

Then, the set A is a torus. In particular, if A is a hyperbolic set, then it will be either an equilibrium state or a closed trajectory.

Proof. By lemmas 1 and 2, the set A is a minimum set of almost-periodic trajectories. We impart to A the structure of a compact topologic group, which is always possible [8]. The set is compact, and, consequently, by the Pontryagin theorem [9], the commutative connected finite-dimensional topologic group is locally homeomorphic to the set being the Cartesian product $\Gamma_1 \times \Gamma_2$. Here, Γ_1 is the compact zero-dimensional topological group and Γ_2 is the n-dimensional set homeomorphic to the sphere $|x| < 1$. The set Γ_1 is discrete or perfect. A perfect zero-dimensional set from R^n is known from [8] to be the Cantor set. Therefore, A is a local disk or a product of the Cantor set by an n-dimensional element. It follows from the Pontryagin theorem that if A is connected locally, then A is the Cartesian product of n circumferences, i.e., A is an n-dimensional torus T^n.

We now establish that A possesses the property of a local connectedness. To do this, we assume the contrary. Then, each point $a \in A$ has a neighborhood N_1, such that $A \cap N_1$ is a product of a n-dimensional element and a Cantor set. Let N_2 be the connected neighborhood of a point $a \in A$. Since for any neighborhood N_1, there exist a neighborhood $N_2 \subset N_1$, such that

$$x \in N_2,\ x \in K(b) \Rightarrow b \in N_1,$$

then we can assume that

$$N_2 \subset \cup\{K(b)\colon b \in A \cap N_1\}.$$

Due to the property of the intersection $A \cap N_1$, A can be decomposed into a sum of two sets A_i ($i = 1, 2$), such that

$$A_i \cap N_2 = \varnothing,$$
$$d(a_1, a_2) > c > 0\ \ \forall a_i \in A_i\ \ (i = 1, 2).$$

We now assume that

$$U_i = \cup\{K(b)\colon b \in A_i\} \cap N_2.$$

Next, we show that sets U_i are open. Indeed, let $y \in K(b) \cap N_2$ and $b \in A_i$. According to Lemma 3, the set $\Pi(A)$ is stable in the Lyapunov sense. Hence, we have

$$\exists \varepsilon > 0,$$
$$d(x, y) < \varepsilon \Rightarrow d(\varphi(t, x), \varphi(t, y)) < \frac{1}{2}\delta(\lambda),$$

where $\delta(\lambda)$ is a number corresponding to the number $\lambda > 0$ chosen in the same manner as in the item (3) of Lemma 1. If $x \in B_\varepsilon(y) \cap N_2 \cap K(a)$, then for a sufficiently large t, we have $d(\varphi(t, a), \varphi(t, b)) < \delta(\lambda)$. Hence, $d(a, b) < \lambda$. From the last inequality and statement (7), it follows that $x \in U_i$, $U_1 \cap U_2 = \varnothing$, $U_1 \cup U_2 = N_2$, and the set N_2 is a combination of two open nonempty sets, which contradicts to the connectedness of the set N_2. The contradiction obtained proves the local connectedness of the set A. Therefore, the set A is a torus. The theorem is proved.

Theorem 1 is generalized to the case of a connected metric space X and a finite-dimensional attractor $A \subset X$. Namely, the following theorem takes place.

Theorem 2. *Let X be a locally connected metric space. Let the invariant set $A \subset X$ of a dynamic system φ: $X \longrightarrow X$ be finite-dimensional, attracting as $t \longrightarrow +\infty$, stable in the Lyapunov sense as $t \longrightarrow +\infty$, and a trajectory dense everywhere there exist in A. Then, the set A is a topological torus. In particular, if A is hyperbolic set, then it will be either an equilibrium state, or a closed trajectory.*

The proof of Theorem 2 is performed in the same manner as that of Theorem 1.

Comments to Theorem 2. It was established by V. V. Nemytskiĭ and V. V. Stepanov [8], that for any compact metric group G, there exists a dynamic system, such that G is a minimal set of almost-periodic trajectories in this dynamic system. Therefore, any such a group can be a stable attractor, and hence, the condition of Theorem 2 stating that the set A is contained in a certain closed locally connected metric space cannot be relaxed.

ACKNOWLEDGMENTS

The authors are grateful to Academician V.V. Rumyantsev for his attention to this work.

REFERENCES

1. A. M. Lyapunov, *General Problem of Stability of Motion* (Gostekhizdat, Moscow, Leningrad, 1950).
2. V. V. Rumyantsev, Differ. Uravn. **19**, 739 (1983).
3. N. G. Chetaev, *Stability of Motion* (GITTL, Moscow, 1955).
4. G. Alland and E. S. Thomas, J. Differ. Equat. **15**, 158 (1974).
5. Z. Nitecki, *Differentiable Dynamics. An Introduction to the Orbit Structure of Diffeomorphism* (MIT Press, Cambridge, 1971).
6. D. Ruelle and F. Takens, Comment. Math. Phys. **20**, 167 (1971).
7. A. A. Markoff, Math. Zeitschr. **36**, 708 (1933).
8. V. V. Nemytskiĭ and V. V. Stepanov, *Qualitative Theory of Differential Equations* (Gostekhizdat, Moscow, 1947; Princeton University Press, Princeton, 1960).
9. L. S. Pontryagin, *Collected Papers. Continuous Groups* (Nauka, Moscow, 1988), Vol. 3.

Translated by V. Devitsyn